Masteroppgave

NTNU
Norges teknisk-naturvitenskapelige universitet
Fakultet for naturvitenskap
Institutt for kjemisk prosessteknologi

Pål Martin Benum

Catalytic Oxidation of NO to NO_2 for Industrial Nitric Acid Production Using Promoted Ruthenium Catalysts

Masteroppgave i Sustainable Chemical and Biochemical Engineering
Veileder: Magnus Rønning
Medveileder: Jithin Gopakumar, Bjørn Christian Enger
Juni 2023

NTNU
Kunnskap for en bedre verden

Pål Martin Benum

Catalytic Oxidation of NO to NO_2 for Industrial Nitric Acid Production Using Promoted Ruthenium Catalysts

Masteroppgave i Sustainable Chemical and Biochemical Engineering
Veileder: Magnus Rønning
Medveileder: Jithin Gopakumar, Bjørn Christian Enger
Juni 2023

Norges teknisk-naturvitenskapelige universitet
Fakultet for naturvitenskap
Institutt for kjemisk prosessteknologi

NTNU
Kunnskap for en bedre verden

ABSTRACT

The growing world population and rising challenges of climate change require efficient and sustainable food production, and synthetic fertilizers have and will play a key role in achieving it. A key ingredient in the production of fertilizers is nitric acid, a chemical that is produced through a process called the Ostwald process. One of the three main steps in this process is the oxidation of NO to NO_2, which currently takes place as a homogeneous gas phase reaction in a series of heat exchangers. By substituting the current state-of-the-art bulky homogeneous reaction with a heterogeneous catalytic reaction, process intensification can be enabled through increased throughput and heat recovery while reducing capital expenditures.

In this work, seven alumina-supported catalysts were synthesized by wet impregnation, characterized, and tested for catalytic activity for oxidation of NO to NO_2 for industrial nitric acid production. Five catalysts were 5 wt% Ru promoted with varying amounts of Fe and Mn, in addition to a 1 wt% Fe and a 1 wt% Mn catalyst. The catalytic activity of the catalysts was investigated as a function of temperature in conditions simulating industrial nitric acid production conditions. A 48-hour isothermal test at 360 ^{o}C was also run to assess the stability of the catalysts.
Both fresh and spent catalysts were characterized by x-ray diffraction (XRD), N_2 adsorption, and CO chemisorption. Results revealed that the promotion of Ru with several metals did not significantly impact surface area, crystallite size, or dispersion of active metal. These properties were also maintained after both temperature ramp and long-term isothermal testing, indicating a high degree of stability of the promoted catalysts.

The promoted Ru catalysts exhibited moderate differences in catalytic activity. There was a trend of a decrease in the conversion of NO with an increase in metal loading and Fe content. Increasing Mn content generally led to lower dependence on temperature for the catalytic conversion, a desirable trait for a catalyst for industrial NO oxidation, as the thermodynamic equilibrium favors NO_2 at lower temperatures. The catalyst with the highest catalytic activity contained 5 wt% Ru and 1 wt% Mn, however, all promoted Ru catalysts performed significantly worse than unpromoted 5 wt% Ru/Al_2O_3. This leads to the conclusion that promoting Ru/Al_2O_3 catalysts with Fe and/or Mn through co-impregnation does not increase catalytic activity towards the oxidation of NO to NO_2 in conditions resembling industrial nitric acid production.

SAMMENDRAG

Den økende verdensbefolkningen og de økende utfordringene knyttet til klimaendringer krever effektiv og bærekraftig matproduksjon, og kunstgjødsel spiller en sentral rolle for å oppnå dette. En nøkkelingrediens i produksjonen av kunstgjødsel er salpetersyre, et kjemikalie som produseres gjennom en prosess kalt Ostwald-prosessen. En av de tre hovedtrinnene i denne prosessen er oksidasjonen av NO til NO_2, som for øyeblikket skjer som en homogen gassfase-reaksjon i en serie med varmevekslere. Ved å erstatte den nåværende homogene reaksjonen med en heterogen katalytisk reaksjon, kan prosessintensivering oppnås gjennom økt gjennomstrømning og varmegjenvinning, samtidig som kapitalkostnadene reduseres.

Syv aluminiumoksid-støttede katalysatorer ble syntetisert ved våt impregnering, karakterisert og testet for katalytisk aktivitet for oksidasjon av NO til NO_2 for industriell produksjon av salpetersyre. Fem katalysatorer var 5 vekt% Ru promotert med varierende mengder Fe og Mn, i tillegg til en 1% Fe og en 1% Mn katalysator. Katalysatorenes katalytiske aktivitet ble undersøkt som en funksjon av temperatur under forhold som simulerer forhold for industriell produksjon av salpetersyre. Det ble også utført en 48-timers isoterm test ved 360 ^oC for å evaluere stabiliteten til katalysatorene.

Både ubrukte og brukte katalysatorer ble karakterisert ved hjelp av røntgendiffraksjon (XRD),N_2-adsorpsjon og CO-kjemisorpsjon. Resultatene viste at promotering av Ru med flere metaller ikke hadde en betydelig innvirkning på overflateareal, partikkelstørrelse eller spredning av aktivt metall. Disse egenskapene ble også opprettholdt etter både testing under økende temperatur og langvarig isotermisk testing, noe som indikerer en høy grad av stabilitet for de promoterte katalysatorene.

De promoterte Ru-katalysatorene viste moderate forskjeller i katalytisk aktivitet. Det var en tendens til en nedgang i omsetning av NO med økende mengde metall og Fe-innhold. Økende Mn-innhold førte generelt sett til lavere avhengighet av temperatur for den katalytiske omsetningen, noe som er en ønskelig egenskap for en katalysator for industriell oksidasjon av NO, ettersom den termodynamiske likevekten favoriserer NO_2 ved lavere temperaturer. Katalysatoren som viste høyest katalytisk aktivitet inneholdt 5% Ru og 1% Mn, men alle de promoterte Ru-katalysatorene presterte betydelig dårligere enn den upromoterte 5% Ru/Al_2O_3. Dette ledet til konklusjonen om at promotering av Ru/Al_2O_3-katalysatorer med Fe og/eller Mn ikke øker den katalytiske aktiviteten for oksidasjon av NO til NO_2 under relevante forhold for industriell produksjon av salpetersyre.

PREFACE

This project forms part of the Industrial Catalysis Science and Innovation (iCSI) initiative, which was launched in 2015 through a collaboration between Yara, Sintef, and NTNU. Titled "Catalytic Oxidation of NO to NO2 for Nitric Acid Production," the objective of this endeavor is to identify a highly efficient catalyst for the oxidation of NO to NO2 under relevant conditions. Since the inception of the project, extensive research has been conducted on various materials.

Ata ul Rauf Salman became the project's inaugural Ph.D. candidate in 2015, and numerous master's students have also contributed to the project, with this thesis being the most recent. In 2020, Jithin Gopakumar joined the project as the current doctoral candidate, continuing the research efforts. Professor Magnus Rønning supervised this work while co-supervised by Jithin Gopakumar and Bjørn Christian Enger (SINTEF).

This thesis marks the end of a two-year Master's program "Sustainable Chemical and Biochemical Engineering" at the Norwegian University of Science and Technology (NTNU) in Trondheim, Norway. This thesis is a continuation of the specialization project in the course "TKP4580 - *Chemical Engineering, Specialization Project*" concluded in the fall of 2022, and was written for the Catalysis group at the Department of Chemical Engineering at NTNU. I wanna express my sincerest gratitude towards my supervisors Magnus Rønning, Jithin Gopakumar, and Bjørn Christian Enger for their support, input, and help with my work. Discussing my work with them has not only expanded my knowledge and understanding of catalysis but genuinely inspired me to pursue a career in the field of research. A special thanks goes out to Jithin for assisting with the practical aspect of the work, and always being willing to help and explain no matter how stupid my questions were. I also want to say thank you to all of the Master's students, Ph.D. candidates, professors, and all other employees at the Catalysis group for providing a great social environment during the hard work that this thesis has been. A special shoutout goes to Estelle Vanhaecke for help and training with characterization instruments, and even more so for being a genuinely wonderful person to be around. Her laugh echoing through the hallway has been a beacon of joy through some rather stressful periods of work.

CONTENTS

LIST OF FIGURES

LIST OF TABLES

ABBREVIATIONS

- **BET** Brunauer Emmett and Teller
- **BJH** Barrett-Joyner-Halenda
- **CEM** Control-Evaporation-Mixing
- **DRIFTS** Diffuse Reflectance Infrared Fourie Transform Spectroscopy Analysis
- **DSC** Differential Scanning Calorimetry
- **FTIR** Fourier Transform Infrared
- **FWHM** Full Width at Half Maximum
- **HRTEM** High-resolution transmission electron microscopy
- **LHHW** Langmuir-Hinselwood-Hougen-Watson
- **MvK** Mars van Krevelen
- **PFR** Plug Flow Reactor
- **SEM** Scanning Electron Microscopy
- **TCD** Thermal Conductivity Detector
- **TPR** Temperature Programmed Reduction
- **WHSV** Weight Hourly Space Velocity
- **XRD** X-Ray Diffraction
- **C** Constant in BET equation
- **p** Partial pressure
- $\mathbf{p_0}$ Saturation pressure
- **V** Volume
- $\mathbf{V_m}$ Adsorption volume
- **D** Metal dispersion

- **d** Distance between lattice planes
- $\mathbf{d_p}$ Average Crystallite size
- **K** Shape factor in Scherrer equation
- $\mathbf{H_{r,298}}$ Enthalphy of reaction at 298 K
- **a.u** Arbitrary unit
- $\mathbf{C_a}$ Carberry number
- **h** Hour
- **J** Joule
- **k** Rate constant
- **mol** Mole
- **min** Minute
- $\mathbf{NO_x}$ Nitrogen oxides
- **ppm** Parts per million
- $\mathbf{r_{NO}}$ Reaction rate of NO oxidation
- **SiC** Silicon Carbide
- **t** Time
- **wt%** Weight percentage
- $\mathbf{x_{NO,c}}$ Catalytic NO conversion
- $\mathbf{x_{NO}}$ Total NO conversion
- **Å** Ångstrom

CHAPTER

ONE

INTRODUCTION

1.1 Background

As the world's population keeps growing, and the fight against climate change keeps getting tougher, the need for efficient and sustainable food production increases. The second of UN's 17 Sustainable Development Goals, is to "end hunger, achieve food security and improved nutrition and promote sustainable agriculture" [1]. We need to improve the output of food production without using more land and without negatively affecting the environment [2, 3]. There are serious concerns that at the current pace, food production will not be able to keep up with the population growth, which is projected to grow to 10 billion globally by 2050 [4]. In order to feed this population sustainably, World Resource Institute has projected that we need to increase total crop calories by almost 60%, without expanding from the area used as farmland today [2].

One of several ways to improve crop yields without expanding farmland is to improve the quality of the soil, which can be done through the addition of fertilizers [5, 3]. Fertilizers can provide nutrients that are otherwise not available in the soil, replace nutrients lost during harvest, and balance the nutrients in the soil for higher crop yield and quality [6]. The three main compounds that modern fertilizers are composed of are nitrogen (N), phosphorous (P), and potassium (K), resulting in the commonly used name "NPK fertilizer" [7]. The fertilizer compounds need to be water-soluble for the plant roots to be able to absorb them. Sources of soluble nitrogen are ammonium (NH_4^+) and nitrate (NO_3^- ions, phosphate ions (PO_4^3) provide soluble phosphorous, and most common potassium compounds are soluble in water. Ammonium and nitrates are produced from nitric acid (HNO_3), and about 70% of the nitric acid produced is used for this purpose [8].

Yara is the leading producer of nitrogen fertilizer in the world [9], and has continuously improved the production process over the last century. The process used for producing nitric acid is called the Ostwald process and consists of three main steps. The first step is the catalytic oxidation of ammonia (NH_3) to nitrogen monoxide (NO) using platinum/rhodium gauze as the catalyst [10]. The second step is the oxidation of NO to nitrogen dioxide (NO_2), before the final step of absorbing NO_2 absorbing in water to form nitric acid [8, 11]. The second step, oxidation of NO

to NO_2, is a third-order reaction that favors low temperatures [11], and currently takes place as a homogeneous gas-phase reaction in a series of heat exchangers without using a catalyst [8]. It is believed that the use of a catalyst in this step of the process could improve the efficiency and economic cost of NO oxidation. With the global annual production of nitric acid reaching over 60 million tonnes [12], process intensification of NO oxidation would be a significant step toward a sustainable future for both the chemical and food production industry.

1.2 State of the Art

Many studies have been conducted and published on effective catalysts for NO oxidation, however, almost exclusively in regards to NO_x emission abatement, where the concentrations of NO are in levels of ppm. The catalyst performance changes drastically when the conditions change to industrial nitric acid production conditions, where the high concentration of NO (10%) and presence of water (15%) in the feed pose challenges. Salman reported how the performance of supported platinum catalysts changed from diesel exhaust to nitric acid production conditions, with the presence of water and strongly oxidizing conditions significantly inhibiting the catalytic activity of Pt [13]. Only three patents exist on the catalytic oxidation of NO to NO_2, and neither has seen any commercial use [14, 15, 16].

In recent years, alternatives for catalysts for NO oxidation at conditions resembling industrial nitric acid production have been investigated, and studies of alumina-supported catalysts with active metals like Ru and Pt have reported promising results [13, 17, 18]. Manganese oxides have also been explored as a cheaper and more available option to noble metals and have revealed good catalytic performance for NO oxidation at nitric acid production conditions [13, 19]. This recent progress encourages further research of alumina-supported Ru and MnO_x catalysts.

1.3 Motivation

The main goal of this research project is to develop a catalyst that efficiently oxidizes NO to NO_2 at conditions relevant to nitric acid production. The current process utilizes the inverse temperature dependence of the oxidation reaction to shift the equilibrium towards NO_2, by reducing the temperature through a series of heat exchangers which also allows for sufficient residence time for the reaction to take place. A fraction of the heat is recovered, while there is also significant heat loss through the pipe walls between each heat exchanger [11]. Replacing this bulky process with a single step for catalytic reaction and heat recovery can therefore significantly increase not only the heat recovery itself but also the capital expenditure (CAPEX) of nitric acid production plants, as there would be less need for space and process equipment. Additionally, according to equilibrium calculations, the conversion of NO to NO_2 could be increased from the current degree of 20% up to about 90% [17]. A summary of the process intensification and its potential

benefits is described in Figure 1.3.1.

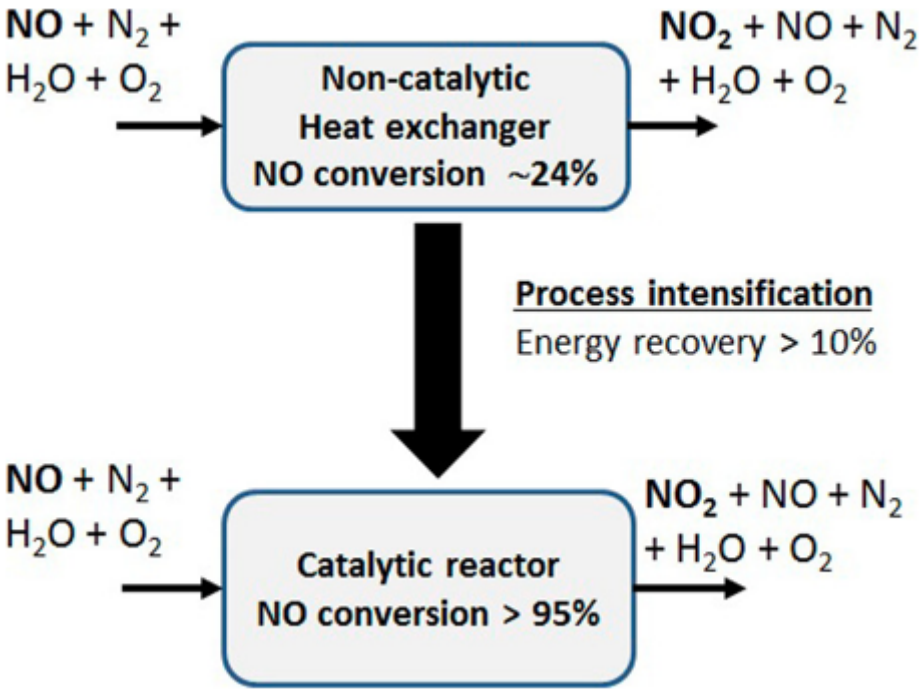

Figure 1.3.1: Process intensification in nitric acid plants by catalytic oxidation of nitric oxide, 4.7 bar pressure. Obtained from Grande etal · [17].

Additional motivation for this research includes gaining a better understanding of catalytic oxidation of NO to NO_2 under nitric acid production conditions, specifically regarding how catalytic performance is affected by the additions of several promoters in various amounts. The characterization of bimetallic and trimetallic catalysts may also give insight into how the addition of several active metals affects catalyst characteristics like reducibility, dispersion, and surface area.

In summary, the motivation for this research project is to:

- Increase the conversion of NO to NO_2 for nitric acid production.
- Reduce CAPEX for future nitric acid plants.
- Increase the rate of heat recovery in nitric acid plants.
- Better understand the conversion of NO oxidation in regard to the addition of several promoters in various amounts.
- Better understand the challenges regarding the synthesis, characterization, and testing of bi and trimetallic catalysts.
- Increase throughput to the absorber, increasing the yield of nitric acid.

1.4 Strategy

This project aims to synthesize, characterize, and test catalysts for catalytic oxidation of NO under simulated nitric acid plant conditions, continuing the promising research done across several projects. A wide variety of active metals and supports have been tested, including ruthenium (Ru), manganese oxides (MnO_x), and platinum (Pt) on supports of gamma alumina ($\gamma-Al_2O_3$) and zirconia (ZnO_2) [13, 19, 17, 20]. This work will be focusing on promoted $Ru/\gamma-Al_2O_3$ catalysts.

This master's project is the continuation of the work done in the course TKP4580 - *Chemical Engineering, Specialization Project* in the fall of 2022 at NTNU Gløshaugen. In that project, three catalysts were synthesized, characterized, and tested for NO oxidation for nitric acid production. The catalysts were 1 wt% Pt/Al_2O_3, 1 wt% Ru/Al_2O_3, and 5 wt% $/Al_2O_3$. The fresh catalysts were characterized by X-ray diffraction (XRD), N_2 physisorption, temperature-programmed reduction (TPR), and chemisorption. They were then tested for catalytic activity as a function of temperature from 150-450 ^oC at 1 bar pressure. The feed composition was similar to that of the feed for NO oxidation in nitric acid production plants, that is 10% NO, 6% O_2, and 15% H_2O. A long-term isothermal activity test was also conducted at 350 ^oC for 45 hours in order to determine the stability of the catalysts. Efforts were also made to determine the reaction order with respect to different components, however, challenges regarding the steady state of the reaction rate made results unreliable. Spent catalysts were also characterized to determine how the reaction affects the catalysts, contributing to the evaluation of the catalyst's stability and suitability.

The aforementioned work concluded that the Ru/Al_2O_3 catalyst performed better than Pt/Al_2O_3 in every aspect, that is both with regards to catalytic activity and long-term stability. 5 wt% Ru/Al_2O_3 also showed higher catalytic activity than 1 wt% Ru/Al_2O_3. This master's project aims to develop promoted 5 wt% Ru/Al_2O_3 catalysts, in order to find a catalyst that displays even higher catalytic activity towards NO oxidation. The catalysts will have different amounts of promoters so study the effect of metal loading on catalyst characteristics and activity. The strategy will be similar to that of the specialization project, where fresh and spent catalysts will be characterized before and after activity testing. The feed composition for activity testing will also be the same - 10% NO, 6% O_2, and 15% H_2O, simulating nitric acid plant conditions. The temperature range will be 150-450 ^oC at atmospheric pressure.

The activity tests will be run in a packed bed reactor in Rig 2.1 on the second floor of Chemistry Hall D. This rig has been modified and optimized towards eliminating some key challenges when attempting to replicate an industrial process in a laboratory [20, 18]. In order to study catalytic activity it is important to minimize the gas phase conversion, which is favored by longer residence time. Gas lines have therefore been shortened and reactor design optimized, and empty reactor runs were conducted to measure the gas phase conversion. The NO oxidation reaction is also sensitive to temperature and pressure gradients. The reactor design has been optimized, and silicon carbide (SiC) was used to minimize these gradients.

CHAPTER

TWO

INDUSTRIAL NITRIC ACID PRODUCTION

2.1 History

Mankind has for a long time sought to improve the quality of the soil we use for farming, and the first known trace of nitric acid goes as far back as the 8th century when Arab alchemist Abu Musa Jabir ibn Hayyan (721-815) synthesized it by distilling sulphuric acid (H_2SO_4) with saltpeter (potassium nitrate, (KNO_3) [21]. This remained the primary way of producing nitric acid for the next millennium until the saltpeter was replaced with Chile saltpeter (sodium nitrate, $NaNO_3$). The Chile saltpeter was a natural resource found mainly in northern Chile and as the 20th century began, the reserves were nearly exhausted [22, 23]. Simultaneously, a rapidly growing global population caused an increased need for food production, and humanity was in dire need of a way to supply its soil with nitrogen. With the natural resources diminishing, efforts were made to instead extract nitrogen from the atmosphere.

The Norwegian physicists Kristian Birkeland and Sam Eyde developed a process in 1903 that was able to oxidize the nitrogen in the air by passing it through an electric arc at over 2000 ^oC, producing nitrogen monoxide (NO) and nitrogen dioxide (NO_2). This gas mixture was then absorbed in water to form nitric acid [24]. With cheap, renewable energy available nearby, two production plants were built in Rjukan and Notodden in Norway. However, the process required enormous amounts of electricity compared to the amount of nitric acid produced, and a German chemist by the name of Wilhelm Ostwald had almost simultaneously developed a more energy-efficient process. This process, now commonly referred to as the Ostwald process, produced nitric oxide by oxidizing ammonia (NH_3) over a platinum-based catalyst [11, 23]. Fritz Haber and Carl Bosch had by 1913 successfully developed a process to produce ammonia by letting a nitrogen/hydrogen gas mixture react at high pressures over an iron-based catalyst. The hydrogen could be produced from fossil fuels, and the Haber-Bosch process quickly ensured a consistent and affordable supply of ammonia [24, 23]. This caused the Ostwald process to be both energetically and financially superior to the one of Birkeland and Eyde, and it quickly became the preferred method of producing nitric acid worldwide. While many improvements have been made, the core principles of the process remain the same to this day. The success of the Ostwald process has

enabled fertilizer production to reach unprecedented heights, likely enabling the lives of several billion people [25].

2.2 Ostwald Process

All industrial-scale nitric acid production uses the Ostwald process, which consists of three main chemical steps:

1. Catalytic oxidation of ammonia to nitric oxide
2. Oxidation of nitric oxide to nitrogen dioxide
3. Absorption of nitrogen dioxide in water

Figure 2.2.1 illustrates a schematic of the Ostwald process.

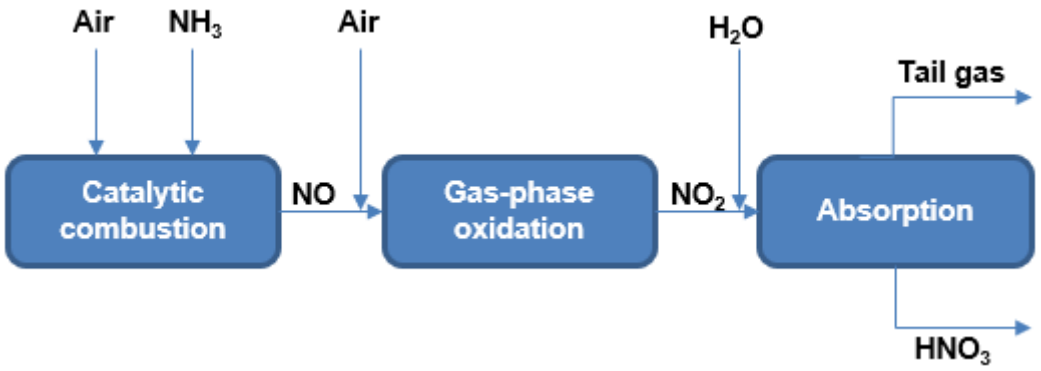

Figure 2.2.1: A simplified block diagram illustrating the Ostwald process. Three steps: catalytic oxidation of NH_3, oxidation of NO, and absorption in water. Illustrated by Benum.

The first step is the oxidation of ammonia, where a 1:9 ammonia/air mixture enters a catalytic converter [8]. The desired reaction is presented in Equation 2.1 [11].

$$4\ NH_3 + 5\ O_2 \rightarrow 5\ NO + 6\ H_2O \qquad \Delta H_{r298} = -907\ kJ/mol \tag{2.1}$$

There are two additional reactions that can take place between oxygen and ammonia, both producing undesired byproducts in N_2 and N_2O. These reactions are presented in Equation 2.2 and Equation 2.3, respectively [11].

$$4\ NH_3 + 3\ O_2 \rightarrow 2\ N_2 + 6\ H_2O \qquad \Delta H_{r298} = -1261\ kJ/mol \tag{2.2}$$

$$4\ NH_3 + 4\ O_2 \rightarrow 2\ N_2O + 6\ H_2O \qquad \Delta H_{r298} = -1103\ kJ/mol \tag{2.3}$$

By looking at the heat of reaction for the three reactions, it is clear that N_2 (Equation 2.2) is the most thermodynamically favored product. N_2 is inert and not useful

in the next step of production, and N_2O is a potent greenhouse gas [26]. This issue with selectivity is solved by using a catalyst. The most common catalyst consists of a very fine gauze of 90-95% platinum (Pt) and 5-10% rhodium (Rh), which significantly improves the selectivity towards NO production [23]. NO formation (Equation 2.1) is also the least exothermic reaction, meaning higher temperatures favor selectivity towards NO. Typical oxidation temperatures therefore range between 750-900 ^oC, which together with the catalyst enables the reaction to reach around 95% yield of NO [8]. Such high temperatures cause catalyst loss due to PtO_2 evaporation, which is why Rh is added to the catalyst. Rh helps reduce PtO_2 evaporation and also increases the mechanical strength of the gauze [23]. Many modern nitric acid plants also employ palladium (Pd) gauze right underneath the Pt/Rh gauze, which "catches" the lost PtO_2 by forming an alloy with it [27].

The next step in the Ostwald process is the gas phase oxidation of NO to NO_2 and its liquid dimerN_2O_4. The reaction is presented in Equation 2.4.

$$2\ NO + \ O_2 \rightarrow 2\ NO_2 \ \leftrightarrow \ N_2O_4 \qquad \Delta H_{r298} = -113.8\ kJ/mol \tag{2.4}$$

The exothermic reaction (Equation 2.4) is thermodynamically favored by high pressure and low temperature. The degree of NO oxidation (i.e. NO_2 content) at 1 bar as a function of temperature is illustrated in Figure 2.2.2.

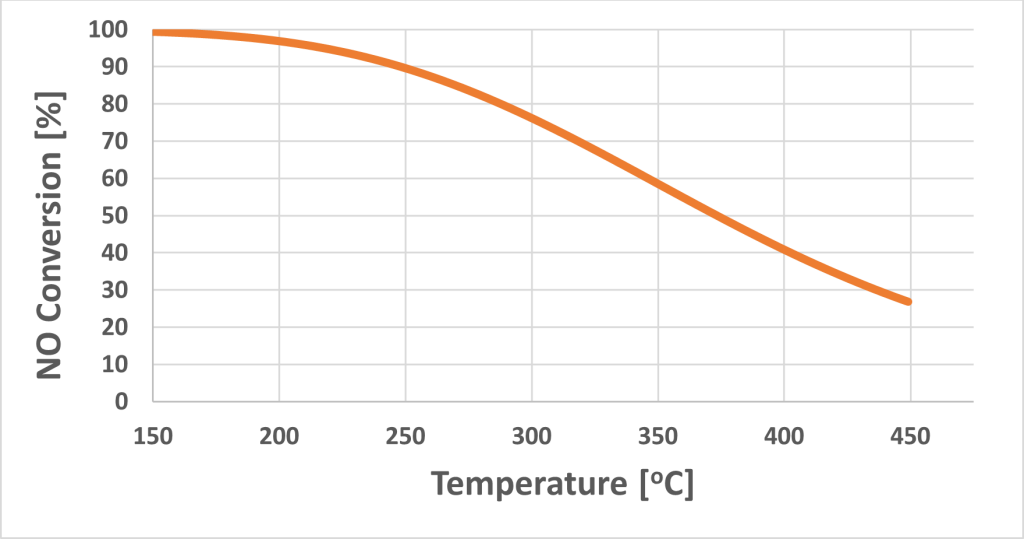

Figure 2.2.2: Conversion of NO to NO_2 based on the thermodynamic equilibrium as a function of temperature at 1 bar pressure.

The NO oxidation reaction is one of few third-order reactions. The rate expression is presented in Equation

$$-r_{NO} = \frac{dP_{NO_2}}{dt} = k_P(P_{NO})^2 P_{O_2} \tag{2.5}$$

Where k_P is the rate constant, and P_{NO2}, P_{NO}, and P_{O2} are the partial pressures of NO_2, NO, and O_2, respectively. This rate expression shows that the reaction has a second-order dependence on the concentration of NO and a first-order dependence on the concentration of oxygen. Figure 2.2.3 shows the rate constant as a function

of temperature.

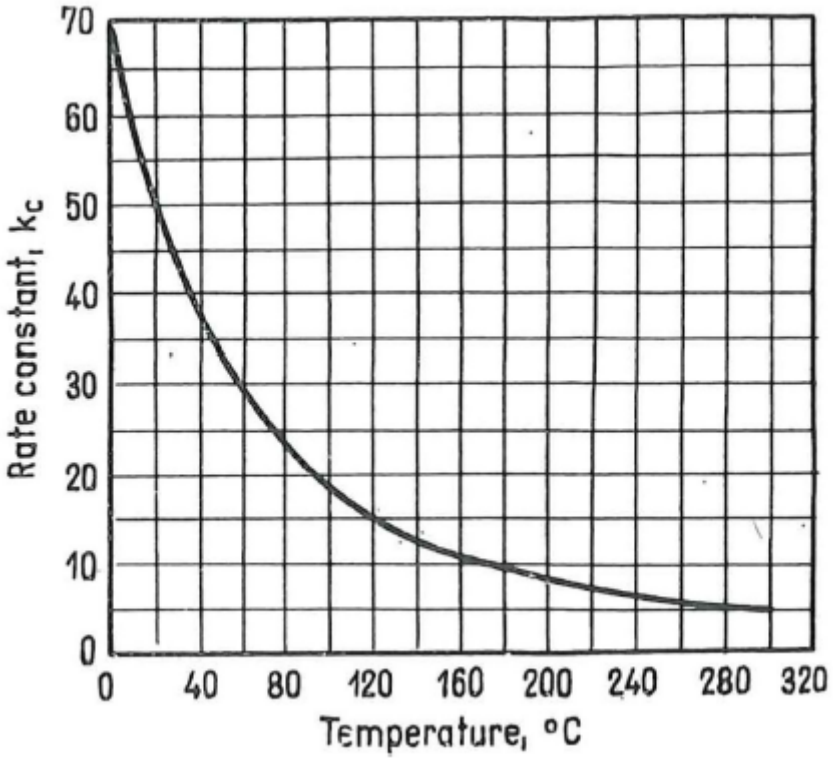

Figure 2.2.3: Rate constant of the NO oxidation reaction as a function of temperature. Obtained from Honti, 1976 [28].

As Figure 2.2.3 shows, the rate constant increases with decreasing temperature. This means that the NO oxidation reaction is both kinetically and thermodynamically favored by low temperatures. This reduction in temperature is achieved by passing the process stream through a series of heat exchangers. This recovers some heat and allows for a longer residence time, which helps the conversion since the rate of reaction for NO oxidation is slow [17]. Much effort has been done to develop a catalyst to increase the reaction rate, but it has proved challenging. The composition of the product stream of the ammonia oxidation in a typical nitric acid plant is 10% NO, 6% O_2, and 15% H_2O. The conditions are strongly oxidizing, and the presence of water has proven to inhibit the activity of some promising catalysts such as coke [13]. The fact that the reaction is favored by low temperatures is also an issue since catalytic activity is typically favored by high temperatures, as suggested by the Arrhenius law [28]. It is therefore desired to develop a catalyst that displays catalytic activity at lower temperatures.
The final step of the Ostwald process is the absorption of the NO_2/N_{2O4} mixture in water. This absorption process is quite complex, as many different reactions can take place both in the gas phase and the liquid phase. Equation 2.6.

$$2\ NO_2 + \ H_2O \rightarrow 2\ HNO_3 + NO \qquad \Delta H_{r298} = -37\ kJ/mol \tag{2.6}$$

As previously mentioned, the different stages involved in the Ostwald process have a preference for either high or low pressure. When designing a nitric acid produc-

tion plant, it is crucial to consider the operating pressure as it results in two primary process designs that are commonly used - the single-pressure and dual-pressure plants. The single-pressure processes typically operate at high-pressure levels (between 7 to 12 bar) and use a higher temperature for the catalytic oxidation of ammonia, which improves energy recovery efficiency. On the other hand, the dual-pressure process involves the placement of a compressor between the ammonia oxidation stage and the reaction of NO_2 with water to form nitric acid. This process uses a lower pressure (between 4 to 5 bar) for the ammonia oxidation stage and a higher pressure (between 10 to 15 bar) for the absorption of NO_2 in water.

CHAPTER

THREE

CATALYTIC OXIDATION OF NO

3.1 Alumina as Support

Al_2O_3, commonly referred to as alumina, is widely used as catalyst support in various industrial and scientific applications due to its many unique properties. The combination of high surface area, porosity, thermal stability, chemical inertness, acid-base properties, and versatility makes alumina an excellent catalyst support material [29, 30, 31]. It is also well-suited for the impregnation and dispersion of active metals, as the Lewis acid and base sites on the surface provide sites for ionic and metallic species to attach onto [29]. These properties also make alumina more suitable for acidic reactions compared to other common support materials like zirconia, ceria, and titania.

Alumina, can exist in a wide variety of polymorphs, such as α, ϑ, δ, ν, and γ-Al_2O_3. The transitions between these phases can occur during heat treatment, and the phase of the alumina support will depend on the calcination temperature and precursor used for synthesis, as illustrated in Figure 3.1.1.

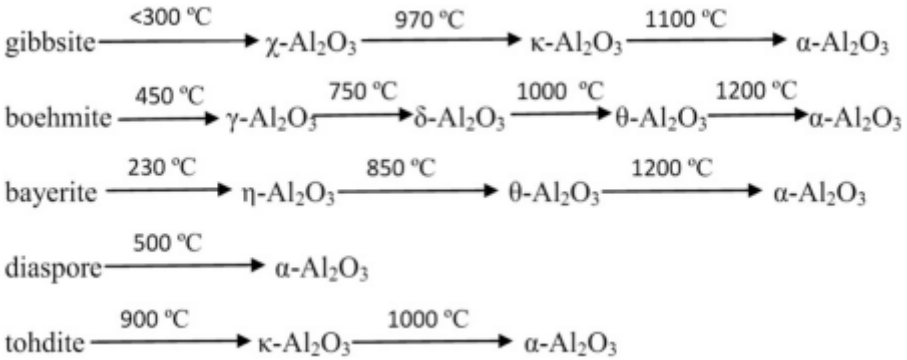

Figure 3.1.1: Phase transformations of alumina. Obtained from Xie et. al. [32]

The different phases of alumina all have different characteristics, like physical strength, chemical activity, porosity, and surface area. The most prominent alumina phase used in catalysis is γ-Al_2O_3, which has a high surface area ($>$ 200

m^2/g), high catalytic activity and adsorption capacity, and good wear-resistance [29, 31]. γ-Al_2O_3 has been used as support material for studies on NO oxidation for industrial nitric acid production. Studies have been conducted by Grande *et al.* [17] and Salman *et al.* [13, 20], on catalytic NO oxidation in industrial nitric acid production conditions over alumina-supported catalysts. They report that γ-Al_2O_3 as support exhibits excellent stability under NO oxidation and allows for easy impregnation with active metals resulting in high dispersion and surface area. Wang *et al.* [33] studied NO oxidation over MnO_x supported on alumina and titania, and found that the performance of the catalysts decreased in the order of $Mn_{0.4}/Al_2O_3 > Mn_{0.2}/Al_2O_3 > Mn_{0.4}/TiO_2 > Mn_{0.2}/TiO_2 > MnO_x > Al_2O_3$, indicating MnO_x/Al_2O_3 synergy for catalytic NO oxidation. They also detected adsorbed oxygen as the active oxidizer, rather than lattice oxygen.

3.2 Ruthenium Catalysts

Ruthenium is known as a good oxidation catalyst, as the versatile transition metal exhibits oxidation states from -II to +VIII, and is widely researched and used in ammonia synthesis and many other oxidation reactions [18, 34, 35, 36]. Numerous studies have been conducted on the adsorption of NO on Ru catalysts. Sokolova *et al.* [37] investigated the adsorption and decomposition of NO on Ru/Al_2O_3 catalysts, and found that NO adsorption on oxidized Ru occurs via nitrite and nitrate routes. They also found that NO adsorbs more easily on oxidized Ru at temperatures above 300 ^oC. Li *et al.* [35] investigated the oxidation of NO to NO_2 over Ru catalysts, however at conditions relevant to diesel exhaust, where NO exists in concentrations of ppm levels. Conditions in NO oxidation for industrial nitric acid production present much higher concentrations of NO (10%) and significant amounts of H_2O (15%). These are strongly oxidizing conditions, which as reported by Salman [13] inhibit the activity of common NO oxidation catalysts like Pt.

One recent investigation of NO oxidation over supported Ru catalysts at nitric acid production conditions was conducted by Gopakumar *et al.*. Ru/γ-Al_2O_3 catalysts were tested for oxidation of NO at industrial nitric acid production conditions and exhibited promising levels of activity at both 1 and 4 bar pressure. Investigations of activation energy, reaction order, and reaction mechanisms were also conducted. An apparent activation energy (E_a) of 152 kJ/mol was reported for NO oxidation over a 0.5 wt% Ru/Al_2O_3 catalyst in the temperature range 340-366 ^oC and 1 bar pressure, which is higher than the activation energy of 33 kJ/mol for Pt catalysts as reported by Salman *et al.* [20]. An Eley-Rideal mechanism was proposed as the reaction mechanism for NO oxidation over the supported Ru catalysts, where NO adsorbs on oxidized Ru and gaseous NO_2 is generated by dissociation of adsorbed NO_3. The proposed mechanism is presented in Equations 3.1-3.4:

$$O_2 + 2^* \xleftrightarrow{K_1} 2O^* \tag{3.1}$$

$$2NO + 3O^* \xleftrightarrow{K_2} 3NO_3^* + NO_2^* + ^* \tag{3.2}$$

$$NO_3^* \xleftrightarrow{\mathrm{K_3}} NO_2 + O^* \tag{3.3}$$

$$NO_2^* + 0.5O_2 \xrightarrow{\mathrm{k_4}} NO_3^* \tag{3.4}$$

Where * is a free active site, and K_i and k_i are equilibrium and rate constant, respectively. By assuming O as the most abundant reaction intermediate (MARI), and the reaction in Equation 3.4 as the rate-limiting step, the rate expression became as described in Equation 3.5 when the surface coverage of adsorbed O exceeds the fraction of free sites ($\Theta_{\mathrm{O}} \gg 1$):

$$r = \frac{k_4 * K_G * P_{NO}^2 * P_{O_2}}{P_{NO_2}} \tag{3.5}$$

Where $K_G = (K_1)^{0.5} * K_2/K_3$. The reaction rate is inversely dependent on the partial pressure of NO_2, first order with respect to O_2, and second order with respect to the partial pressure of NO.

Aika *et al.* [38] studied the effect of various promoters on Ru/Al_2O_3 catalysts for ammonia synthesis, and found that the addition of alkali precursor promoters increased the dispersion and activity of Ru. The viability of promoting Ru and reported high catalytic activity encourage further research of supported Ru catalysts for NO oxidation at industrial nitric acid production conditions.

3.3 Manganese Oxide Catalysts

Manganese oxides are useful for various uses within the field of heterogeneous catalysis. Supported manganese oxide catalysts show promising catalytic activity in a wide variety of oxidation reactions, with key attributes like high chemical stability and good redox properties, allowing for a variety of Mn oxidation states and crystalline phases [13, 39, 40, 41, 42, 43, 44]. In recent years, manganese oxide has gained attention and has been studied for use in diesel exhaust, which involves the catalytic oxidation of NO [39]. Mn is much cheaper than noble metals like Pt and leaves a smaller environmental footprint since it is available in larger quantities, being the 12th most abundant element on earth [45]. This makes it an intriguing prospect to replace noble metals for catalytic oxidation of NO.

The mechanism of NO oxidation on MnO_x/TiO_2 catalysts was studied by Tang et. al through the use of in situ diffuse reflectance infrared Fourier transform spectroscopy (DRIFTS). They found that the reaction takes place via a Mars-van Krevelen (MvK) mechanism, where NO first coordinates to Mn sites. It is then oxidized by lattice oxygen to form nitrates, which finally decompose to NO_2 at high temperatures [46]. It is also believed that the oxidation of organic molecules over transition metal oxides like MnO_x also proceeds via the MvK mechanism, where the metal oxide is re-oxidized by adsorbed oxygen [47]. Manganese oxides display apparent capabilities of oxygen storage and release when undergoing a rapid cycle of oxidation and reduction by interacting with reducing and oxidizing

agents [43, 47].

Manganese oxides can exist in a wide variety of forms, and the choice of method of preparation, precursor, calcination temperature, and support material can all affect the oxidation state and crystalline structure of MnO_x [13, 43]. Nitrates or acetates are common precursors, and when using alumina as the support, nitrate precursors typically lead to microcrystalline MnO_x as mainly Mn (IV) and Mn (III), while using acetates results in surface metal oxide, mainly Mn (III) [48]. Calcination temperature is also important for the oxidation state of Mn, as a temperature of 525 ^oC or lower results in Mn (IV), while using higher temperatures results in Mn (III) [44]. It is vital to know what state is most active toward the reaction one is developing the catalyst for. Wang et al. investigated the catalytic activity of different manganese oxides (MnO_2, Mn_2O_3, and Mn_3O_4) in typical diesel exhaust conditions, that is 500 ppm NO, 5 vol%, 15 vol% H_{2O} (when used), and 200 ppm SO_2 (when used). It was found that the activity decreased in the order of $MnO_2 > Mn_2O_3 > Mn_3O_4$, meaning that the oxidation state of Mn (IV) is the most catalytically active towards NO oxidation in such conditions [49].

Mn (IV) can also exist in a number of different crystalline structures, which can greatly affect catalytic activity [50, 39]. Chen et al. tested different crystal structures of unsupported MnO_2 for catalytic oxidation of NO. The different phases α-, β-, γ-, and δ-MnO_2 were synthesized and tested for catalytic activity in 500 ppm NO, 5 vol%, 10 vol% H_{2O} (when used), and 200 ppm SO_2 (when used), across a temperature range of 100-400 ^oC. The different MnO_2 crystal structures exhibited significantly different activities, with γ-MnO_2 being the best. γ-MnO_2 is a mix of the two structures pyrolusite and ramsdellite, which may lead to it being rich in point defects and vacancies. Chen *et al.* [39] proposed that these vacancies can act as active sites for oxidation and that this together with the high porosity and surface area of γ-MnO_2 gives it its high catalytic activity towards NO oxidation. They illustrated the mentioned crystal structures of MnO_2, which are displayed in Figure 3.3.1.

3.4 Iron Catalysts

Iron serves as a key catalyst component for many oxidation reactions due to its vast availability and good redox properties, with its wide range of oxidation states (-IV to +VI) [51, 52]. Supported iron catalysts have been widely used in industrial oxidation reactions, like in the Haber-Bosch process, where iron-based catalysts facilitate the oxidation of nitrogen gas to produce ammonia [53, 54]. Iron catalysts are also employed in the oxidation of hydrocarbons, such as the Fischer-Tropsch process for the synthesis of liquid fuels from syngas [55, 56]. No studies have been published on the oxidation of NO over iron, however, the general rich redox chemistry and use of Fe in other oxidation reactions indicate that it may be effective as a promoter. Iron is also much cheaper and leaves a negligible environmental footprint compared to noble metals, making it an intriguing option for the promotion of supported catalysts for industrial NO oxidation.

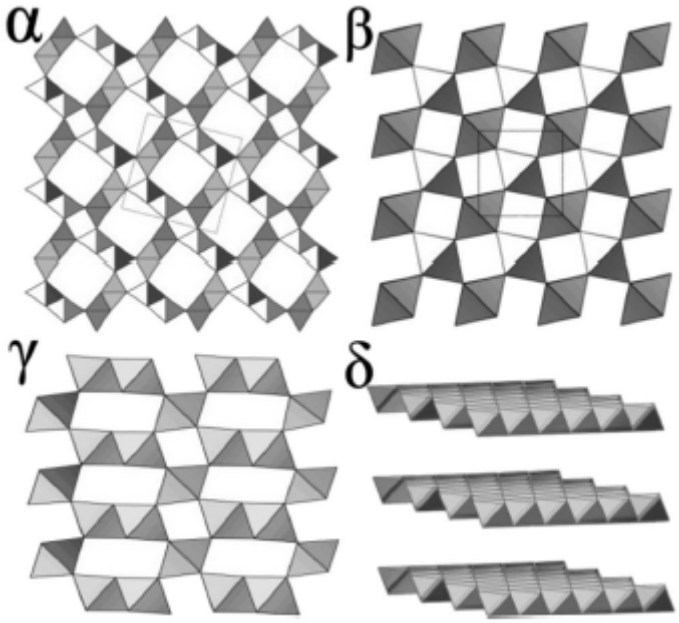

Figure 3.3.1: Crystal structures of α-, β-,γ-, and δ-MnO_2, illustrated by Chen *et al.* [39].

CHAPTER

FOUR

THEORY

4.1 Catalyst Preparation

As there are a wide variety of types of catalysts within heterogeneous catalysis, there also exist different preparation methods. The choice of preparation method can significantly affect the cost of preparation and catalyst characteristics like surface area, dispersion, and metal loading. The methods for preparing catalysts can be broadly categorized as dry and wet techniques. The co-precipitation method is typically preferred when trying to achieve a porous material with a large surface area, along with maximum catalytic activity per unit volume. The cost of the materials also plays an important role and co-precipitation is typically only chosen when the precursor materials are cheap. Conversely, if the catalyst preparation involves costly precursors like noble metals and the intention is to deposit the active phase as nanometer-sized particles onto the support material, the preferred methods are either impregnation or precipitation from a solution [30, 57].

4.1.1 Impregnation

Impregnation is a catalyst preparation method where a support material is impregnated with a precursor solution containing the desired active component, typically a catalytically active metal. There are two main types of impregnation techniques: wet impregnation and incipient wetness impregnation, also referred to as dry impregnation. Prior to impregnation, the support material typically undergoes either drying or calcination to eliminate any volatile impurities or residual moisture. This step is crucial in reducing the potential risk of pore blockage in the catalyst. A precursor solution of volume V is then introduced into the support material, which possesses a total pore volume V_{PT}. In wetness impregnation, the solution is added in excess ($V > V_{PT}$). In incipient wetness impregnation, the quantity of precursor solution employed is precisely equivalent to the volume of pores within the support ($V = V_{PT}$), ensuring no excess solution remains outside the pore space. This is typically achieved empirically by simply adding water dropwise until the sample looks fully wetted but with no excess solution remaining [30, 57, 58]. One can also estimate the required volume V by determining the specific pore volume by a characterization method like N_2 physisorption.

Capillary suction helps draw the precursor solution into the support's pores. The displacement of the air within the pores occurs when the capillary pressure surpasses the pressure of the trapped air inside the pore, particularly in cases where the pore has a small radius. The air bubbles can exert significant pressure, reaching magnitudes of tens of bars, which can lead to the rupture of the pore walls if the support material is not structurally strong enough. Under typical conditions and with appropriate support materials, the air dissolves into the solution and gradually escapes from the catalyst's pores [58]. Figure 4.1.1 illustrates the mass transfer inside the catalyst pores during wet and dry impregnation.

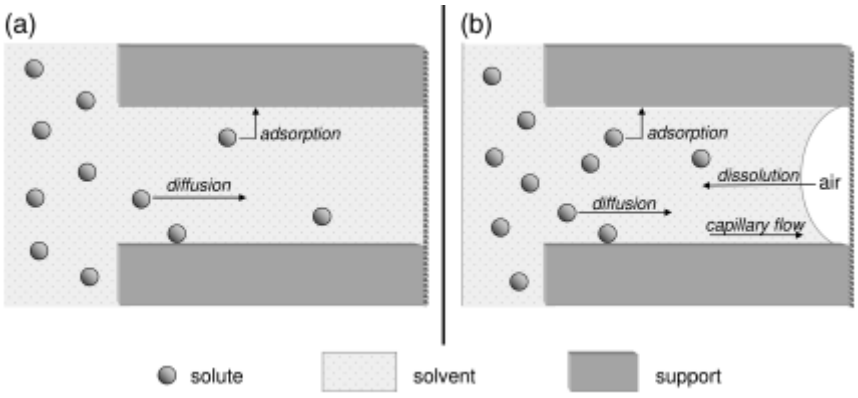

Figure 4.1.1: Mass transfer in a) wet and b) dry impregnation, solute moving from left to right. Obtained from Marceau *et.al.*[58].

In addition to pressure, there are many factors that affect the impregnation process, including temperature and the amount of active metal. A solid/gas phase being substituted with a solid/liquid phase is often an exothermic process and leads to heat release, which may alter the impregnation conditions, especially if the precursor's solubility is sensitive to temperature changes. If the viscosity of the solution is excessively high, it can extend the time it takes to wet and fill the pores of the support material. Furthermore, it is important to consider that the precursor's loading is limited by its solubility in the solution [57]. After impregnation is completed, the sample is typically dried in an oven overnight to evaporate the bulk of the precursor solvent.

4.1.2 Calcination

Calcination is a process that involves heating a substance, typically a solid material, at high temperatures in a controlled environment. The purpose of calcination is to bring about various physical and chemical changes in the catalyst, resulting in desirable properties or transformations. One of these is the removal of impurities, like volatile compounds and anions from the precursor solution which remain in the catalyst pores after impregnation. By subjecting the material to high temperatures, these impurities are typically burned off or vaporized, resulting in a purer catalyst [58, 59]. Calcination can also activate the catalyst by initiating structural changes or phase transformations. Heating at elevated temperatures can promote the reorganization of atoms or ions, leading to the development of desired catalytic properties. For example, the calcination of metal oxides can induce lattice rearrangements, creating active sites for catalytic reactions. Phase

transformations caused by calcination can result in an increase in desired properties like mechanical strength or surface area if the appropriate temperatures are chosen [59]. Alumina, for example, can exist in a wide variety of phases depending on the calcination temperature and precursor. As explained in Section 3.1, γ-Al_2O_3 is typically the desirable alumina phase for use as catalyst support, due to its high surface area, catalytic activity, and adsorption capacity [29, 31]. α-Al_2O_3 on the other hand has a much lower surface area but has a number of useful traits such as high resistance to heat, acid, and alkali, while also being physically hard and strong. [32, 60]. It is therefore important to choose the right temperature and heating rate when calcining catalysts.

The choice of atmosphere is also a key factor for the effect of calcination. While one can use high-temperature furnaces for calcination in air, there also exists dedicated calcination setups which enable gas flow through the sample during heating. Air or oxygen can be used to oxidize the active metal and/or the support, while H_2 is commonly used for reduction. The choice of gas depends on what phase of the catalyst is considered the active phase - if the known active phase for the catalyst is an oxide phase one should use air or oxygen, while if the metallic state is considered more active, H_2 should be employed instead.

4.2 Characterization methods

The following sections will give the theoretical background of every characterization technique utilized in this project.

4.2.1 X-ray diffraction

X-ray diffraction is a technique used to study the arrangement of atoms in a crystal lattice, and is based on the principles of wave interference. When X-rays are directed at a crystal, they are diffracted by the atoms in the crystal lattice. The diffracted X-rays then form a pattern of bright spots, known as a diffraction pattern, which is recorded on a detector. The pattern of bright spots in the diffraction pattern is caused by the constructive interference of X-rays that have been diffracted by the crystal [61].

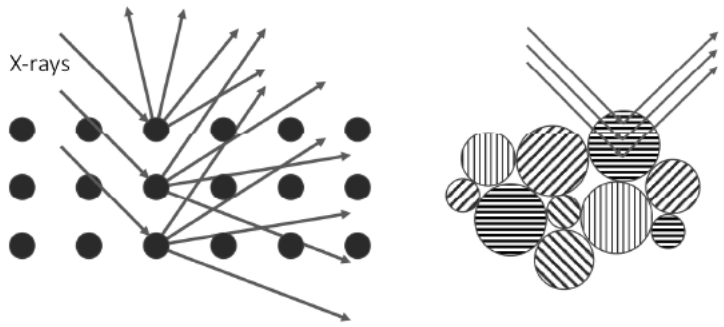

Figure 4.2.1: X-rays being scattered by the atoms in the lattice. Obtained from Chorkendoff and Niemantsverdriet [30].

The spacing between the atoms in the crystal lattice determines the angle at which the X-rays are diffracted and the intensity of the diffracted X-rays. This lets us determine the spacing between the atoms in the crystal lattice by analyzing the diffraction pattern and using Bragg's equation, which is described in Equation 4.1 [62].

$$2dsin(\theta) = n\lambda \tag{4.1}$$

Where λ is the beam wavelength, θ is the incident angle, n is an integer, and d is the distance between the diffracting planes. The concept is visualized by Figure 4.2.1.

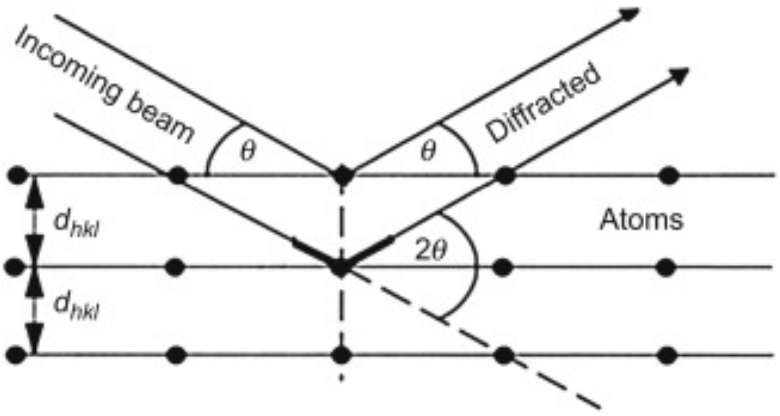

Figure 4.2.2: Diffraction of x-rays by atoms in the crystal lattice. Obtained from Epp [63].

This information can be used to determine the crystalline phases present in a sample, by comparing the pattern to patterns of known compounds. Another property that can be determined from the diffraction pattern is the size of the crystallites. This can be calculated using the Debye-Scherrer equation, which relates crystallite size to the diffraction angle and the wavelength of the X-rays. It is given by Equation 4.2 [64].

$$D = \frac{K\lambda}{\beta \cos\theta} \tag{4.2}$$

Where λ is the X-ray wavelength, β is the full width at half maximum (FWHM), and θ is the diffraction angle. K is the Scherrer constant, a dimensionless factor related to the crystallite shape, and is typically 0.9 for spherical crystallites. D is the crystallite size assuming cubic and monodisperse crystallites, and it is therefore important that the value of D should be interpreted with care [64, 65]. For a system of polydisperse particles, the obtained value of D represents the volume-weighted average of the particle size distribution [66]. The calculation done with the Scherrer equation is also only a relative measure that gives a rough estimate of the crystallite size and should not be used as an absolute determination. The method does not account for the effects of stress and strain, which also causes broadening of the diffraction peaks, meaning that the method should not be used if the sample has been exposed to stress [64, 65, 66]. Uncertainty in correcting

for instrumental broadening may also affect the accuracy of the calculations. This correction is done by comparing the FWHM intensity to a single-crystalline Si standard and using a Gaussian correction described in Equation 4.3.

$$B_p^2(2\theta) = B_h^2(2\theta) - B_f^2(2\theta) \tag{4.3}$$

Where $B_p^2(2\theta)$ is the corrected FWHM, $B_h^2(2\theta)$ is the FWHM of the sample, and $B_f^2(2\theta)$ is the FWHM of the Si standard [67, 64].

The crystallite size calculated using the Scherrer equation can be used to roughly estimate the dispersion, D, by using Equation 4.4.

$$D = \frac{k}{d_p} \tag{4.4}$$

Where d_p is the average crystallite diameter and the constant k changes with assumptions of particle size and shape. For internal comparisons, k may be set to a united value [68]. Since this dispersion value is calculated using the particle size obtained through the Scherrer equation, it should also not be used as an absolute determination but instead used to cross-check with other experimental results.

4.2.2 N_2 Adsorption

Surface area, pore volume, and pore size are all physical properties that can significantly impact the performance of a catalyst, and the determination of these properties is often a key part of characterizing porous catalysts. The specific surface area of the material may increase the number of active sites available for the reactant molecules to adsorb onto and react, thus increasing the rate of reaction. The size and shape of the pores significantly affect the mass transfer of reactants and products within the catalyst structure, which can influence the accessibility of the active sites, the reaction mechanism, and even the selectivity of certain products. While a high surface area is generally desirable for a heterogeneous catalyst as it often increases the number of available active sites, too high of a surface area may lead to issues with structural strength and sintering. Sintering is a physical and/or thermal process leading to the agglomeration of metal without actually melting, which in a porous catalyst can mean active sites merging to form larger particles, or even entire pores collapsing. This is an undesired process as it can cause loss of surface area and active sites, reducing the activity of the catalyst [69]. Most heterogeneous catalysts are mesoporous, meaning they have an average pore diameter between 2 and 50 nm [70].

The most common method of determining the surface area and pore size of mesoporous catalysts, is through the adsorption and desorption N_2 at 77 K, which is the boiling point of nitrogen [71]. The N2 adsorption and desorption method is based on the principle of measuring the amount of nitrogen gas adsorbed onto the surface of the porous material at various pressures and measuring how many N_2 molecules need to adsorb onto the surface to cover it with a full monolayer. In

reality, the gas molecules may adsorb in several layers, illustrated by Figure 4.2.3 [72, 73].

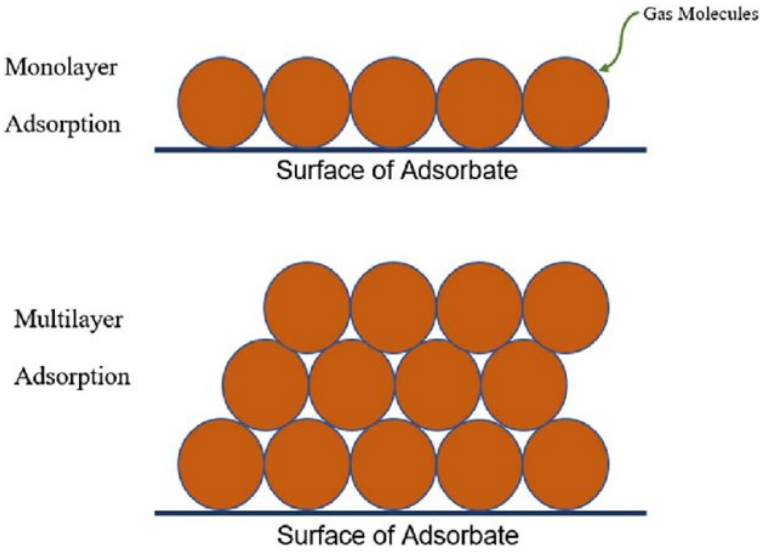

Figure 4.2.3: Illustration of monolayer versus multilayer adsorption of gas molecules on a solid surface. Obtained from Mohammed *et. al* [73].

As the pressure of N_2 increases, the amount adsorbed onto the sample is plotted versus the relative pressure p/p_0, where p is the pressure of N_2 and p_0 is the saturation pressure of N_2 at 77 K [74]. An early theory regarding isotherms was developed by Irving Langmuir in 1916, who made several assumptions to be able to describe the adsorption of a gas on a solid surface. The assumptions were the following [75]:

- The adsorption is a monolayer process, meaning that only one layer of molecules can be adsorbed onto the surface.
- All active sites on the surface have equal adsorption energy.
- Each active site can only hold one molecule.
- There is no interaction between the adsorbed molecules, meaning adsorption energy is independent of surface coverage.
- The activity of the adsorbate is directly proportional to the adsorbate concentration.

The main flaw of the Langmuir theory is that it does not account for multilayer adsorption, which as mentioned is often the case in reality. Brunauer, Emmet and Teller (BET) therefore made some additional assumptions to be able to better describe real adsorption processes [72]:

- The gas molecules will adsorb in infinite layers at saturation pressure ($p = p_0$), where molecules in the first layer act as adsorption sites for molecules in the second layer, etc.
- The enthalpy of adsorption for the second layer and higher is equal to the condensation enthalpy.
- The adsorption layers do not interact.
- The Langmuir theory can be applied to each adsorption layer.

By making these assumptions, the isotherm can be mathematically described by the BET Equation, described in Equation 4.5 [72, 76].

$$\frac{P}{V(P_O - P} = \frac{(C-1)P}{V_m C P_0} + \frac{1}{V_m C} \tag{4.5}$$

Where P is the pressure of the adsorbate gas, P_0 the saturation pressure, V_m is the volume of adsorbed gas at a full monolayer, V is the adsorbed volume at pressure P, and C is a constant. By plotting $P/(V(P\text{-}P_0))$ versus P/P_0 the slope S and intercept I of the equation can be found through least squares regression. One can then calculate V_m and the constant C, as described in Equation 4.6 and Equation 4.7 [77].

$$V_m = \frac{1}{S+1} \tag{4.6}$$

$$C = 1 + \frac{S}{I} \tag{4.7}$$

From here, the specific surface area S can be calculated as described in Equation 4.8 [77].

$$S = \frac{V_m N s}{V M} \tag{4.8}$$

Where N_S is Avogadro's number, V is the molar volume of the gas, M is the mass of the sample, and s is the cross-sectional area of the adsorbed molecules (0.162 nm^2 for N_2 at 77 K) [77].

The BET equation is linear, and thus the data points used for the calculation of surface area should be in the linear part of the graph, which represents the formation of the monolayer. This range is usually between relative pressures of 0.05 and 0.3 [30, 74].

In addition to surface area calculations, N_2 physisorption using the same equipment can also be used to determine pore volume and pore size distribution. Once the N_2 is adsorbed on the surface of the sample, the process is reversed by decreasing the pressure, letting the N_2 desorb. The following isotherm can then be used to determine to gather information about the pore structure [30]. Smaller

pores will lead to a higher rate of condensation of N_2. This phenomenon is called capillary condensation and is described by the Kelvin equation. Barrett, Joyner, and Halenda (BJH) developed a method to relate the amount of desorbed N_2, as the relative pressure decreases, to the pore size. This equation is called the modified Kelvin equation, and is described in Equation 4.9 [74, 78].

$$ln\frac{P}{P_0} = -\frac{2\sigma V cos\theta}{rRT} \tag{4.9}$$

Where P/P_0 is the relative pressure of N_2, σ is the surface tension, θ is the contact angle, T is the temperature, R is the gas constant, and r is the pore radius.

The N_2 isotherms generated by the physisorption experiment may take several different shapes, which can give useful information about the material that is being analyzed. The International Union of Pure and Applied Chemistry (IUPAC) did in 1982 define six different types of N_2 isotherms, all of which are displayed in Figure 4.2.4 [76]. The Type I isotherm usually results from microporous structures, where the pore size is so small that it governs the maximum uptake of gas molecules, which approaches a fixed value as (p/p_0) approaches 1. Type II typically represents non-porous or macroporous materials, where unrestricted monolayer-multilayer adsorption takes place. Point B represents the almost linear middle section where the monolayer is completed. The type III isotherm is rare but may be obtained from non-porous or macroporous materials with weak adsorbate interactions, and does not have a point B meaning BET analysis is not applicable. A type IV isotherm is usually obtained from mesoporous materials and is very similar to isotherm type II except it has a hysteresis loop associated with capillary condensation occurring in the mesopores. The type V isotherm is similar to type 3 except with mesopores, giving a hysteresis loop at the end. The type VI isotherm represents stepwise multilayer adsorption on non-porous surfaces [75, 76].

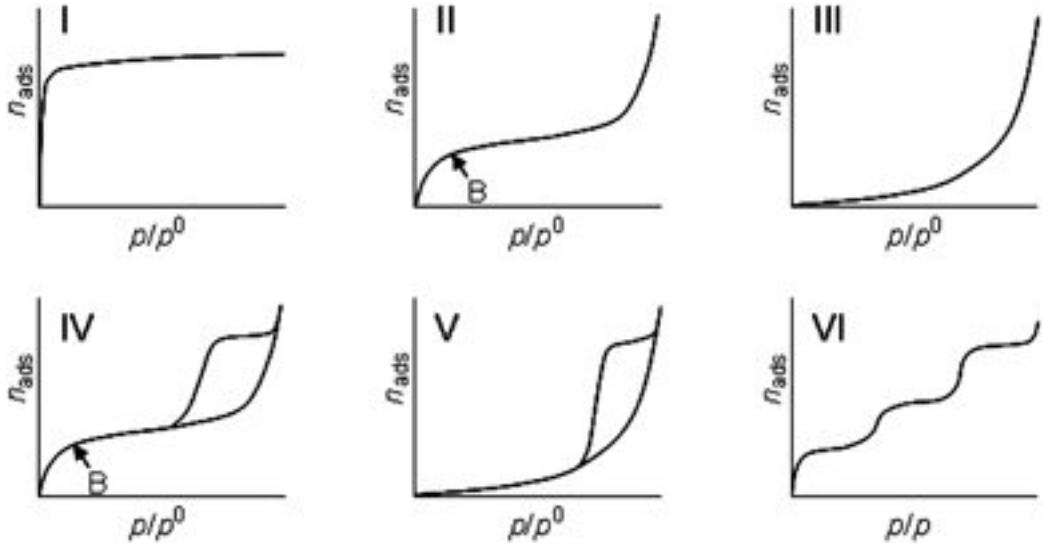

Figure 4.2.4: The six different isotherms defined by IUPAC in 1982. Obtained from Kajama *et al.*[79].

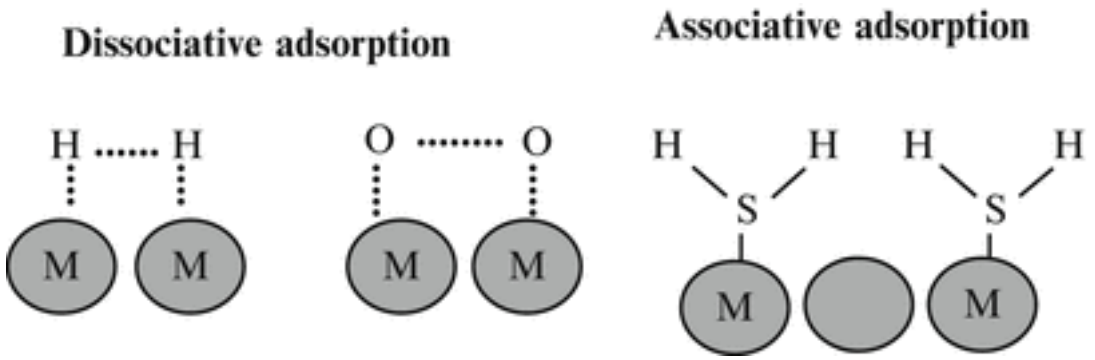

Figure 4.2.5: Dissociative and associative adsorption, obtained from Schmal [84].

4.2.3 Chemisorption

Chemisorption is a type of adsorption where the adsorbate molecules form chemical bonds with the adsorbent, like hydrogen bonds, covalent bonds, or ionic bonds [80]. Although the adsorbate molecules adsorb onto the same active sites on the catalyst as they do during the process of physisorption, the bonds formed from sharing electrons are much stronger than those formed through Van der Waal forces. This means that chemisorption requires a higher activation energy, and also that the formed bonds require more energy to be broken, leading to chemisorption typically being an irreversible process, where desorption is difficult [81, 82]. Chemisorption can typically only take place if the adsorptive is in direct contact with the surface, causing chemisorption to most often be a single-layer process [83]. Adsorbate molecules can chemisorb either associatively or dissociatively. Associative chemisorption means that the entire adsorbate molecule bonds with a single active site, while dissociative chemisorption means that the atoms in the molecules bond with different active sites, leading to different adsorption stoichiometries [80, 83]. The two concepts are visualized in Figure 4.2.5.
Due to the irreversibility of the process, chemisorption is usually undesired in catalytic processes, as the chemisorbed molecules will not desorb and therefore block the active sites for new reactant molecules [85]. Chemisorption can, however, be used to analyze several different physical properties of catalysts, like the dispersion of active metal on a support. Dispersion is the ratio of exposed surface atoms to the total number of atoms in the bulk and is mathematically defined in Equation 4.10.

$$D = \frac{N_S}{N_T} \tag{4.10}$$

Where D is the dispersion, N_S is the number of exposed surface atoms (i.e. active sites), and N_T is the total number of active metal atoms present in the catalyst. Since catalytic reactions mainly take place on the surface of the catalyst, high dispersion is typically a favorable characteristic of a catalyst, as more highly dispersed crystallites supply more active sites for reactions to take place [30, 86]. The dispersion can however also be too high, as too high dispersion can lead to crystallites that are too small to act as active sites [86].

The characterization procedure begins by completely evacuating the sample, such

that no other gas molecules are adsorbed on the sample surface prior to analysis. The analysis gas of choice may vary depending on the sample, and common analysis gases include H_2, CO, CO_2, and O_2. Once the sample is evacuated, the analysis gas is introduced at increasing pressures. There will typically be molecules that weakly adsorb (physisorb) onto the support surface, while others will strongly adsorb (chemisorb) onto the active metal sites. The initial adsorption isotherm will therefore consist of a combination of irreversible and reversible adsorption. In order to distinguish between the two, the sample is evacuated and a second adsorption test is then run. The vacuum causes the physisorbed molecules to desorb, while all that is left are the molecules that have chemisorbed onto the active metal surface. The second test is then completed under identical conditions to the first test, except now the isotherm will only consist of physisorbed molecules, since the active metal sites which allow for chemisorption are already occupied. By subtracting the second isotherm from the first, one is left with an isotherm describing chemisorption only [83]. The process is illustrated in Figure 4.2.6.

The amount of chemisorbed molecules gives information on the amount of active metal on the surface, which together with knowledge regarding the materials in question, may be used to calculate the dispersion of active metal using Equation 4.11.

$$D = \frac{n\ V_{ads} M_w * 100}{V_g M} \tag{4.11}$$

Where n is the adsorption stoichiometry, V_{ads} is the volume of chemisorbed gas, M_w is the molecular weight of the metal, M is the metal loading (%), and V_g is the molar volume of an ideal gas at STP (22414 cm^3/mol).

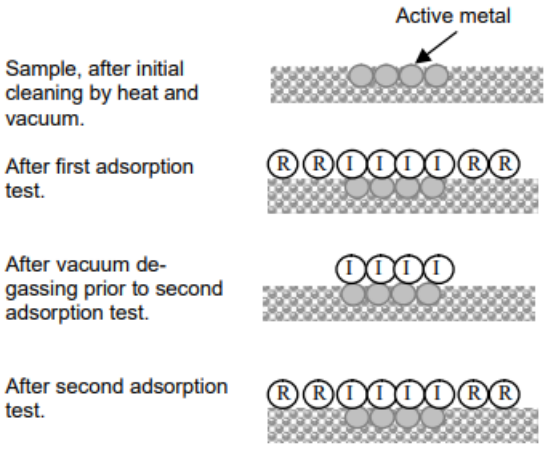

Figure 4.2.6: Four steps in determining the isotherm for only irreversible adsorption, where I and R represent irreversibly and reversibly adsorbed molecules, respectively. Obtained from Micromeritics [83]

.

4.3 Activity measurements

4.3.1 Product analysis using FTIR

Fourier-transform infrared spectroscopy (FTIR) gas analyzers are devices used to analyze the composition of gases based on their absorption and emission of infrared light. The technique relies on the principle that different gas molecules absorb and emit light at specific infrared wavelengths. creating a unique spectral fingerprint for each gas. These infrared spectra arise when transitions between quantized vibrational energy levels occur within a molecule. The molecular vibrations range from the straightforward coupled motion of the atoms in diatomic molecules to more intricate movements in larger polyfunctional molecules. Each molecule possesses its own distinctive vibrational modes, creating a unique spectral fingerprint for each gas [87].

The analyzer starts with a broadband infrared light source that emits a wide range of infrared wavelengths. The gas sample to be analyzed is then introduced into a sample cell or gas chamber. This cell is designed to allow infrared light to pass through the gas. An interferometer then splits the incoming light beam into two separate beams using a beam splitter. One beam is directed toward a fixed mirror, and the other beam is directed toward a moving mirror. The moving mirror rapidly oscillates back and forth, causing the path length of one beam to vary. The two beams are then recombined at the beam splitter, resulting in an interference pattern. The varying path length of the moving mirror creates an interference pattern that contains information about the different infrared wavelengths. The interference pattern is directed to a detector, typically a photodetector or a detector array, which measures the intensity of the light at each wavelength. This creates an interferogram. The interferogram is processed using a Fourier transform, a mathematical technique that converts the interferogram from the time domain (intensity vs. time) to the frequency domain (intensity vs. wavelength). The resulting spectrum represents the absorption and emission characteristics of the gas sample at different infrared wavelengths. As mentioned, each gas molecule has unique absorption and emission bands, allowing for the identification and quantification of the gases present in the sample. The obtained spectrum is compared to reference spectra or spectral libraries to identify the gases present in the sample. The intensities of the absorption peaks are used to determine the concentration of each gas [87, 88]. Figure 4.3.1 shows a schematic of an FTIR gas analyzer.

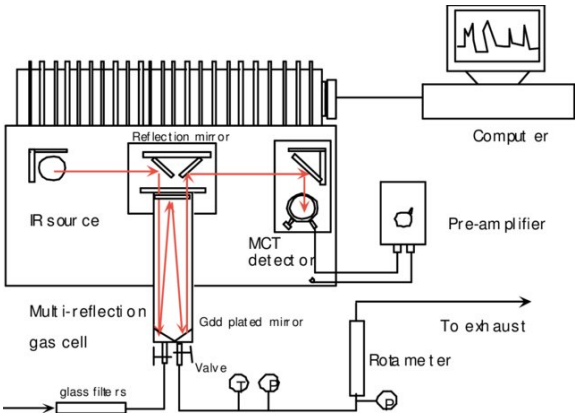

Figure 4.3.1: Schematic of an on-line FTIR gas analysis system. Obtained from Eddings *et.al.*[89].

FTIR gas analyzers have many advantages. They can simultaneously detect and quantify multiple gases in real-time, providing high sensitivity and accuracy ranging from ppb to percentages. They also require minimal sample preparation and are used in a variety of fields, including catalysis [90]. If the mirrors inside the FTIR gas analyzer are damaged or react with other compounds, the concentration measurements can contain significant amounts of noise. This issue can be solved by oxygen cleaning, making frequent service of the instrument important [87].

CHAPTER

FIVE

EXPERIMENTAL

5.1 Catalyst preparation

5.1.1 Support

γ-Al_2O_3 was used as the support for all catalysts. Pellets of 1/8" size were purchased from Alfa Aesar and crushed with a mortar and pestle. The crushed alumina was then sieved into a size fraction of 53–90 µm and calcined in a Nabertherm calcination furnace. The support was heated to 600 ^oC in air with a heating rate of 5 ^oC/min, where it was held for 2 hours before cooling down. The support was then sieved again before impregnation. N_2 physisorption and X-ray diffraction was conducted on the alumina to confirm that the phase composition (γ-Al_2O_3) and high surface area were retained.

5.1.2 Impregnation and Calcination

Seven γ-Al_2O_3-supported catalysts were prepared through wetness impregnation, a commonly used preparation method for depositing active metals on supports of alumina [13, 33, 48, 57]. Five catalysts had a 5 wt% loading of Ru with different amounts of promoters (Fe and Mn), resulting in both bimetallic and trimetallic catalysts. In addition, two monometallic catalysts of 1 wt% Fe and Mn were synthesized. Table 5.1.1 presents a summary of the composition of each catalyst synthesized in this project, along with the names which will be used to refer to the specific catalysts.

Table 5.1.1: List of names and compositions of the synthesized catalysts.

Catalyst Name	Composition
1Fe	1% Fe, 99% Al_2O_3
1Mn	1% Mn 99% Al_2O_3
5Ru1Fe	5% Ru, 1% Fe, 94% Al_2O_3
5Ru1Mn	5% Ru, 1% Mn, 94$ Al_2O_3
5Ru1Fe1Mn	5% Ru, 1% Fe, 1% Mn ,93% Al_2O_3
5Ru3Fe1Mn	5% Ru, 3% Fe, 1% Mn, 91% Al_2O_3
5Ru1Fe3Mn	5% Ru, 1% Fe, 3% Mn, 91% Al_2O_3

The amount of support and precursor required to achieve the desired metal loading was first calculated and weighed out. The precursors used for Ru, Fe, and Mn were $RuCl_3 \cdot H_2O$, $Fe(NO_3)_3 \cdot 9\,H_2O$, and $Mn(NO_3)_2 \cdot 4\,H_2O$, respectively. The precursors were then dissolved in deionized water and stirred with a magnetic stirrer for 30 minutes to ensure that the precursor was evenly dispersed. After stirring, the solution was added dropwise to the support and thoroughly mixed. The multimetallic catalysts were synthesized through co-impregnation, meaning that the precursors were dissolved in the same solution before being added to the support. The samples were then dried in an oven at 120 ^oC for 24 hours to remove the water.

Once dried, all catalysts were calcined at 450 ^{o}C for two hours, with a heating rate of 5 ^{o}C/min. 1Fe and 1Mn were calcined in air in a Nabertherm calcination furnace. All other catalysts were calcined in a dedicated calcination setup in a reducing 200 NmL/min flow of 5% H_2 in N_2. The catalysts were finally sieved into a size fraction of 53–90 µm.

5.2 Characterization techniques

5.2.1 X-ray diffraction

A DaVinci 1 X-ray Diffractometer was utilized to conduct X-ray diffraction (XRD) analysis in order to identify the various phases present within the catalysts. To prepare the samples, a small quantity of powdered sample was evenly distributed onto a 10 mm Si-cavity holder using a plastic spatula and a glass plate. This particular holder was selected due to its minimal sample requirement, ensuring that a minimum amount of spent catalyst sample was consumed for XRD, leaving more sample for other characterization methods. Cu $\varkappa\alpha$ radiation of 40 kV and 40 mA with a wavelength of 1.5405 Å was used as the radiation source, and an analysis program suitable for samples with low crystallinity was utilized. This program uses a slit opening of 0.1^o/min and a step size of approximately 0.044 ^{o}, and the diffractogram was captured in the 2ϑ range of 5-75 ^{o}. The acquired data was processed and analyzed using DIFFRAC.SUITE EVA software. Prior to plotting, the data used for the XRD plots was background subtracted and normalized. The identification and comparison of the different phases found within the catalyst samples was done by using the ICDD PDF® Database.

5.2.2 N_2 physisorption

N_2 physisorption measurements were performed to determine the specific surface area, pore volume, and pore size distribution of the catalysts. Approximately 100 mg of the sample was transferred to the bottom part of the sample tubes, before undergoing degassing pretreatment using the VacPrep 061 Degasser. The sample tubes were connected to the degassing unit and left to evacuate for one hour at room temperature. Subsequently, they were moved to the heating station and evacuated at 200 degrees overnight. After the degassing process was completed, the sample was reweighed to ensure accurate measurements.

The physisorption isotherms were obtained using a Micromeritics Tri Star 3020 Surface Area and Porosity Analyzer. To enhance temperature control, the sample tubes were covered with Teflon jackets. Additionally, a filler rod was placed inside the tubes to minimize any errors arising from free space. The sample tubes were then immersed in a dewar containing liquid nitrogen before beginning the analysis procedure. The methods chosen to calculate surface area and pore volume were Brunauer-Emmett-Teller (BET) and Barrett-Joyner-Halenda (BJH), respectively [72, 91]. A pressure range (p/p_0) of 0.05 - 0.3 was selected to ensure that only the linear portion of the isotherm was considered for calculations.

5.2.3 Chemisorption

The dispersion and particle size of the active metals on the alumina-supported catalysts were measured by CO chemisorption. The adsorption isotherms were obtained using a Micrometrics ASAP 2020 instrument. Approximately 110 mg of catalyst was placed inside a U-shaped glass reactor, sandwiched between two quartz wool pieces. O-rings were placed on the reactor outlet when connecting it to the instrument, and all parts were thoroughly cleaned with ethanol to avoid leaks. An external thermocouple was attached to the reactor for temperature control, and the sample was evacuated for 1 hour before a leak test was performed prior to analysis. The leak test consisted of closing the valves to the pump and then measuring the pressure increase for one minute - if the pressure increase was not greater than 0.05 mmHg, the system was considered leak-proof and analysis was started. The CO adsorption isotherms were recorded across the pressure range of 25-550 mmHg.

Different analysis conditions were utilized for the different catalysts, as they contained different active metals. Manganese oxides are not easily reduced to Mn^{0+} and do not respond well to H_2 treatment [45, 92], nor was there found an adsorptive which gave acceptable isotherms for the 1Mn catalyst. Several analysis procedures were tested until acceptable isotherms were obtained, and two different procedures in total were used. The procedures will be referred to as Chemisorption Analysis Procedure 1 and 2 and are described in Table 5.2.1,5.2.2, respectively. The experimental data from all chemisorption experiments, including what analysis procedure was used for what samples, can be found in Table B.1 in Appendix 7.2.

5.3 Activity testing

Activity testing was conducted in Rig 2.1 on the second floor of Chemistry Hall D at NTNU Gløshaugen, Trondheim. This rig is dedicated to studying NO oxidation under simulated industrial nitric acid plant conditions. The reactant gases consisted of NO (40% NO/Ar) and O_2 (40% O_2/Ar), and were purchased from AGA AS. The dilutant used was argon 6.0 (99.99999% Ar) which was also purchased from AGA AS. The rig has five feed gas lines connected to a ventilation network, all equipped with a check valve, a pressure gauge, a pressure-reducing valve, and a Bronkhorst electronic mass flow controller (MFC). Each gas line is individually heated to 200 ^{o}C with heating tapes prior to mixing at the reactor inlet. The

Task	**Gas**	**Temperature [^{o}C]**	**Rate [^{o}C/min]**	**Time [min]**
Evacuation	He	100	10.0	30
Leak test	-	40	10.0	-
Flow	H_2	450	10.0	120
Evacuation	-	430	10.0	60
Evacuation	-	100	10.0	45
Leak test	-	100	10.0	-
Evacuation	-	50	10.0	60
Analysis	CO	35	10.0	-
Evacuation	He	35	10.0	60

Table 5.2.1: Chemisorption Analysis Procedure 1.

Task	**Gas**	**Temperature [^{o}C]**	**Rate [^{o}C/min]**	**Time [min]**
Evacuation	He	100	10.0	30
Leak test	-	40	10.0	-
Flow	H_2	550	10.0	120
Evacuation	-	530	10.0	60
Evacuation	-	100	10.0	45
Leak test	-	100	10.0	-
Evacuation	-	50	10.0	60
Analysis	CO	35	10.0	-
Evacuation	He	35	10.0	60

Table 5.2.2: Chemisorption Analysis Procedure 2.

amount of water present in the reactor was controlled by a Bronkhorst electronic Controlled-Evaporation-Mixing (CEM) unit, which also handled the mixing of water, oxygen, and argon. A detailed flow scheme of Rig 2.1 can be found in Appendix 7.2.

Activity testing was carried out in a packed bed reactor (PBR). The reactor itself was a vertical stainless steel tubular reactor with a length of 8 cm and an inner diameter of 9.7 mm. The reactant gases entered through two separate tubes at the top of the reactor. Oxygen and water diluted in argon entered through one tube, while NO entered through the other. The reason for using two separate tubes was to minimize the contact time between oxygen and NO prior to entering the reactor, in order to minimize the gas phase NO conversion. The reactor is graphically illustrated in Figure 5.3.1.

The reactor was prepared by first inserting an approximately 1 cm long stainless steel cylinder at the bottom of the reactor, used to keep the reactor contents in place. The cylinder had a narrower opening that faced up the reactor. A pinch of quartz wool was then packed on top of the cylinder using a metal rod before the catalyst mixture was poured down the reactor inlet. Another pinch of quartz wool was placed on top of the catalyst bed to keep it in place. The catalyst mixture consisted of the catalyst itself mixed with 30 mesh (595 µm) SiC. The SiC was added to dilute the heat generated by the exothermic reaction to achieve isother-

Figure 5.3.1: Illustration of the reactor used for activity testing. Illustrated by Jithin Gopakumar.

mal conditions. The large SiC particle was chosen to make separating the spent catalyst and SiC achievable, which is necessary to characterize the spent catalyst. Approximately 500 mg of catalyst and 2.75 g of SiC was used for each test, however, these amounts were sometimes modified in order to achieve the same catalyst bed height for each activity test. The bed height is important to keep constant as it significantly impacts the contact time, i.e. the time the gas mixture is in contact with the catalyst surface and can undergo a catalytic reaction. The bed height was measured by sticking a metal rod down the reactor after adding the first piece of quartz wool and then marking the metal rod at the reactor exit. This procedure was repeated after the catalyst mixture was added, and the measured distance between the two marks on the rod was determined to be the catalyst bed height.

Two half-cylindrical aluminum blocks were placed around the reactor, equipped with four heating cartridges to ensure uniform heating. One K-type thermocouple was placed inside the heating block, while another one was placed down the reactor inside the catalyst bed to achieve accurate temperature control. A Eurotherm (2416i) controlled the temperature in the catalyst bed, while dedicated LabView software was used to control the set points of all process variables.

A total feed flow rate of 200 NmL/min was used for all activity tests, corresponding to a weight hourly space velocity (WHSV) of 24 000 NmL/hg_{cat}. The product stream was immediately diluted with 800 NmL/min Ar upon exiting the reactor in order to minimize gas phase conversion prior to concentration measurements. The dilutant also helps cool down the gas mixture to 191 ^{o}C, which is the required temperature for the gas analyzer. The gas analyzer used to analyze the product stream was a Fourier Transform Infrared (FT-IR) gas analyzer (MKS 2030HS, 1 bar, 5.11 m path length, 191 ^{o}C). A Pfeiffer Vacuum ThermoStar GSD 301 T3 Benchtop Mass Spectrometer monitored the Ar and the homonuclear diatomic compounds like O_2 and N_2.

The activity measurements presented in Section 5.3 of this report were all done without pretreatment in Rig 2.1 prior to testing. During activity testing of Ru/Al_2O_3 catalysts in the course TKP4580 - *Chemical Engineering, Specialization Project* in the fall of 2022, pretreating the catalyst bed in H_2 proved to improve catalytic activity. Those catalysts were, however, calcined in air and therefore not reduced prior to activity testing. As explained in Section 5.1.2, all catalysts synthesized in this project which contained Ru were calcined in a reducing atmosphere of 5% H_2.

Two different programs for activity testing were used in this project. The first program was used for all catalysts and consisted of a temperature ramp from 150-450 ^{o}C. The catalysts were first heated to 150 ^{o}C at 5 ^{o}C/min in Ar and held at this temperature for 30 minutes to let the temperature stabilize. The temperature was then increased to 450 ^{o}C at 5 ^{o}C/min in 10% NO, 6% O_2, and 15% H_2O, simulating nitric acid plant conditions. The second testing program was a steady state isothermal run at 360 ^{o}C, where the temperature was increased to 350 ^{o}C at 5 ^{o}C/min before being held at this temperature for 48 hours in 10% NO, 6% O_2, and 15% H_2O, in order to gauge the stability of the catalyst. The two testing programs are summarized in Table 5.3.1.

Table 5.3.1: Summary of the testing procedures used for activity testing.

Name	Temperature	Ramp Rate	Hold time	Feed Composition
450Ramp	150-450 ^{o}C	5 ^{o}C/min	-	10% NO, 6% O_2, 15% H_2O
360SS	360 ^{o}C	-	48 h	10% NO, 6% O_2, 15% H_2O

While the NO conversion was used to compare the performance of the catalysts, the gas phase conversion needs to be subtracted to determine the actual catalytic conversion, which is needed if one wishes to calculate the catalytic reaction rate. Because of this, runs with an empty reactor, only SiC (30 mesh), and SiC (30 mesh) mixed with pure alumina support (53-90 µm) were conducted in order to measure gas phase conversion and also to assess the inertness of the reactor, SiC, and alumina. The runs with only SiC used approximately 3.25 g of SiC, while the mixed run used approximately 2.75 g SiC and 0.5 g Al_2O_3. The testing program used for these tests was 450Ramp. Exact experimental details including the mass of SiC and catalyst, bed height, and test program used for all activity tests can be found in Table A.3 in Appendix 7.2 .

The conversion of NO to NO_2 was calculated by making the assumption that the only nitrogen species present in the system are NO and NO_2. This assumption lets us create a mole balance when knowing that one reacted NO molecule produces one NO_2 molecule (as shown in Equation 2.4). The mole balance is described by Equation 5.1.

$$n_{NO_{in}} = n_{NO_{2,out}} + n_{NO_{out}} \tag{5.1}$$

Where $n_{NO_{in}}$ represents the number of moles of NO entering the reactor, and $n_{NO_{2,out}}$ and $n_{NO_{out}}$ represent the number of moles of NO_2 and NO exiting the reactor, respectively. using this mole balance, the conversion of NO was calculated using Equation 5.2.

$$NO_{conversion} = \lambda * \frac{[NO_2]_{outlet}}{[NO]_{inlet}} * 100 \tag{5.2}$$

Where $[NO]_{inlet}$ is the concentration of NO at the inlet ($[NO]_{inlet} = [NO_2]_{outlet} + [NO]_{outlet}$), and $[NO_2]_{outlet}$ is the concentration of NO_2 at the outlet. λis a constant which accounts for changes in volume due to the reaction and can differ under different conditions. λ= 0.99 is typically used for nitric acid plant conditions [93].

Equation 5.3 is derived from the mole balance of a PBR on the differential form and shows how the rate of reaction can be calculated based on the mass of the catalyst.

$$r_{NO_2} = \frac{x_{NO} F_{NO,n}}{m_{cat}} \tag{5.3}$$

Where x_{NO} is the conversion of NO to NO_2, $F_{NO,n}$ is the molar flow rate of NO at the inlet, and m_{cat} is the mass of the catalyst. To find the molar flow rate of NO, 1.249 g/L is used as the density of NO (20 ^{o}C, 1 bar) [94]. In order to calculate the catalytic reaction rate, Equation 5.4 can be used.

$$r_{NO_2,c} = \frac{x_{NO,c} F_{NO,n}}{m_{cat}} \tag{5.4}$$

Where $x_{NO,c}$ is the catalytic conversion of NO, which is the measured NO conversion with the gas phase conversion subtracted, as shown in Equation 5.5.

$$x_{NO,c} = x_{NO} - x_{NO,g} \tag{5.5}$$

Equation 2.5 is based on the assumption that there are no radial gradients in reaction rate, pressure, or temperature in the PBR, which in reality is difficult to achieve experimentally. The reaction rates calculated using this equation are therefore rough estimates, and will primarily be used to compare the catalysts, rather than treating them as determined values.

CHAPTER

SIX

RESULTS AND DISCUSSION

6.1 Characterization of fresh catalyst

The following sections will present the relevant characterization results for the fresh (not yet used for activity testing) catalysts.

6.1.1 N_2 Adsorption

Table 6.1.1 shows the surface area, cumulative pore volume, and average pore diameter for the alumina-supported catalysts. The surface area is calculated by the BET method, while the pore volume and diameter are calculated by the BJH method. These methods are explained in detail in Section 4.2.2, and make numerous assumptions in order to calculate these values from measurements of N_2 adsorption/desorption. The potential inaccuracy of these assumptions is the reason for the lack of decimals in Table 6.1.1.

Table 6.1.1: Data from N2 adsorption: BET surface area, BJH desorption cumulative volume of pores, and BJH desorption average pore diameter of the fresh catalysts.

Catalyst	**BET surface area** [m^2/g]	**Pore volume [cm3/g]** [cm^3/g]	**Average Pore Size** [nm]
Al2O3	228	0.88	11
1Fe	226	0.89	11
1Mn	225	0.88	11
5Ru1Fe	224	0.86	11
5Ru1Mn	220	0.88	11
5Ru1Fe1Mn	216	0.85	11
5Ru3Fe1Mn	223	0.86	11
5Ru1Fe3Mn	228	0.86	11

The high surface area of the alumina support indicates that it is γ-Al_2O_3, confirming that the catalyst preparation methods were appropriate. As explained in Section 3.1, γ-Al_2O_3 is the desired phase of alumina when used as catalyst support, as its high surface area and thermal stability can facilitate active and stable

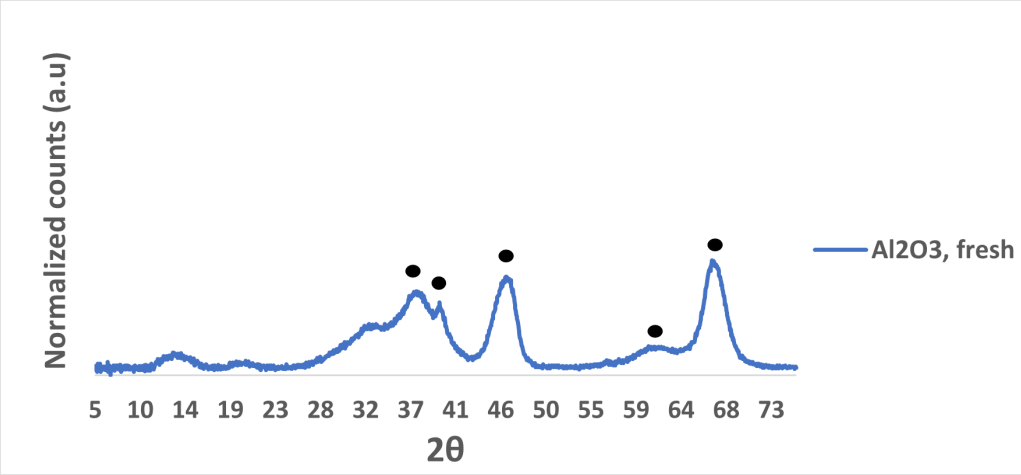

Figure 6.1.1: XRD patterns of fresh Al_2O_3-support. The γ-Al_2O_3 peaks are indicated with a dot (•).

catalysts. The pore volume of the support was determined to be 0.88 m^2/g, and the average pore diameter of 11 nm means that the support is mesoporous, which is common for heterogeneous catalysts [70]. Neither surface area, pore volume nor pore size changes significantly between the pure support and the catalysts. This validates that the desired characteristics of γ-Al_2O_3 are retained through impregnation and calcination.

The plot of the isotherm for the alumina support can be found in Figure B.1 Appendix 7.2, along with the BET surface area plot and pore size distribution plot. The isotherm appears to be a Type II isotherm, which is explained in detail in Section 4.2.2. This isotherm is suitable for BET surface area calculations, as the linear plateau of the isotherm fits the linear BET equation (Equation 4.5 well [75, 76]. The range of partial pressures (p/p_0) used for calculations was 0.05-0.3 p/p_0, which by looking at the isotherm in Figure B.1 Appendix 7.2 is within the linear region of the plot. This indicates that the chosen range of partial pressures was appropriate for surface area calculations. The pore volume and average pore size were calculated using the Kelvin equation (Equation 4.9) on the measured desorption of N_2.

6.1.2 X-ray diffraction

Figure 6.1.1 shows the fresh alumina support's X-ray diffraction (XRD) pattern. The diffractogram confirms the presence of γ-Al_2O_3 by comparing with PDF #00-029-0063, with distinct peaks at 37.59^o, 39.47^o, 45.84^o, 60.60^o and 67.00^o. This is the desired alumina phase for the catalyst, as the high surface area and thermal stability make it a suitable catalyst support [29, 31]. The broad peaks indicate that the material is semi-crystalline, which is common for γ-Al_2O_3 [13].

Figure 6.1.2 shows the normalized XRD patterns of the fresh 1Fe and 1Mn catalysts. When comparing with the diffraction pattern of the pure alumina support in Figure 6.1.1, it is clear that the patterns are identical, with no visible peaks associated with iron or manganese. This is often an indication of small crystallite

size and/or high dispersion, which is common for catalysts with low metal loading like 1 wt% [63, 95]. Reed *et al.* found that catalysts with less than 10 wt% Mn showed little to no evidence of crystalline MnO_x in XRD patterns, which is in accordance with these findings.

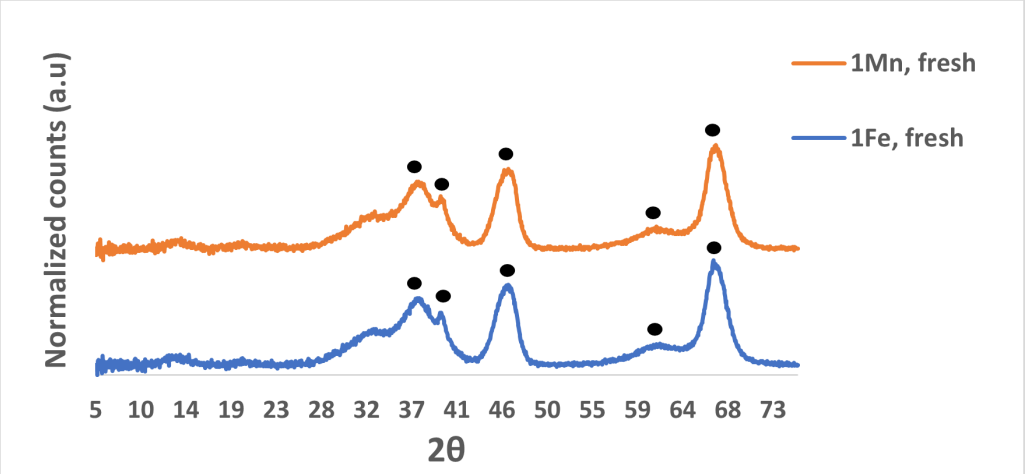

Figure 6.1.2: XRD patterns of fresh 1Fe and 1Mn.

Figure 6.1.3 shows the normalized XRD patterns of 5Ru1Fe and 5Ru1Mn. The diffraction pattern confirms the presence of Ru^0 by matching with PDF #00-006-0663, with new peaks at 38.39^o, 42.14^o, 44.00^o, 58.23^o, and 69.41^o. All new peaks are associated with metallic Ru and not RuO_2, confirming that the Ru on the catalysts was fully reduced. This was the aim of the catalyst preparation, as Ru/Al_2O_3 catalysts tested in the project course TKP4580 - *Chemical Engineering, Specialization Project* in the fall of 2022 showed significantly higher activity in NO oxidation when reduced to Ru^0 prior to testing.

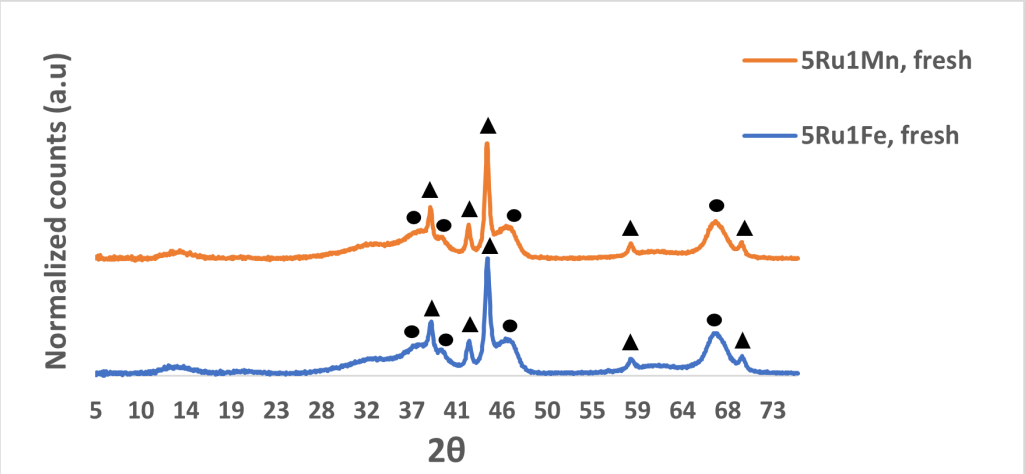

Figure 6.1.3: XRD patterns of fresh 5Ru1Fe and 5Ru1Mn. The distinct γ-Al_2O_3 peaks are indicated with a dot (•), while the Ru^0 peaks are indicated with a triangle (▲).

Figure 6.1.4 shows the normalized XRD patterns of 5Ru1Fe1Mn, 5Ru3Fe1Mn, and 5Ru1Fe3Mn. The peak positions are identical to the bimetallic catalysts, with only Ru^0 and γ-Al_2O_3 peaks present. The only significant difference between

the diffraction patterns is the peak heights. The counts are normalized, meaning the height of the Ru peaks can be assessed by comparing them with the height of the alumina peaks. The Ru peak intensity decreases in the order of 5Ru1Mn3Fe > 5Ru3Fe1Mn > 5Ru1Fe1Mn, indicating a trend in increased peak intensity with increased metal loading. Higher peak intensity may indicate larger crystallites/lower dispersion, a common effect of increased active metal loading [95].

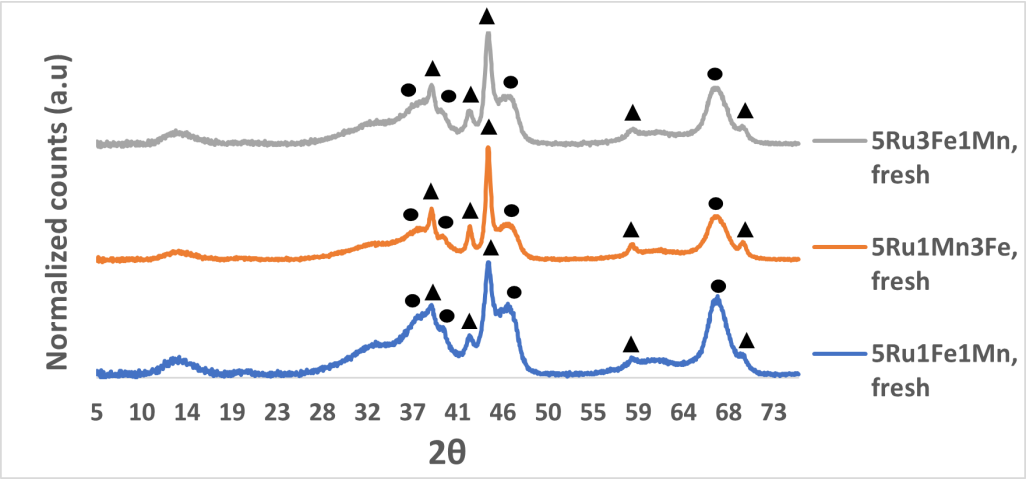

Figure 6.1.4: XRD patterns of fresh 5Ru1Fe1Mn, 5Ru1Fe3Mn, and 5Ru3Fe1Mn.. The distinct γ-Al_2O_3 peaks are indicated with a dot (•), while the Ru^0 peaks are indicated with a triangle (▲).

To further investigate the relationship between catalyst composition and crystallite size, the Scherrer equation (Equation 4.2) was used to estimate the size and dispersion of the Ru crystallites. As explained in Section 4.2.1, the Scherrer equation is based on numerous assumptions and the calculated values should not be considered determined sizes, but rather used for internal comparisons of catalysts [64, 65]. The values will also be compared with the crystallite size and dispersion measured by CO chemisorption. Since Ru was the only metal that displayed peaks on the diffraction pattern, only Ru crystallite size and dispersion will be estimated from XRD. The peak used for calculations was the (101) peak at $2\vartheta = 44^o$, with $\lambda = 1.5405$ Å. The shape factor used was 0.9 assuming spherical particles, and Equation 4.4 described in Section 4.2.1 was used to calculate dispersion for internal comparison, with k = 1. The results are summarized in Table 6.1.2. Average crystallite sizes range between 12 and 20 nm, and there is no trend of an increase in crystallite size (or decrease in dispersion) with increased metal loading. This indicates that promoting Ru with Fe and Mn is possible without compromising the dispersion of Ru, which in other reactions has been linked to higher catalytic activity [96, 97]. Maintaining high dispersion is typically desirable, as higher dispersion allows for a higher number of available active sites.

Table 6.1.2: Crystallite size and dispersion of Ru on fresh catalysts calculated using the Scherrer equation (Equation 4.2).

Catalyst	Crystallite Size [nm]	Dispersion [%]
5Ru1Fe	17	6 %
5Ru1Mn	20	5 %
5Ru1Fe1Mn	12	8 %
5Ru3Fe1Mn	12	8 %
5Ru1Fe3Mn	17	6 %

6.1.3 Chemisorption

Dispersion of active metal and crystallite size was measured by CO chemisorption. While chemisorption is a commonly used characterization method for heterogeneous catalysts, it can often become challenging when used for catalysts containing several active metals. Finding a single adsorptive gas that adsorbs well onto all active metals is not always possible, as different gases interact differently with different metals. Choosing pretreatment conditions which suit all of the active metals can also be difficult, as some metals may require different reduction temperatures, and some metals do not respond well to any reduction at all [81, 98]. The interaction of adsorptive properties between the metals can also be a source of uncertainty. Paryjczak *et al.* [98] studied the adsorptive properties of $Ag-Rh/Al_2O_3$ catalysts in relation to chemisorption of H_2, O_2, and CO. They found that the interaction between the metals was complicated, they could not conclude that chemisorptive properties of the metals were additive. They proposed that the differences from ideal behavior could stem from changes in the composition of the bimetallic surface and/or varying adsorption stoichiometry. It is important to thoroughly consider these issues when conducting chemisorption on bi and trimetallic catalysts, and trial and error through repeated experiments may often be necessary to gain insight into the behavior of the adsorptive.

A CO chemisorption analysis procedure for Ru/Al_2O_3 catalysts was found in literature, and proved successful also for the catalysts presented in this work [97]. The adsorptive gas found consistently successful for chemisorption on Ru was CO, which therefore was chosen as adsorptive for the catalysts presented in this work. A CO:Ru adsorption stoichiometry of 0.6:1 was used, as proposed by Borodzinski and Bonarowska [95].

Determining the dispersion of Mn on the alumina support through chemisorption proved challenging, as no common and successful analysis procedure for chemisorption measurements on MnO_x/Al_2O_3 catalysts was found in literature. Several different procedures and adsorptive were tested on the 1Mn catalyst to investigate the possibilities of determining the dispersion of Mn, but none proved consistently successful in obtaining an isotherm valid for calculations. For chemisorption isotherms to be considered appropriate for dispersion and crystallite size determination, it is crucial that the first analysis isotherm has a higher volume adsorbed than the repeat analysis isotherm at all pressures, and that the volume adsorbed

always increases with increasing pressure. Any deviation from this would contradict the principles of chemisorption and make calculations invalid. The theory behind these principles is explained in detail in Section 4.2.3. No analysis procedure resulted in consistently appropriate isotherms for the 1Mn catalyst and as a result, chemisorption was deemed unfit for determination of dispersion and crystallite size of Mn. While analysis procedures for chemisorption on Fe have been reported in the past, no successful procedure using CO gave desirable isotherms for the 1Fe catalyst. When comparing the volume of adsorbed CO of the 1Mn and 1Fe catalysts and the Ru catalysts, it was clear that Mn and Fe adsorbed a significantly smaller amount of CO compared to that of the catalysts containing Ru. It was therefore decided that chemisorption may be performed on the other catalysts to estimate the dispersion and crystallite size of Ru, excluding Mn and Fe from the calculations. An example of the problematic isotherms obtained from chemisorption on 1Mn, as well as an example of appropriate isotherms obtained from the other catalysts can be found in Figure **??** and **??** Appendix 7.2.

The dispersion and crystallite size of Ru on the fresh catalysts measured by CO chemisorption is presented in Table 6.1.3. The dispersion ranges between 5% and 7% and does not significantly change with increased metal loading. The dispersion of un-promoted 5 wt% Ru/Al_2O_3 was measured by CO chemisorption in the course TKP4580 - *Chemical Engineering, Specialization Project* in the fall of 2022 an was found to be 6%. Comparison of that value with the results presented in Table 6.1.3 indicates that that promoting Ru/Al_2O_3 with Mn and Fe does not reduce the dispersion of Ru. Decrease in dispersion and increase in crystallite size through sintering or agglomeration can be a common effect of increasing the metal loading, and can contribute to catalyst deactivation through loss of active sites [99, 100, 69]. The absence of such a mechanism through doping of the 5 wt% Ru/Al_2O_3 with Fe and Mn is promising for the doping Ru with several active metals without losing key catalyst properties.

Table 6.1.3: Dispersion and crystallite size of Ru on fresh catalysts measured by CO chemisorption.

Catalyst	Dispersion [%]	Crystallite Size [nm]
5Ru1Fe	5	24
5Ru1Mn	6	21
5Ru1Fe1Mn	7	19
5Ru3Fe1Mn	7	17
5Ru1Fe3Mn	7	20

Experimental uncertainties in the determination of dispersion and crystallite size exist in both XRD and CO chemisorption, and comparing the results from the two characterization methods is therefore important. While the values were not identical, the crystallite sizes determined by the two methods were within the same range and did not show any clear trend with changes in metal composition. While there is still some degree of experimental error and uncertainty in these results, the general agreement between the two methods implies that the dispersion and crystallite size measurements are appropriate for describing these features of the catalysts presented in this work.

6.2 Activity testing

6.2.1 Experimental Challenges

Catalytic activity was measured by the conversion of NO. The experimental setup was designed to minimize errors to achieve as accurate and consistent measurements as possible. Several modifications of Rig 2.1 have been made to optimize the design, and the preparation and testing procedures were kept as consistent as possible for all catalysts. Every catalyst was loaded into the reactor in the same way, with bed height being measured and kept constant for every test. The reactor was always inserted into the rig in the same way, and the same programs were used for each catalyst, with a constant flow rate and feed composition, resembling nitric acid plant conditions. There are, however, still some experimental challenges that should be addressed.

The rate expression for gas phase NO oxidation presented in Equation 2.5 in Section 2.2 shows that the reaction rate has a second-order dependence on the partial pressure of NO and a first-order dependence on the partial pressure of oxygen. This means that the reaction rate, and thus conversion, increases with increased pressure of NO and O_2. The conversion data can therefore be significantly impacted by pressure drop inside the reactor, especially since the partial pressure term of NO, p_{NO}, is squared. Due to the small catalyst particle size (53–90 µm), packing the catalyst too tight can lead to pressure drop. The SiC particles used are also much larger (595 µm) than the catalyst particles. This may cause the mixture of SiC and catalyst to be unevenly distributed through the catalyst bed, potentially creating temperature and/or pressure gradients. In the activity measurements done in Rig 2.1 for published papers, SiC particles of similar size (53–90 µm) were used to avoid this issue [13, 19]. Using the same size fraction does however make it difficult to separate the SiC and spent catalyst, which is necessary for the characterization of spent catalyst. This means that in order to achieve conversion data from runs with similar size SiC and catalyst while also characterizing spent catalyst, twice the number of activity tests would be necessary (one run for conversion data, one for creating spent catalyst). This project only runs across one semester and is therefore limited in time and resources, so it was decided to only use 30 mesh (53–90 µm) SiC particles.

Monitoring and evaluating how tightly packed and homogeneous the catalyst bed is difficult, as the stainless steel reactor is not see-through. One possible solution to this would be to use a reactor made of quartz or glass, which would also allow for more accurate measurements of bed height. This would however require rubber seals to connect the glass to the steel piping, and these cannot withstand temperatures above 200 ^{o}C. Increasing the reactor length would move the seals further away from the hot catalyst bed, but this would lead to a longer pathway for the feed gas, increasing gas phase conversion. It has therefore been decided that a short, stainless steel reactor is the most optimal for accurate activity measurements. The pressure in the system is also recorded and displayed inside the rig, and this pressure was checked at the start of each experiment to check for pressure build-up. Suspiciously high conversion at low temperatures also indicated issues

regarding pressure, and many activity tests were redone to ensure that all conversion data is obtained at 1 bar pressure.

Potential sources of error in temperature measurements also exist within the system. Temperature gradients increase with increased bed height, which the large SiC particles and low density of alumina contribute to. In addition, the thermocouple which records the catalyst bed temperature is only capable of measuring the temperature at one point of the bed, meaning that it is difficult to determine if the temperature is different in other areas of the reactor. The exothermic reaction also releases heat, but the SiC dilutes this heat to minimize the impact this has on potential temperature gradients.

Gas phase conversion between the reactor effluent and FTIR gas analyzer is also a concern. The gas needs to travel a significant distance while also being cooled down to 191 ^{o}C, as the gas analyzer cannot handle higher temperatures [90]. This can potentially facilitate significant gas phase conversion, however, the issue is to a high degree solved by heavily diluting the gases in Ar at the reactor effluent (Ar/reactor effluent = 4). As mentioned in Section 4.3.1, the concentration measurements made by the FTIR gas analyzer will also contain an increasing amount of noise. The water and NO_2 in the system produce some nitric acid over time, which reacts with the gold-plated mirror in the FTIR gas analyzer. This noise can be removed by cleaning the mirrors with oxygen, only done by the distributors (MKS) during service. The majority of the activity measurements done in this project contained significant amounts of noise, and the activity data presented in this work has been smoothened using the "Exponential Smoothing" tool in Microsoft Excel. A comparison of a plot of raw data and the smoothened data can be found in Figures C.2 and C.1 Appendix 7.2. Images of the contaminated mirror can be found in Appendix 7.2.

In summary, the experimental design is optimized to minimize errors in activity measurements, but there are still significant uncertainties regarding conversion measurements and the control of temperature and pressure. It is therefore difficult to ensure a homogeneous system and steady-state conditions, making calculations of values like kinetic parameters and reaction orders untrustworthy. The errors and uncertainties are however similar for every test, allowing for accurate comparison and evaluation of catalyst performance.

6.2.2 Mass Transfer Limitations

When studying catalytic activity, it is important to ensure that the reaction rate is not limited by mass transfer limitations, such that the recorded measurements represent actual catalytic activity. Salman *et al.* studied the catalytic oxidation process of NO to NO_2 for the production of nitric acid in the same rig and testing conditions used in this work [20]. They used a Pt/Al_2O_3 catalyst and 53-90 µm SiC particles. The absence of internal diffusion limitations in the system under these conditions was confirmed by using the Weisz-Prater criterion [101]. Salman *et al.* also assessed the presence of external mass and heat transfer limitations by calculating the Carberry number (Ca) and employing criteria proposed by Mears

[102]. The calculations revealed no external limitations as the Ca number was determined to be on the order of 10^{-5}, which is far below the limit of 0.05 [20]. Due to the large margin of safety of these initial estimations, it was assumed that the same experimental setup, albeit with a different catalyst and varying particle size of SiC, would also be free from internal diffusion limitations and external mass and heat transfer limitations at these conditions.

6.2.3 Gas Phase Conversion Measurements

The oxidation of NO to NO_2 is a reaction that favors high pressure and low temperature, as explained in detail in Section 2.2. The homogeneous gas phase conversion was measured in the same experimental setup as the catalysts but without a catalyst present. Several different gas phase conversion measurements were made. One test was with a completely empty reactor (ERE), and one was with 3.25 g of SiC, in order to confirm the inertness of SiC. One test was run with a mixture of 2.75 g of SiC and 0.5 Al_2O_3, to measure any potential catalytic activity of the support, and also to more accurately simulate the gas flow conditions when the reaction is run with catalysts. The alumina and SiC bed may lead to small changes in pressure that will also occur with a catalyst bed present, which can significantly affect the highly pressure-dependent reaction. The results from these runs also served as baselines for the onset of catalytic activity, and were used to subtract from total conversion to determine the catalytic conversion of the catalysts. The baseline was also used to check for pressure build-up during the catalyst runs. If the total conversion of the catalyst at low temperatures was significantly higher than the gas phase conversion, it indicated that there may have been pressure build-up, and the test had to be repeated.

Figure 6.2.1 shows the conversion of NO as a function of temperature from 150-450 ^{o}C at 1 bar pressure, with a ramp rate of 5 ^{o}/min and WHSV = 24 000 $\mathrm{NmL/h \cdot g_{cat}}$.

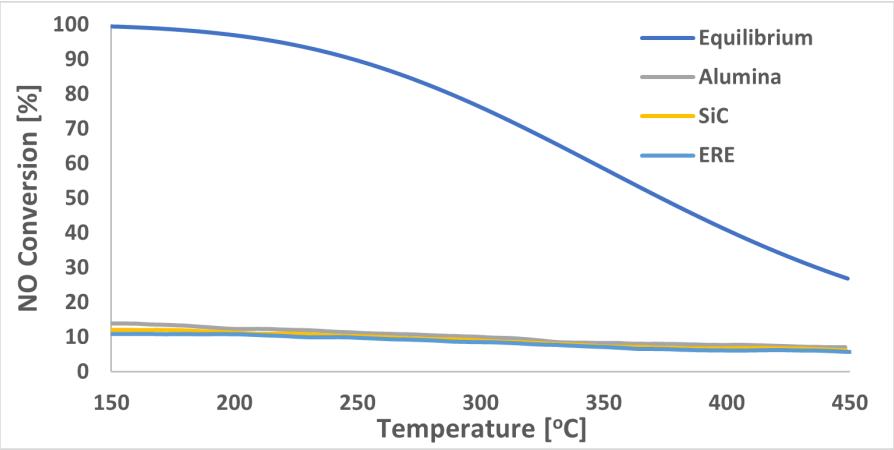

Figure 6.2.1: Conversion of NO as a function of temperature from 150-450 ^{o}C for an empty reactor, 3.25 g of SiC, and a mixture of 2.75 g SiC and 0.5 g Al_{2O3}. The blue line represents the maximum NO conversion (i.e. level of NO_2) considering the thermodynamic equilibrium at 1 bar pressure.

Figure 6.2.1 shows the trend of gas phase NO oxidation. As temperature increases, the conversion of NO decreases due to the negative rate as constant explained in Section 2.2. The empty reactor, SiC, and SiC/Al_2O_3 all follow this trend, as their curves are almost identical. There is a slight increase in conversion in the order of ERE < SiC < SiC/Al_2O_3, however, this difference is minuscule and independent of temperature. If the difference in conversion was due to SiC or Al_2O_3 being catalytically active, the conversion would increase with increasing temperature, as catalytic activity typically increases with temperature. The slight difference is therefore most likely due to a slight pressure increase when the reactor is filled with SiC/Al_2O_3, and both components are assumed catalytically inactive in NO oxidation. While an active support can be useful for increasing the catalytic activity of the catalysts, it is important that the reactor itself and the dilutant SiC are inert such that measured activity only comes from the catalyst itself.

6.2.4 Effect of Temperature on NO Conversion

The presentation of conversion as a function of temperature is subject to uncertainties arising from several factors related to the experimental design, as described in the previous sections. However, the results aim to present the differences between the catalysts and their performance under NO oxidation. In relation to the limitations associated with reaching true steady state, accurate temperature measurements, and pressure drop in the catalyst bed, it is arguable that calculating kinetic properties like activation energy from these results would not yield meaningful values.

For evaluation of the catalysts that displayed significant amounts of activity, the effect of temperature on the catalytic performance will be presented as catalytic conversion of NO, $x_{NO,c}$. Equation 5.5 in Section 5.3 was used for calculations, and the gas phase conversion data was extrapolated to fit the conversion data of the catalysts.

Plots of the total conversion without the gas phase subtraction for each catalyst are presented in Appendix 7.2. The catalyst bed height and mass of SiC and catalyst used for each activity measurement can be found in Table C.1 Appendix 7.2. The activity measurement programs used for the results presented in the following sections are described in detail in Section 5.3.

6.2.4.1 Iron and Manganese Catalysts

In addition to the promoted Ru/Al_2O_3 catalysts, 1 wt% Fe/Al_2O_3 (1Fe) and 1 wt% Mn/Al_2O_3 (1Mn) were synthesized and tested for catalytic activity in NO oxidation. These two catalysts were not synthesized and tested based on expectations of them achieving NO conversions higher than the Ru/Al_2O_3 catalysts, but rather to investigate the activity of Fe and Mn in NO oxidation both as promoters and as exclusive active metals. It was believed that trends in the NO conversion for 1Fe and 1Mn could contribute to explaining the promoter effect on the catalytic activity of the promoted catalysts. Figure 6.2.2 shows the total NO conversion as

a function of temperature for 1Fe and 1Mn. It was decided to plot the total and not catalytic conversion for these two catalysts, due to them displaying little to no catalytic activity. The gas phase conversion is therefore also included in the plots for reference.

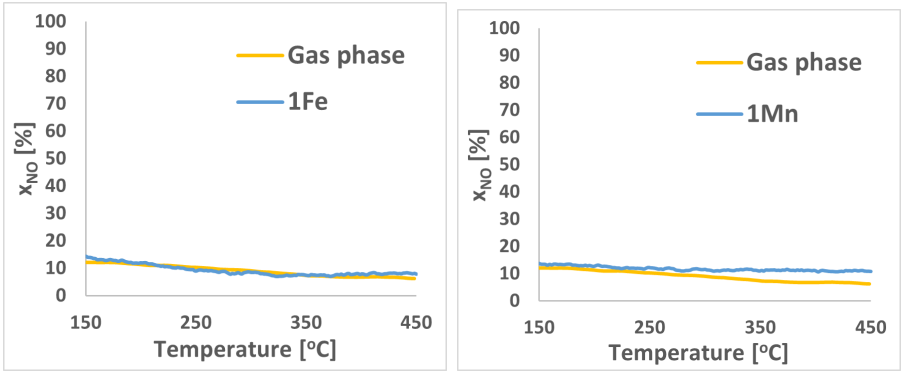

(a) Total conversion of 1Fe. **(b)** Total NO conversion of 1Mn.

Figure 6.2.2: Total NO conversion, x_{NO} (%), of 1Fe and 1Mn in 10% NO, 6% O_2, 15% H_2O from 150-450 ^{o}C with a ramp rate of 5 ^{o}C/min, pressure of 1 bar, and WHSV = 24 000 NmL/h$\cdot g_{cat}$. The yellow line represents the gas phase conversion.

Figure 6.2.2 shows that 1Fe displays no catalytic activity across the entire temperature range, as the conversion line is effectively identical to the gas phase conversion line. 1Mn begins to show signs of catalytic activity above 300 ^{o}C, albeit in minor amounts. The difference between the total NO conversion of 1Mn at higher temperatures and the gas phase conversion is so small that it is not safe to conclude that it is due to catalytic conversion and not inaccuracy caused by the experimental design, like pressure build-up in the reactor. An argument for the conversion originating from catalytic conversion and not pressure increase is that it increases with increasing temperature, a common trend of catalytic activity. These results indicate that Mn might be more active than Fe towards catalytic oxidation of NO, however, the effect of these metals as promoters on Ru could still differ. Due to the negligible level of catalytic activity of 1Fe and 1Mn, they will not be included in calculations and comparisons in the following sections.

6.2.4.2 Bimetallic Promoted Ru Catalysts

Figure 6.2.3 presents the catalytic conversion $x_{NO,c}$ for 5Ru1Fe and 5Ru1Mn as a function of temperature in the range 150-450 ^{o}C. Comparing the results of these two catalysts will indicate how promoting Ru with either one of Fe and Mn affects catalytic activity. The two catalysts show a similar trend of catalytic activity starting around 350 ^{o}C, and the activity is as expected much higher than for 1Fe and 1Mn due to the presence of Ru.

Table 6.2.1 presents the catalytic conversion and estimated catalytic reaction rate for 5Ru1Fe and 5Ru1Mn at 375 ^{o}C and 425 ^{o}C. The reaction rate was calculated using Equation 5.4 in Section 5.3, and an example of the calculation is demon-

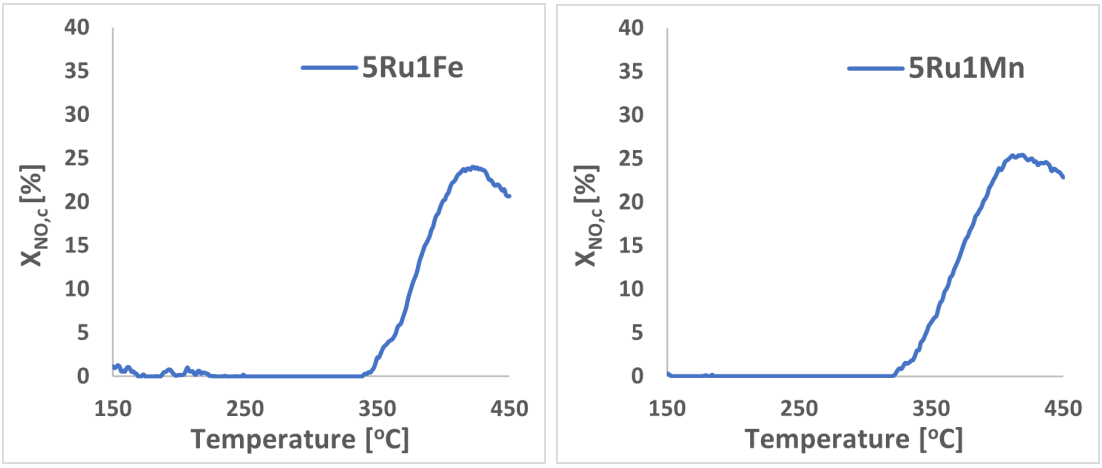

(a) Catalytic NO conversion of 5Ru1Fe. **(b)** Catalytic NO conversion of 5Ru1Mn.

Figure 6.2.3: Catalytic NO conversion, $x_{NO,c}$ (%), of 5Ru1Fe and 5Ru1Mn in 10% NO, 6% O_2, 15% H_2O from 150-450 ^{o}C with a ramp rate of 5 ^{o}C/min, pressure of 1 bar, and WHSV = 24 000 NmL/h $\cdot$ g_{cat}.

strated in Appendix 7.2. The catalytic reaction rates should not be taken as determined values due to experimental uncertainties explained in Section 6.2.1, but should rather be used for internal comparison of catalytic performance. Table 6.2.3 shows that 5Ru1Mn produces a significantly higher conversion and reaction rate at 375 ^{o}C compared to 5Ru1Fe (about 1.5 times higher), however, the values are almost identical at 425 ^oC. This indicates that the promotion of Ru with Mn increases catalytic activity at lower temperatures compared to the promotion with Fe, even though they reach similar conversions at the highest temperatures. Both ruthenium and manganese catalysts have previously shown activity for NO oxidation at low temperatures under conditions relevant to industrial nitric acid production, which is further supported by these results [19, 18].

Table 6.2.1: Catalytic conversion, $x_{NO,c}$ (%) and estimated catalytic reaction rate, $r_{NO2,c}$ (mol/($g_{cat} \cdot s$) for 5Ru1Fe and 5Ru1Mn at 375 ^{o}C and 425 ^{o}C.

Catalyst	$\mathbf{x_{NO,c,375}}$ [%]	$\mathbf{x_{NO,c,425}}$ [%]	$\mathbf{r_{NO2,c,375}}$ [mol/($g_{cat} \cdot s$]	$\mathbf{r_{NO2,c,425}}$ [mol/($g_{cat} \cdot s$]
5Ru1Fe	10	24	6.5E-05	1.7E-04
5Ru1Mn	15	25	9.8E-05	1.7E-04

The catalytic conversion's dependency on temperature for 5Ru1Fe and 5Ru1Mn are presented in Table 6.2.2. The temperature dependency is evaluated as the slope of the catalytic conversion across two ranges of temperature, 350-400 ^{o}C and 375-425 ^{o}C. The slope is calculated by linear regression, and the calculation method along with the respective R^2 values is given in Table **??** in Appendix 7.2. The results show that the catalytic activity of 5Ru1Fe has a higher dependency on temperature compared to 5Ru1Mn, especially at higher temperatures. The results from activity testing of the bimetallic catalysts indicate that manganese is a better promoter than iron in Ru/Al_2O_3 catalysts for oxidation of NO at lower temperatures.

Table 6.2.2: Temperature dependency of the catalytic activity for 5Ru1Fe and 5Ru1Mn presented as the slope of catalytic NO conversion $x_{NO,c}$ as a function of temperature in the ranges 350-400 ^{o}C and 375-425 ^{o}C.

Catalyst	**Temperature Dependency** (350-400 ^{o}C)	**Temperature Dependency** (375-425 ^{o}C)
5Ru1Fe	0.39	0.32
5Ru1Mn	0.35	0.25

6.2.4.3 Trimetallic Promoted Ru Catalysts

Figure 6.2.4 presents the catalytic conversion $x_{NO,c}$ for 5Ru1Fe1Mn, 5Ru3Fe1Mn, and 5Ru1Fe3Mn as a function of temperature in the range 150-450 ^{o}C. The comparison of the catalytic activity of these catalysts may provide insight into how the Fe/Mn ratio of promoters affects the catalytic activity of alumina-supported Ru catalysts. The catalytic conversion appears to reach its maximum at higher temperatures with increased loading of Fe. In fact, the conversion of 5Ru3Fe1Mn seems to still be rising at 450 ^{o}C, meaning it would most likely reach a higher conversion at a higher temperature if the temperature program was modified. The aim of this work is however not to achieve the highest possible conversion regardless of temperature, but rather to find catalysts suitable for low-temperature catalytic oxidation of NO at industrial nitric acid conditions. At higher temperatures, the reaction is limited by the thermodynamic equilibrium of NO and NO_2 (explained in Section 2.2). Any catalyst that could possibly be suitable for industrial NO oxidation will therefore have to be catalytically active at lower temperatures. 5Ru1Fe3Mn does appear to generate some catalytic conversion at temperatures as low as 250 ^{o}C. Although the conversion stays low until it reaches higher temperatures, it may indicate that higher loading of Mn increases catalytic activity at lower temperatures compared to Fe.

Table 6.2.3 presents the catalytic conversion and estimated catalytic reaction rate for 5Ru1Fe1Mn, 5Ru3Fe1Mn, and 5Ru1Fe3Mn at 375 ^{o}C and 425 ^{o}C. The reaction rate was calculated using Equation 5.4 in Section 5.3, and an example of the calculation is demonstrated in Appendix 7.2. The catalytic reaction rates should not be taken as determined values due to experimental uncertainties explained in Section 6.2.1, but should rather be used for internal comparison of catalytic performance. 5Ru1Fe1Mn exhibits the highest conversion and reaction rate at both temperatures, with the difference being the largest at 425 ^{o}C.

Table 6.2.3: Catalytic conversion, $x_{NO,c}$ (%) and estimated catalytic reaction rate, $r_{NO2,c}$ (mol/($g_{cat} \cdot s$) for 5Ru1Fe1Mn, 5Ru3Fe1Mn, and 5Ru1Fe3Mn at 375 ^{o}C and 425 ^{o}C.

Catalyst	$\mathbf{x_{NO,c,375}}$ [%]	$\mathbf{x_{NO,c,425}}$ [%]	$\mathbf{r_{NO2,c,375}}$ [mol/($g_{cat} \cdot s$]	$\mathbf{r_{NO2,c,425}}$ [mol/($g_{cat} \cdot s$]
5Ru1Fe1Mn	8	22	5.3E-05	1.6E-04
5Ru3Fe1Mn	4	14	2.8E-05	1.0E-04
5Ru1Fe3Mn	7	15	2.8E-05	1.0E-04

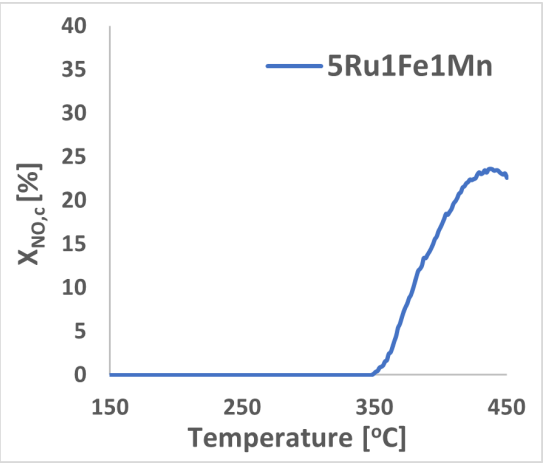

(a) Catalytic NO conversion of 5Ru1Fe1Mn.

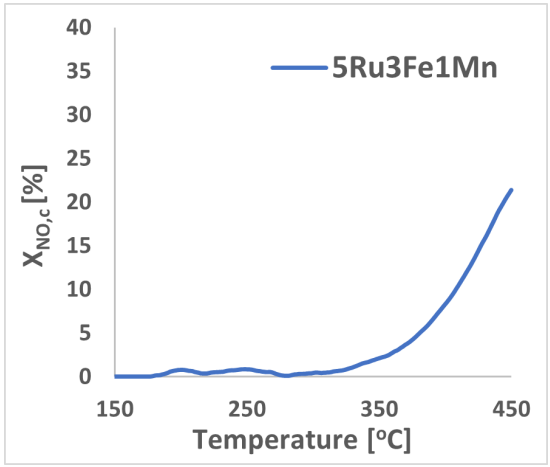

(b) Catalytic NO conversion of 5Ru3Fe1Mn.

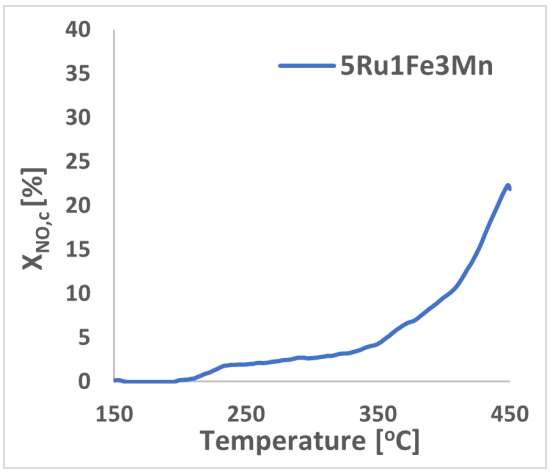

(c) Catalytic NO conversion of 5Ru1Fe3Mn.

Figure 6.2.4: Catalytic NO conversion, $x_{NO,c}$ (%), of 5Ru1Fe1Mn, 5Ru3Fe1Mn, and 5Ru1Fe3Mn in 10% NO, 6% O_2, 15% H_2O from 150-450 ^{o}C with a ramp rate of 5 ^{o}C/min, pressure of 1 bar, and WHSV = 24 000 NmL/h $\cdot$ g_{cat}.

The catalytic conversion's dependency on temperature for 5Ru1Fe1Mn, 5Ru3Fe1Mn, and 5Ru1Fe3Mn are presented in Table 6.2.4. The temperature dependency is evaluated as the slope of the catalytic conversion across two ranges of temperature, 350-400 ^{o}C and 375-425 ^{o}C. The slope is calculated by linear regression, and the calculation method along with the respective R^2 values is given in Table **??** in Appendix 7.2. It is clear that 5Ru1Fe1Mn is the most temperature-dependent catalyst in terms of catalytic conversion, while 5Ru1Fe3Mn is the least. This means that while 5Ru1Fe1Mn exhibits the highest catalytic activity in total, it is also the most dependent on temperature, as it shows no catalytic activity at all below 350 ^{o}C. While the trimetallic catalysts do slightly differ in catalytic activity during the temperature ramp measurements, none exhibit significant levels of catalytic conversion at low temperatures and reach around the same maximum catalytic conversion.

Table 6.2.4: Temperature dependency of the catalytic activity for 5Ru1Fe1Mn, 5Ru3Fe1Mn, and 5Ru1Fe3Mn presented as the slope of catalytic NO conversion $x_{NO,c}$ as a function of temperature in the ranges 350-400 ^{o}C and 375-425 ^{o}C.

Catalyst	**Temperature Dependency** (350-400 ^{o}C)	**Temperature Dependency** (375-425 ^{o}C)
5Ru1Fe1Mn	0.36	0.29
5Ru3Fe1Mn	0.12	0.20
5Ru1Fe3Mn	0.03	0.15

6.2.5 Comparison of all Ruthenium Catalysts

Figure 6.2.5 compares the temperature dependency of the catalytic NO conversion for all promoted Ru catalysts. The general trend is that the temperature dependency decreases with increased metal loading. The two catalysts with the highest metal loading (9 wt% total), 5Ru3Fe1Mn and 5Ru1Fe3Mn, show a significantly lower dependency on temperature, especially in the lower temperature range of 350-400 ^{o}C. The temperature dependency of catalytic conversion also generally decreases with increased loading of Mn, as it decreases in the orders of 5Ru1Fe > 5Ru1Mn and 5Ru1Fe1Mn > 5Ru3Fe1Mn > 5Ru1Fe3Mn. The chosen temperature ranges are both ranges where the catalytic conversion increases for all catalysts, meaning that lower dependency on temperature for a catalyst indicates that it can perform better at low-temperature NO oxidation in resembling nitric acid production conditions. The overall trend is that a decrease in total metal loading and an increase in Mn content lowers the temperature dependency of the catalytic conversion. Table 6.2.5 shows the onset temperature of catalytic activity, which was defined as the temperature where catalytic conversion surpasses 5%, and indicates a similar trend.

Figure 6.2.6 compares the estimated catalytic reaction rates of all promoted Ru catalysts at 375 ^{o}C and 425 ^{o}C. The bimetallic catalysts have the highest reaction rates at both temperatures, and there is a trend of decreased catalytic reaction rate with increased metal loading, similar to the trend of increased temperature

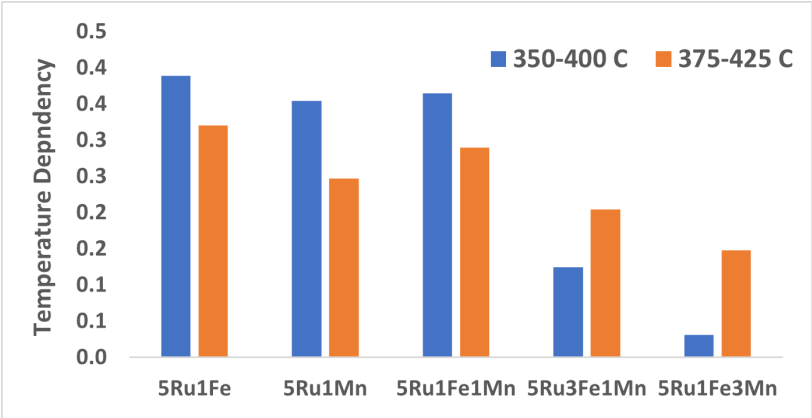

Figure 6.2.5: Temperature dependency of the catalytic activity for all promoted Ru catalysts presented as the slope of catalytic NO conversion $x_{NO,c}$ as a function of temperature in the ranges 350-400 ^{o}C and 375-425 ^{o}C.

Table 6.2.5: Temperature where catalytic conversion surpasses 5% for all promoted Ru catalysts.

Catalyst	**T_5%** [^{o}C]
5Ru1Fe	365
5Ru1Mn	346
5Ru1Fe1Mn	367
5Ru3Fe1Mn	382
5Ru1Fe3Mn	357

dependency. The results from these activity measurements and calculations indicate that increasing the metal loading, both in terms of the number of promoters and wt%, causes a decrease in catalyst performance. While the differences in performance are moderate, 5Ru1Mn exhibits the highest catalytic activity in the lower and higher temperature regimes, and the promotion of Ru with Mn appears to have a more positive impact on catalytic performance compared to Fe.

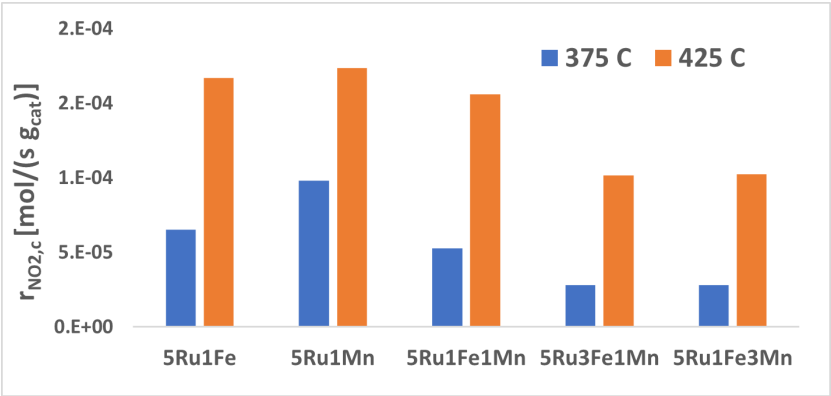

Figure 6.2.6: Calculated catalytic reaction rate for all supported Ru catalysts at 375 ^{o}C and 425 ^{o}C.

6.2.5.1 Comparison with un-promoted Ruthenium Catalyst

This work is a continuation of the work done in the course TKP4580 - *Chemical Engineering, Specialization Project* in the fall of 2022, where 1 wt% Pt/Al_{O3}, a 1 wt% Ru/Al_{O3}, and a 5 wt% Ru/Al_{O3} catalysts were synthesized, characterized and tested for activity towards NO oxidation in conditions resembling industrial nitric acid production. The 5 wt% Ru/Al_2O_3 (5Ru) catalyst displayed the highest catalytic activity, and the aim of this work was to improve this catalyst through promotion with other active metals. It is therefore relevant to compare the catalysts presented in this work to the 5Ru catalyst to assess how effective the promoters are in increasing the catalytic conversion of NO. Figure 6.2.7 presents the catalytic conversion of 5Ru and 5Ru1Mn as a comparison of the best-performing promoted catalyst to the non-promoted one. It is clear that 5Ru exhibits higher catalytic conversion, both in terms of lower onset temperature and higher maximum conversion, indicating that the promotion of Ru with Mn and Fe did not increase catalytic activity.

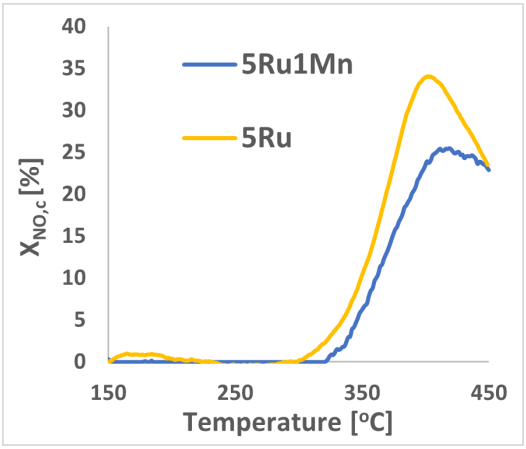

Figure 6.2.7: Catalytic NO conversion, $x_{NO,c}$ (%), of 5Ru and 5Ru1Mn in 10% NO, 6% O_2, 15% H_2O from 150-450 °C with a ramp rate of 5 °C/min, pressure of 1 bar, and WHSV = 24 000 NmL/h · g_{cat}.

Figure 6.2.8 presents a summary of the maximum catalytic conversion of each catalyst, including 5Ru, plotted against the temperature at which the respective maximum catalytic conversion occurs. The arrow indicates the direction of higher maximum catalytic conversion at lower temperatures, which are the desired characteristics of the catalyst presented in this work. While this plot should not be evaluated as a measure of the absolute best catalytic performance, it serves as a summary and basis for comparison of catalyst performance for NO oxidation. It illustrates the significant difference in catalytic activity between the un-promoted 5Ru catalyst and the promoted Ru catalysts synthesized and tested in this work. The thermodynamic equilibrium between NO and NO_2 (presented in Section 2.2.1) shifts towards NO with decreasing temperature, meaning that low-temperature catalytic activity is necessary in order to reach high levels of conversion. The conversion plot of 5Ru reaches the equilibrium curve at almost 20 °C lower than 5Ru1Mn (the lowest of the promoted catalysts). As seen in Figure 6.2.8, this results in a maximum catalytic conversion that is almost 10% higher than that of

5Ru1Mn (the highest of the promoted catalysts). Based on the results from activity measurements, it is clear that promoting Ru/Al_2O_3 catalysts with Fe and Mn through impregnation does not increase catalytic activity towards the oxidation of NO in simulated industrial nitric acid production conditions.

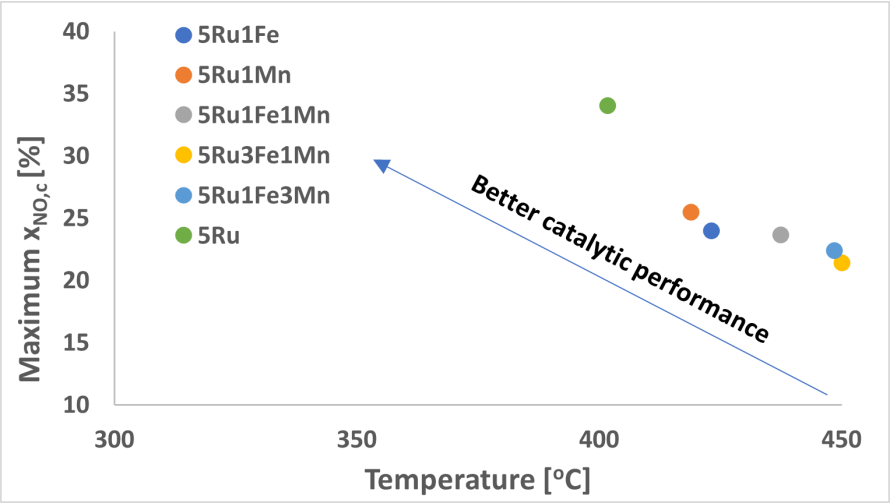

Figure 6.2.8: Maximum catalytic conversion versus temperature for all promoted Ru catalysts and 5Ru.

6.2.6 Steady State Conditions

The NO conversion of 5Ru1Fe3Mn was measured in a 48-hour-long isothermal activity test in 10% NO, 6% O_2, 15% H_2O at 360 ^{o}C, pressure of 1 bar, and WHSV = 24 000 NmL/h $\cdot$ g_{cat}. The test was conducted in order to evaluate the long-term catalytic activity of the 5Ru1Fe3Mn, to see if the addition of several promoters affected the stability of the trimetallic catalyst. Figure 6.2.9 presents the total NO conversion as a function of time of the 48-hour isothermal test, and Table 6.2.6 shows the average total NO conversion across the five 10-hour (one 8-hour) intervals.

Table 6.2.6: Average total conversion of NO across five time periods across 48 hours for 5Ru1Fe3Mn in 10% NO, 6% O_2, 15% H_2O at 360 ^{o}C, pressure of 1 bar, and WHSV = 24 000 NmL/h $\cdot$ g_{cat} $\cdot$

Time period (h)	Average total NO conversion (%)
0-10	15.2
0-20	16.8
20-30	17.9
30-40	17.8
40-48	17.9

The results from the isothermal test show that the NO conversion of 5Ru1Fe3Mn does not decrease at all across the extended period of 48 hours. In fact, the conversion slightly increases during the first 10 hours, before stabilizing around 17.9%. Gopakumar *et al.* tested a 0.5 wt% Ru/Al_2O_3 for long-term isothermal

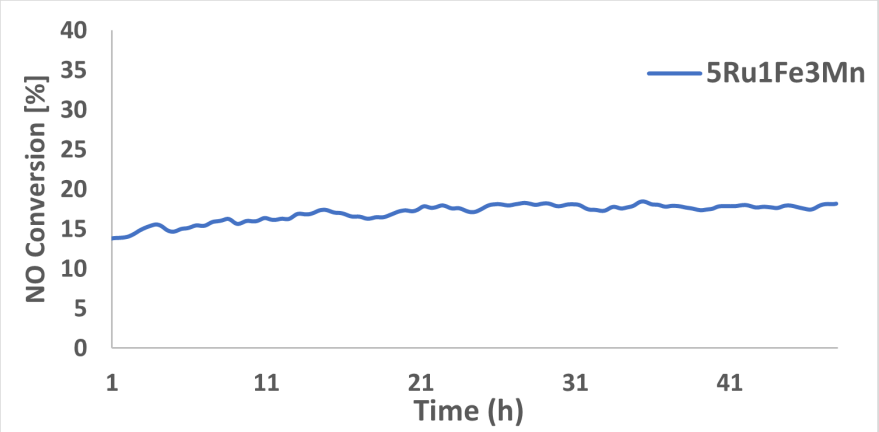

Figure 6.2.9: Total conversion of NO at 360 ^{o}C across 48 hours for 5Ru1Fe3Mn in n 10% NO, 6% O_2, 15% H_2O at 360 ^{o}C, pressure of 1 bar, and WHSV = 24 000 $\mathrm{NmL/h \cdot g_{cat}}$.

NO oxidation under similar conditions, and reported a similar trend of increase in conversion in the first 8 hours. It is not safe to conclude that there is an activation mechanism taking place, as the conversion increase could be due to pressure build-up, or the reaction taking a long time to reach steady state. However, the absolute absence of any loss of conversion across the entire time period indicates that the 5Ru1Fe3Mn is very stable for NO oxidation in conditions resembling industrial nitric acid production. Alumina-supported catalysts often exhibit high degrees of stability due to the chemical inertness and thermal stability of γ-Al_2O_3 [31]. In addition, γ-Al_2O_3-supported catalysts have shown good stability during NO oxidation reactions specifically. Grande *et al.* [17] studied NO oxidation at conditions relevant to nitric acid production (1-5% NO) over alumina-supported catalysts, observing no deactivation after 20 days on stream.

The active metals deposited on the alumina support can however deactivate over time due to mechanisms like changes in phase composition due to oxidation or reduction, or sintering. The increased loading of active metals on the trimetallic catalysts could increase the likelihood of sintering esepcially[69], making a long-term activity test necessary to confirm the stability of the promoted Ru catalysts. The absence of any signs of deactivation over a 48-hour long activity test indicates that promoting Ru/Al_2O_3 catalysts with several active metals is possible without compromising stability.

6.3 Characterization of spent catalyst

In this section, the characterization results of catalysts spent in activity testing are presented. After activity testing, the reactor contents were emptied, and the catalyst mixture was sieved in order to separate the catalyst and the SiC. Quartz wool above and below the catalyst bed held it in place inside the reactor, and the bulk of this was separated from the catalyst mixture with tweezers prior to sieving. Some of the quartz wool particles did however most likely end up in the spent catalyst mixtures used for characterization. The experimental setup of

characterization of fresh and spent catalysts was identical to ensure a consistent basis of comparison. Catalyst samples spent in the 10% NO temperature ramp from 150-450 ^{o}C are denoted with "SP NO", while the catalyst sample spent in the 48-hour isothermal run at 360 ^{o}C is denoted with "SP 360SS".

6.3.1 XRD

The XRD patterns of spent γ-Al_2O_3, 1Fe, and 1Mn can be found in Figures B.7 and B.8 in Appendix 7.2. The diffraction patterns of the spent samples did not differ from those of the fresh samples. This was expected as γ-Al_2O_3 is known for being both chemically and thermally stable, and there were no visible Fe or Mn peaks on the catalysts. One possible outcome of testing was that either Fe or Mn experienced enough agglomeration or sintering to where the crystallites would be large enough to show up on XRD patterns, however, this did not seem to be the case.

Figures 6.3.1, 6.3.2, 6.3.3, 6.3.4, and 6.3.5 show the XRD patterns of fresh and spent 5Ru1Fe, 5Ru1Mn, 5Ru1Fe1Mn, 5Ru3Fe1Mn, and 5Ru1Fe3Mn, respectively. The shape, position, and intensities of the peaks of the fresh and spent catalysts are effectively identical, indicating that there was no significant amount of change in dispersion, crystallite size, or phase composition during the 10% NO temperature ramp tests. This indicates that the catalysts are resistant to changes in phase composition and crystallite size and dispersion, which is a desirable trait for stable heterogeneous catalysts. The 5Ru1Fe3Mn sample spent in 10% NO at 360 ^{o}C for 48 hours, did, however, see some decrease in Ru peak sharpness and intensity. This implies a decrease in crystallinity and crystallite size, a somewhat unexpected effect compared with how the active metal on many catalysts tends to sinter or agglomerate over extended periods of activity testing [69, 85]. While this effect could be due to loss of active metal and not redispersion, this is unlikely as the temperatures used should not be high enough for the evaporation of Ru to take place.

The industrial nitric acid production feed conditions of 10% NO, 6% O_2, and 15% H_2O are strongly oxidizing conditions, which have proven problematic for other promising catalysts. Pt is an active metal that has proven very effective in NO oxidation in diesel exhaust conditions, where the concentrations of NO are low (0.1-1%). Under stronger oxidizing conditions, however, Pt catalysts tend to experience deactivation over time due to the oxidation of Pt to PtO [103]. The fact that oxidation is not evident on the promoted Ru/Al_2O_3 catalysts, even after 48 hours of testing, indicates that the catalyst is stable for NO oxidation in simulated nitric acid production conditions.

The average crystallite size of Ru was investigated both before and after activity testing. The same method was used for both spent and fresh catalysts. The peak used for calculations was the (101) peak at $2\vartheta = 44^{o}$, with $\lambda = 1.5405$ Å. The shape factor used was 0.9 assuming spherical particles, and Equation 4.4 described in Section 4.2.1 was used to calculate dispersion for internal comparison, with k = 1. The results are summarized in Table 6.3.1, and a comparison of the average Ru

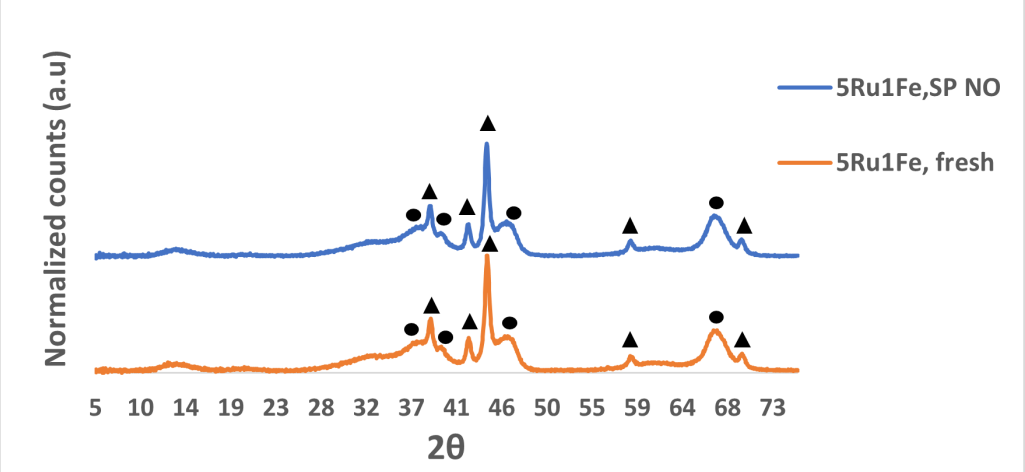

Figure 6.3.1: XRD patterns of fresh and spent 5Ru1Fe.The distinct γ-Al_2O_3 peaks are indicated with a dot (•), while the Ru^0 peaks are indicated with a triangle (▲).

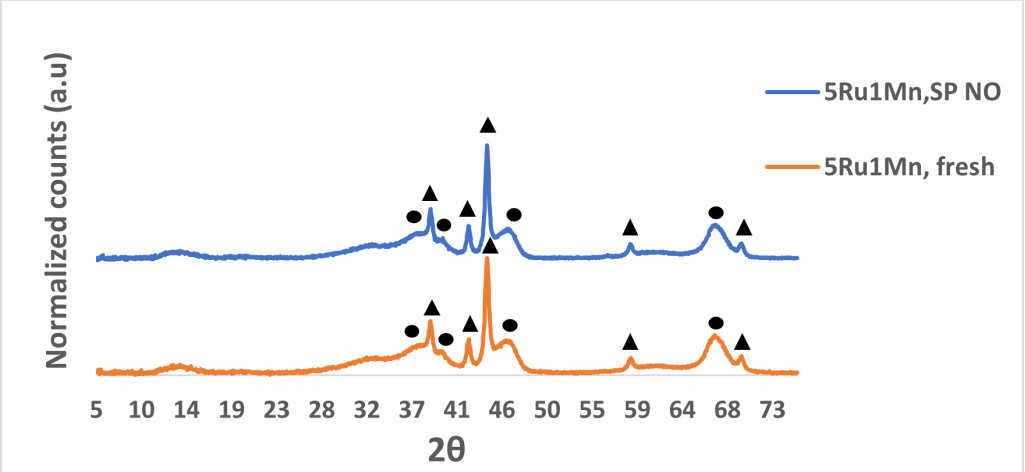

Figure 6.3.2: XRD patterns of fresh and spent 5Ru1Mn.The distinct γ-Al_2O_3 peaks are indicated with a dot (•), while the Ru^0 peaks are indicated with a triangle (▲).

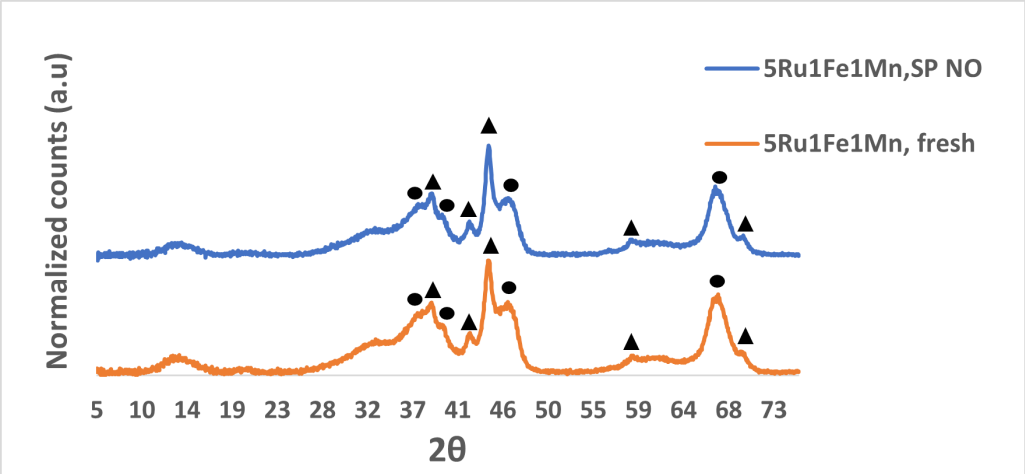

Figure 6.3.3: XRD patterns of fresh and spent 5Ru1Fe1Mn.The distinct γ-Al_2O_3 peaks are indicated with a dot (•), while the Ru^0 peaks are indicated with a triangle (▲).

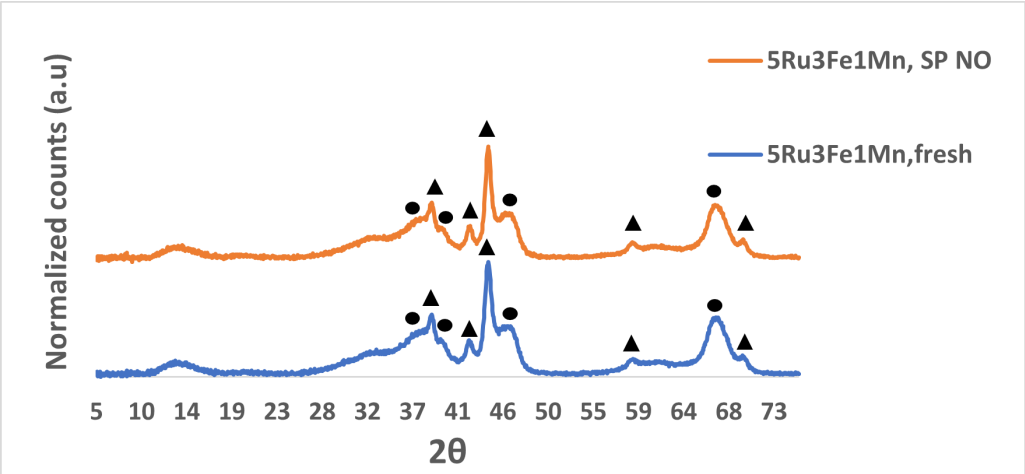

Figure 6.3.4: XRD patterns of fresh and spent 5Ru3Fe1Mn.The distinct γ-Al_2O_3 peaks are indicated with a dot (•), while the Ru^0 peaks are indicated with a triangle (▲).

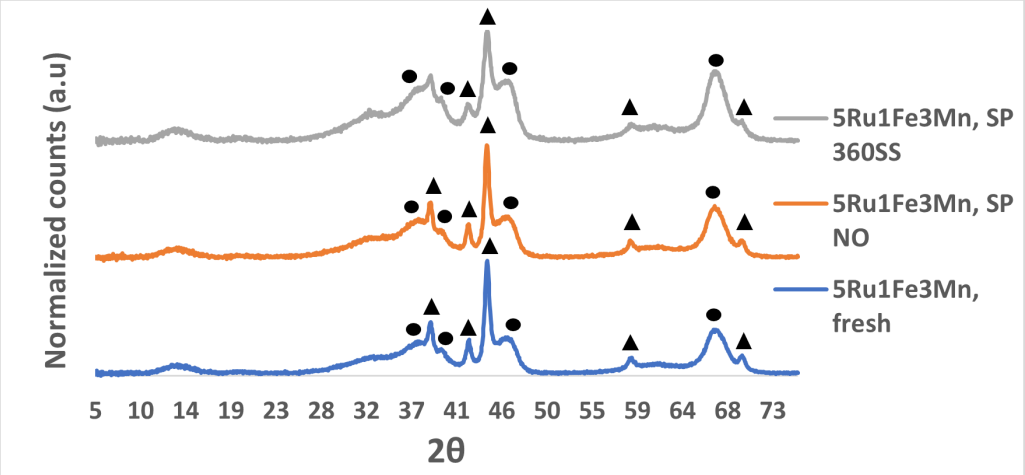

Figure 6.3.5: XRD patterns of fresh and spent 5Ru1Fe3Mn.The distinct γ-Al_2O_3 peaks are indicated with a dot (•), while the Ru^0 peaks are indicated with a triangle (▲).

crystallite size of the fresh and spent catalysts is visualized in Figure 6.3.6.

Table 6.3.1: Crystallite size and dispersion of Ru on spent catalysts calculated using the Scherrer equation (Equation 4.2).

Catalyst	Crystallite Size [nm]	Dispersion [%]
5Ru1Fe, SP NO	18	6 %
5Ru1Mn, SP NO	22	5 %
5Ru1Fe1Mn, SP NO	12	8 %
5Ru3Fe1Mn, SP NO	14	7 %
5Ru1Fe3Mn, SP NO	17	6 %
5Ru1Fe3Mn, SP 360SS	12	8 %

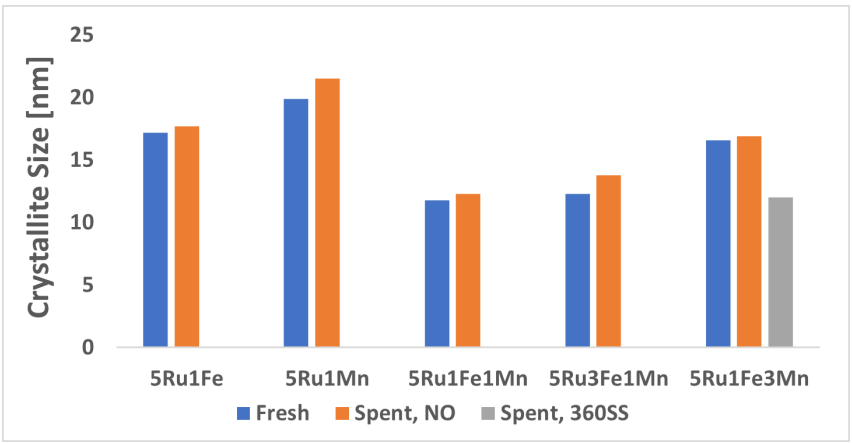

Figure 6.3.6: Average Ru crystallite sizes on fresh and spent catalysts calculated using the Scherrer equation (Equation 4.2).

The crystallite sizes lay within the range of 12-22 nm, which is similar to that of the fresh catalysts. Figure 6.3.6 shows a slight trend in increasing crystallite size

after the catalyst is spent in activity measurements, however, the change is too small to indicate a clear trend of crystallite growth. In fact, the sample which underwent testing for 48 hours and in theory should be most prone to an increase in crystallite size, showed a decrease of 5 nm. It is therefore not possible to conclude that there was significant redispersion of metal particles during activity testing, based on these results.

6.3.2 Chemisorption

The dispersion and crystallite size of Ru was measured by CO chemisorption on catalysts before and after activity testing. The experimental challenges regarding these measurements are explained in detail in Section 6.1.3. Table 6.3.2 shows the dispersion and crystallite size of Ru on the spent catalysts. A comparison of the dispersion and crystallite size of Ru in the fresh and spent catalysts is visualized in Figure 6.3.7 and Figure 6.3.8, respectively. The results show a slight trend of an increase in dispersion and a decrease in crystallite size after activity testing.

Table 6.3.2: Dispersion and crystallite size of Ru on spent catalysts measured by CO chemisorption.

Catalyst	Dispersion [%]	Crystallite Size [nm]
5Ru1Fe, SP NO	9	14
5Ru1Mn, SP NO	8	17
5Ru1Fe1Mn, SP NO	13	10
5Ru3Fe1Mn, SP NO	8	15
5Ru1Fe3Mn, SP NO	7	20
5Ru1Fe3Mn, SP 360SS	8	16

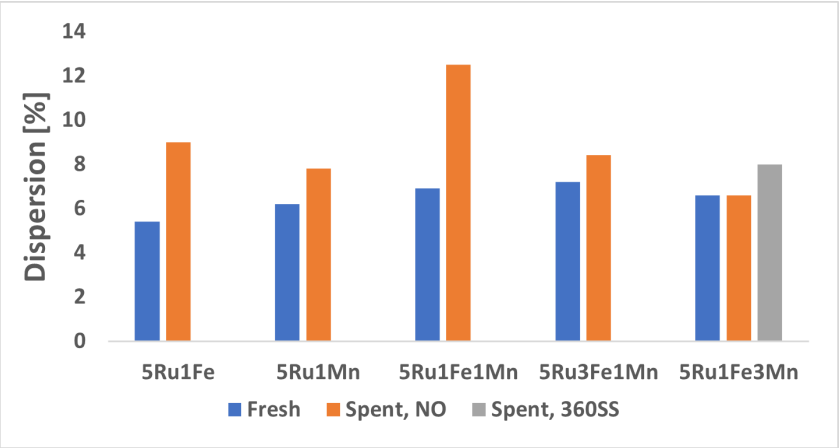

Figure 6.3.7: Dispersion of active metal on fresh and spent catalyst measured by CO chemisorption.

When comparing the results of crystallite size and dispersion of fresh versus spent catalysts calculated by XRD and CO chemisorption, the slight trends that the two methods indicate contradict one another. The chemisorption results indicate an increase in particle size for most catalysts, while XRD suggests a slight decrease. It

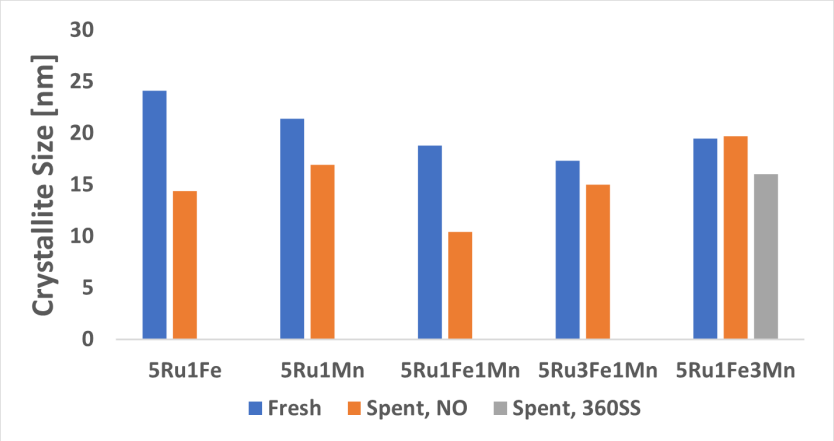

Figure 6.3.8: Crystallite sizes of fresh and spent catalyst measured by CO chemisorption.

is therefore not possible to conclude that there is a clear trend change in crystallite size and dispersion of Ru in the catalysts which have undergone activity testing for NO oxidation. The fact that the sample spent in long-term isotherm testing exhibits an opposite trend from the rest of the results from CO chemisorption, and also shows minimal change, strengthens the claim of the absence of significant redispersion during the reaction.

CHAPTER

SEVEN

CONCLUSIONS AND FUTURE WORK

7.1 Conclusion

Seven alumina-supported catalysts were synthesized, characterized, and tested for catalytic activity for oxidation of NO to NO_2 for industrial nitric acid production. Five catalysts were 5 wt% Ru promoted with varying amounts of Fe and Mn, in addition to a 1 wt% Fe and a 1 wt% Mn catalyst. All catalysts were prepared by wet impregnation, and catalysts containing Ru were calcined in a reducing atmosphere, the others in air. The catalysts were characterized by X-ray diffraction, N_2 adsorption, and CO chemisorption, confirming the presence of high surface area γ-Al_2O_3 and metallic Ru. The dispersion of active metal did not significantly differ with changing composition. All catalysts were tested for oxidation of NO to NO_2 in a feed composition of 10% NO, 6% O_2, and 15% H_2O at 1 bar pressure, simulating industrial nitric acid production conditions. One catalyst was also tested for stability in an isothermal run at 360 ^{o}C for 48 hours. All spent catalysts were characterized to gauge the effect of the reaction on catalyst properties.

Results from activity testing showed moderate differences in catalytic activity between the promoted Ru catalysts. The conversion of NO appeared to decrease slightly with higher metal loading and increased Fe content. The temperature dependency of the catalytic conversion decreased with increased metal loading and higher Mn content. Increased amounts of Mn also improved low-temperature conversion, and the catalyst which displayed the highest conversion both overall and at lower temperatures was 5Ru1Mn (5 wt% Ru, 1 wt% Mn). The 48-hour-long isothermal test of 5Ru1Fe3Mn showed a slight increase in NO conversion across the first 20 hours and no decrease after that point, indicating high stability of the trimetallic catalysts.

This work is a continuation of the work done in the course TKP4580 - *Chemical Engineering, Specialization Project* in the fall of 2022 where a 5 wt% Ru/Al_2O_3 catalyst displayed promising catalytic performance. The aim of promoting Ru with Fe and Mn was to increase the catalytic activity of the catalyst. However, all promoted catalysts presented in this work displayed significantly lower catalytic conversion at all temperatures.

While the promotion of Ru/Al_2O_3 with Fe and Mn decreased catalytic activity, it did not negatively impact other catalyst properties. Surface area, crystallite size, and dispersion remained stable upon promotion and activity testing. All catalysts exhibited a slight increase in dispersion after being tested in 10% NO, including the sample from the long-term isothermal test. There was also no detectable change in the phase composition of alumina or Ru during testing. These characterization results indicate that the promoted catalyst is still resistant to deactivation mechanisms like sintering, agglomeration, and oxidation of metallic Ru. This shows that the promotion of Ru with significant amounts of other metals is possible without compromising key catalyst properties, although Fe and Mn did not improve catalytic activity.

7.2 Future Work

Promotion of Ru with Mn and Fe proved to decrease catalytic activity but retain other key catalyst features. It is therefore suggested that other metals are tested as promoters for Ru in the catalytic oxidation of NO under simulated industrial nitric acid production conditions. Silver seems to be a good alternative, as both Gopakumar *et al.* [19] and Vold [104] both reported that the promotion of manganese oxides with silver significantly improved catalytic activity for NO oxidation under conditions resembling industrial nitric acid production. Platinum is another promising option, as it has proven to be catalytically active for NO oxidation in several studies, although issues with stability have been reported [13, 17, 20, 104].

As demonstrated in this work, alumina is a very stable support that allows for high surface area and dispersion. It does, however, as displayed in catalytic activity tests, not exhibit any activity towards NO oxidation on its own, being completely inert. One possibility for future work could therefore be to investigate Ru catalysts on other supports. Manganese oxide and zirconia have exhibited catalytic activity in NO oxidation and could be intriguing options to explore as supports, although issues regarding stability have also been reported [19, 39, 104].

Characterization results like crystallite size and dispersion have many possible sources of inaccuracy, as discussed in previous sections. A possible additional characterization technique that could help improve the accuracy and understanding of these properties is transmission electron microscopy (TEM). The use of TEM can give accurate information on particle shape and particle size distribution and identify adsorbed species on the catalyst surface. Information like this can help improve the understanding of key catalyst properties and adsorption mechanisms, which could also be a possible deactivation mechanism (poisoning).
As discussed in Section 5.3, there are many challenges regarding the experimental design which lead to uncertainties regarding temperature control, pressure drop, and gradients in temperature and pressure. Many modifications to the experimental setup, like adding more thermocouples or using quartz or glass reactors, tend to cause more new problems than they solve. One modification, however, that can be done without much interference with the process is the recording of the measured temperature and pressures in the system. The LabView software

displays bed and heating block temperature, along with reactor pressure. If the software was developed to accurately record these values in time, it could help explain irregular activity during reactions, and give better understanding of how modifications to the experimental design affect temperature and pressure.

BIBLIOGRAPHY

[1] *End hunger, achieve food security and improved nutrition and promote sustainable agriculture*. 2015. URL: https://sdgs.un.org/goals/goal2.

[2] Janet Ranganathan et al. *How to Sustainably Feed 10 Billion People by 2050, in 21 Charts*. Tech. rep. World Resources Institute, Dec. 2018. URL: https://www.wri.org/insights/how-sustainably-feed-10-billion-people-2050-21-charts.

[3] *FAO. 2018. Transforming Food and Agriculture to Achieve the SDGs: 20 interconnected actions to guide decision-makers. Technical Reference Document. Rome. 132 pp. Licence: CC BY-NC-SA 3.0 IGO.*

[4] *World population projected to reach 9.8 billion in 2050, and 11.2 billion in 2100*. 2017. URL: https://www.un.org/en/desa/world-population-projected-reach-98-billion-2050-and-112-billion-2100#:~:text=The%20current%20world%20population%20of,Nations%20report%20being%20launched%20today..

[5] Jonathan A Foley et al. "Global Consequences of Land Use". In: *American Association for the Advancement of Science* 22.5734 (2005), pp. 570–574. URL: https://www.jstor.org/stable/3842335.

[6] *Why is fertilizer important for feeding the world?* 2023. URL: https://www.yara.com/crop-nutrition/crop-and-agronomy-knowledge/why-is-fertilizer-important/.

[7] *Crop nutrition: Our fertilizer product range*. 2023. URL: https://www.yara.com/crop-nutrition/our-fertilizer-product-range/.

[8] *AP42 8.8 Nitric Acid Production*. Tech. rep. United States Environmental Protection Agency, 1993.

[9] *Nitric Acid Market Size & Share Analysis - Industry Research Report - Growth Trends*. Tech. rep. Mordor Intelligence, 2017. URL: https://www.mordorintelligence.com/industry-reports/nitric-acid-market.

[10] Chongyan Ruan et al. "Selective catalytic oxidation of ammonia to nitric oxide via chemical looping". In: *Nature Communications* (2022). DOI: 10.1038/s41467-022-28370-0. URL: https://doi.org/10.1038/s41467-022-28370-0.

[11] Jacob A Moulijn, Michiel Makkee, and Annelies E. van Diepen. *Chemical process technology*. 04. Dec. 2013, pp. 260–263. ISBN: 9781444320244. DOI: 10.5860/CHOICE.51-2107. URL: http://choicereviews.org/review/10.5860/CHOICE.51-2107.

[12] R Gubler et al. *Nitric Acid: Chemical Economics Handbook*. London: IHS Chemical, 2014.

[13] Ata ul Rauf Salman. "Catalytic oxidation of NO to NO2 for nitric acid production". PhD thesis. Norwegian University of Science and Technology, 2019.

[14] William C. Klingelhoefer. *Nitric Oxide Oxidation*. 1938.

[15] M.L. Heilig. *Process of Oxidizing Gases*. 1994.

[16] H.C Andersen and A.J. Haley. *Process for the oxidation of nitric oxide*. 1963.

[17] Carlos A Grande et al. "Process Intensification in Nitric Acid Plants by Catalytic Oxidation of Nitric Oxide". In: (2018). DOI: 10.1021/acs.iecr.8b01483. URL: https://pubs.acs.org/sharingguidelines.

[18] Jithin Gopakumar et al. "Oxidation of NO using a supported Ru catalyst at nitric acid production conditions[Manuscript in preparation]". In: (2023).

[19] Jithin Gopakumar et al. "Catalytic oxidation of NO to NO 2 for industrial nitric acid production using Ag-promoted MnO 2 / ZrO 2 catalysts †". In: (2023). DOI: 10.1039/d2cy02178a. URL: https://doi.org/.

[20] Ata ul Rauf Salman et al. "Catalytic oxidation of NO to NO2 for nitric acid production over a Pt/Al2O3 catalyst". In: *Applied Catalysis A: General* 564 (Aug. 2018), pp. 142–146. ISSN: 0926-860X. DOI: 10.1016/J.APCATA.2018.07.019.

[21] Samir S. Amr and Abdelghani Tbakhi. "Jabir ibn Hayyan". In: *Annals of Saudi Medicine* 27.1 (2007).

[22] *Chile saltpetre*. 2008. URL: https://www.britannica.com/science/Chile-saltpetre.

[23] Michael Thiemann, Erich Scheibler, and Karl Wilhelm Wiegand. *Nitric Acid, Nitrous Acid, and Nitrogen Oxides*. Weinheim, Germany: Wiley-VCH Verlag GmbH & Co. KGaA, June 2000. DOI: 10.1002/14356007.a17{_}293. URL: https://onlinelibrary.wiley.com/doi/10.1002/14356007.a17_293.

[24] Kevin H R Rouwenhorst et al. "From the Birkeland-Eyde process towards energy-efficient plasma-based NO X synthesis: a techno-economic analysis". In: *This journal is Cite this: Energy Environ. Sci* 14 (2021), p. 2520. DOI: 10.1039/d0ee03763j.

[25] Hannah Ritchie. *How many people does synthetic fertilizer feed?* Nov. 2017. URL: https://ourworldindata.org/how-many-people-does-synthetic-fertilizer-feed#:~:text=As%20a%20result%2C%20the%20Haber,to%203.5%20billion%20people%20today..

[26] S. C. Gad. "Nitrous Oxide". In: *Encyclopedia of Toxicology: Third Edition* (Jan. 2014), pp. 586–587. DOI: 10.1016/B978-0-12-386454-3.00893-9.

[27] Xin Liu, Yongqiang Han, and Husheng Jia. "Pt-Rh-Pd Alloy Group Gauze Catalysts Used for Ammonia Oxidation". In: *Rare Metal Materials and Engineering* 46.2 (Feb. 2017), pp. 339–343. ISSN: 1875-5372. DOI: 10.1016/S1875-5372(17)30091-7.

[28] György D. Honti. *The nitrogen industry*. Akadémiai Kiadó, 1976, pp. 400–413. ISBN: 963-05-0228-3. URL: http://opac.mtak.hu/F?func=direct&local_base=MTA01&doc_number=523415.

[29] Guido Busca. "Structural, Surface, and Catalytic Properties of Aluminas". In: (). DOI: 10.1016/B978-0-12-800127-1.00003-5. URL: http://dx.doi.org/10.1016/B978-0-12-800127-1.00003-5.

[30] J. W. Niemantsverdriet I. Chorkendorff. *Concepts of Modern Catalysis and Kinetics, 3rd Edition*. 3rd. Vol. 1. John Wiley & Sons, 2017.

[31] Monica Trueba and Stefano P. Trasatti. "γ-alumina as a support for catalysts: A review of fundamental aspects". In: *European Journal of Inorganic Chemistry* 17 (Sept. 2005), pp. 3393–3403. ISSN: 14341948. DOI: 10.1002/EJIC.200500348.

[32] Yadian Xie et al. *The Effect of Novel Synthetic Methods and Parameters Control on Morphology of Nano-alumina Particles*. Dec. 2016. DOI: 10.1186/s11671-016-1472-z.

[33] Denghui Wang et al. "Assisting effect of Al2O3 on MnOx for NO catalytic oxidation". In: *Green Energy & Environment* 6.6 (Dec. 2021), pp. 903–909. ISSN: 2468-0257. DOI: 10.1016/J.GEE.2020.07.005.

[34] Mario Pagliaro, Sandro Campestrini, and Rosaria Ciriminna. "Ru-based oxidation catalysis". In: *Chemical Society Reviews* 34.10 (2005), pp. 837–845. ISSN: 14604744. DOI: 10.1039/b507094p.

[35] Landong Li et al. "Oxidation of nitric oxide to nitrogen dioxide over Ru catalysts". In: *Applied Catalysis B: Environmental* 88.1-2 (Apr. 2009), pp. 224–231. ISSN: 09263373. DOI: 10.1016/j.apcatb.2008.09.032.

[36] Kazuo Urabe, Takashi Yoshioka, and Atsumu Ozaki. "Ammonia synthesis activity of a Raney ruthenium catalyst". In: *Journal of Catalysis* 54.1 (Aug. 1978), pp. 52–56. ISSN: 0021-9517. DOI: 10.1016/0021-9517(78)90026-X.

[37] L. A. Sokolova, N. M. Popova, and K. Dosumov. "Mechanism of NO adsorption and decomposition on ruthenium catalysts". In: *Reaction Kinetics and Catalysis Letters* 26.1-2 (1984), pp. 193–197. ISSN: 15882837. DOI: 10.1007/BF02063890.

[38] I Characterization. "Support and Promoter Effect of Ruthenium Catalyst". In: 304 (1985), pp. 296–304.

[39] Hu Chen, Ying Wang, and Yong-Kang Lv. "Catalytic oxidation of NO over MnO 2 with different crystal structures †". In: *Royal Society of Chemistry* (2016). DOI: 10.1039/c6ra10103h. URL: www.rsc.org/advances.

[40] G.K Boreskov. *Catalysis: Catalytic Activation of Dioxygen*. Ed. by John R. Anderson and Michel Boudart. Vol. 3. Berlin, Heidelberg: Springer Berlin Heidelberg, 1982, pp. 39–137. ISBN: 978-3-642-93225-0. DOI: 10.1007/978-3-642-93223-6. URL: http://link.springer.com/10.1007/978-3-642-93223-6.

[41] Sanjiang Pan et al. "Efficient and stable noble-metal-free catalyst for acidic water oxidation". In: (). DOI: 10.1038/s41467-022-30064-6. URL: https://doi.org/10.1038/s41467-022-30064-6.

[42] Elena Brusamarello et al. "Manganese Based Perovskites in Soot Oxidation: Far from Noble Metals?" In: 1 (), p. 3. DOI: 10.1007/s11244-022-01726-y. URL: https://doi.org/10.1007/s11244-022-01726-y.

[43] F. Arena et al. "Structure and redox properties of bulk and supported manganese oxide catalysts". In: *Physical Chemistry Chemical Physics* 3.10 (2001), pp. 1911–1917. ISSN: 14639076. DOI: 10.1039/B100091H.

[44] Brian R Strohmeier and David M Hercules. "Surface Spectroscopic Characterization of Mn/Al203 Catalysts". In: *J. Phys. Chem* 88 (1984), pp. 4922–4929. URL: https://pubs.acs.org/sharingguidelines.

[45] L.A Corathers and J.F Machamer. "Manganese". In: *Industrial Minerals & Rocks: Commodities, Markets, and Uses*. Vol. 7. 2006, pp. 631–636. ISBN: 978-0-87335-233-8. URL: https://books.google.no/books?id=zNicdkuulE4C&pg=PA631&redir_esc=y#v=onepage&q&f=false.

[46] Nian Tang et al. "Mechanism study of NO catalytic oxidation over MnOx/-TiO 2 catalysts". In: *Journal of Physical Chemistry C* 115.16 (Apr. 2011), pp. 8214–8220. ISSN: 19327447. DOI: 10.1021/JP200920Z.

[47] V. P. Santos et al. "The role of lattice oxygen on the activity of manganese oxides towards the oxidation of volatile organic compounds". In: *Applied Catalysis B: Environmental* 99.1-2 (Aug. 2010), pp. 353–363. ISSN: 09263373. DOI: 10.1016/J.APCATB.2010.07.007.

[48] Freek Kapteijn et al. "Alumina-Supported Manganese Oxide Catalysts - I Characterization - Effect of Precursor and Loading". In: *Journal of Catalysis* 150 (1994), pp. 94–104.

[49] Hui Wang et al. "Performance and mechanism comparison of manganese oxides at different valence states for catalytic oxidation of NO". In: *Chemical Engineering Journal* 361 (Apr. 2019), pp. 1161–1172. ISSN: 1385-8947. DOI: 10.1016/J.CEJ.2018.12.159.

[50] Shuhui Liang et al. "Effect of Phase Structure of MnO 2 Nanorod Catalyst on the Activity for CO Oxidation". In: (2008). DOI: 10.1021/jp0774995. URL: https://pubs.acs.org/sharingguidelines.

[51] *Iron - Oxidation States, Ferrous Oxide, Ferric Sulfate, and Ferric Chloride | Britannica*. URL: https://www.britannica.com/science/iron-chemical-element/Compounds.

[52] Fatima I Adam et al. "Redox Properties and Activity of IronCitrate Complexes: Evidence for Redox Cycling". In: (2015). DOI: 10.1021/tx500377b. URL: https://pubs.acs.org/sharingguidelines.

[53] Arif Darmawan et al. "Integrated ammonia production from the empty fruit bunch". In: *Innovative Energy Conversion from Biomass Waste* (Jan. 2022), pp. 149–185. DOI: 10.1016/B978-0-323-85477-1.00006-3.

[54] V Palma et al. "Catalysts for conversion of synthesis gas". In: (2017). DOI: 10.1016/B978-0-08-101031-0.00007-7. URL: http://dx.doi.org/10.1016/B978-0-08-101031-0.00007-7.

[55] Dong Hyun Chun et al. "Highly selective iron-based Fischer-Tropsch catalysts activated by CO 2-containing syngas". In: (2014). DOI: 10.1016/j.jcat.2014.06.014. URL: http://dx.doi.org/10.1016/j.jcat.2014.06.014.

[56] Kamyar Keyvanloo et al. "Supported Iron FischerTropsch Catalyst: Superior Activity and Stability Using a Thermally Stable Silica-Doped Alumina Support". In: (2014). DOI: 10.1021/cs401242d. URL: https://pubs.acs.org/sharingguidelines.

[57] Bahareh A.T. Mehrabadi et al. "A Review of Preparation Methods for Supported Metal Catalysts". In: *Advances in Catalysis*. Vol. 61. Academic Press Inc., 2017, pp. 1–35. DOI: 10.1016/bs.acat.2017.10.001.

[58] Eric Marceau, Xavier Carrier, and Michel Che. *Synthesis of Solid Catalysts*. Wiley-VCH, Oct. 2009, pp. 59–78. ISBN: 9783527320400. DOI: 10.1002/9783527626854. URL: https://onlinelibrary.wiley.com/doi/book/10.1002/9783527626854.

[59] B. Rand. "Calcination". In: *Concise Encyclopedia of Advanced Ceramic Materials* (Jan. 1991), pp. 49–51. DOI: 10.1016/B978-0-08-034720-2.50023-X. URL: https://linkinghub.elsevier.com/retrieve/pii/B978008034720250023X.

[60] Samir Lamouri et al. "Control of the γ-alumina to α-alumina phase transformation for an optimized alumina densification". In: *Boletín de la Sociedad Española de Cerámica y Vidrio* 56.2 (Mar. 2017), pp. 47–54. ISSN: 0366-3175. DOI: 10.1016/J.BSECV.2016.10.001. URL: https://www.elsevier.es/en-revista-boletin-sociedad-espanola-ceramica-vidrio-26-articulo-control-alumina-alumina-phase-transformation-S0366317516300899.

[61] *X-ray diffraction | Definition, Diagram, Equation, & Facts | Britannica*. 2023. URL: https://www.britannica.com/science/X-ray-diffraction.

[62] Richard A Spragg. "IR Spectrometers A2 - Lindon, John C". In: *Encyclopedia of Spectroscopy and Spectrometry (Second Edition)* (2010), pp. 1199–1209. URL: http://www.sciencedirect.com:5070/referencework/9780123744135/encyclopedia-of-spectroscopy-and-spectrometry.

[63] J. Epp. "X-ray diffraction (XRD) techniques for materials characterization". In: *Materials Characterization Using Nondestructive Evaluation (NDE) Methods* (Jan. 2016), pp. 81–124. DOI: 10.1016/B978-0-08-100040-3.00004-3.

[64] Ahmad Monshi, Mohammad Reza Foroughi, and Mohammad Reza Monshi. "Modified Scherrer Equation to Estimate More Accurately Nano-Crystallite Size Using XRD". In: *World Journal of Nano Science and Engineering* 02.03 (2012), pp. 154–160. ISSN: 2161-4954. DOI: 10.4236/wjnse.2012.23020.

[65] B. Ingham and M. F. Toney. "X-ray diffraction for characterizing metallic films". In: *Metallic Films for Electronic, Optical and Magnetic Applications: Structure, Processing and Properties*. Elsevier Ltd., 2013, pp. 3–38. ISBN: 9780857090577. DOI: 10.1533/9780857096296.1.3.

[66] Adriana Valério and Sérgio L. Morelhão. "Usage of Scherrer's formula in X-ray diffraction analysis of size distribution in systems of monocrystalline nanoparticles". In: (Nov. 2019). URL: http://arxiv.org/abs/1911.00701.

[67] C.G. Zhou and Q.H. Yu. "Nanostructured thermal barrier coatings". In: *Thermal Barrier Coatings* (Jan. 2011), pp. 75–96. DOI: 10.1533/9780857090829.1.75.

[68] C Prado-Burguete et al. *Effect of Carbon Support and Mean Pt Particle Size on Hydrogen Chemisorption by Carbon-Supported Pt Catalysts*. Tech. rep. 1991, pp. 397–404.

[69] Deraz Nasrallah M. "Sintering process and catalysis". In: *International Journal of Nanomaterials, Nanotechnology and Nanomedicine* (Jan. 2018), pp. 001–003. DOI: 10.17352/2455-3492.000023.

[70] Soshi Shiraishi. *Electric Double Layer Capacitors*. Tech. rep. Gunma: Gunma University, 2003, pp. 447–456.

[71] Mahmoud Nasrollahzadeh et al. "Plant-Mediated Green Synthesis of Nanostructures: Mechanisms, Characterization, and Applications". In: *Interface Science and Technology* 28 (Jan. 2019), pp. 199–322. ISSN: 1573-4285. DOI: 10.1016/B978-0-12-813586-0.00006-7.

[72] Stephen Brunauer, P H Emmett, and Edward Teller. *Adsorption of Gases in Multimolecular Layers*. Tech. rep. 1938. URL: https://pubs.acs.org/sharingguidelines.

[73] Isah Mohammed et al. *A review on polymer, gas, surfactant and nanoparticle adsorption modeling in porous media*. 2020. DOI: 10.2516/ogst/2020063.

[74] Pieter Bertier et al. "On the use and abuse of N2 physisorption for the characterization of the pore structure of shales". In: Mar. 2016, pp. 151–161. DOI: 10.1346/cms-wls-21.12.

[75] Saied Azizian and Setareh Eris. "Adsorption isotherms and kinetics". In: *Interface Science and Technology* 33 (Jan. 2021), pp. 445–509. ISSN: 1573-4285. DOI: 10.1016/B978-0-12-818805-7.00011-4.

[76] Kenneth Sing. "Reporting physisorption data for gas/solid systems with special reference to the determination of surface area and porosity". In: *Pure and Applied Chemistry* 57.4 (1985), pp. 603–619. DOI: 10.1351/PAC198557040603.

[77] R. J. (Ruud J.) Wijngaarden, A. Kronberg, and K. R. Westerterp. *Industrial catalysis : optimizing catalysts and processes*. Wiley-VCH, 1998, p. 268. ISBN: 3527285814.

[78] Elliott P. Barrett, Leslie G. Joyner, and Paul P. Halenda. "The Determination of Pore Volume and Area Distributions in Porous Substances. I. Computations from Nitrogen Isotherms". In: *Journal of the American Chemical Society* 73.1 (May 2002), pp. 373–380. DOI: 10.1021/ja01145a126.

[79] M. N. Kajama. "Hydrogen permeation using nanostructured silica membranes". In: *Sustainable Development and Planning VII*. Vol. 1. WIT Press, May 2015, pp. 447–456. DOI: 10.2495/sdp150381.

[80] David Stephen. Ballantine. *Acoustic wave sensors : theory, design, and physico-chemical applications*. Academic Press, 1997, p. 436. ISBN: 0120774607.

[81] O. Abdulrahman Adeleke et al. "Principles and Mechanism of Adsorption for the Effective Treatment of Palm Oil Mill Effluent for Water Reuse". In: *Nanotechnology in Water and Wastewater Treatment: Theory and Applications* (Jan. 2019), pp. 1–33. DOI: 10.1016/B978-0-12-813902-8.00001-0.

[82] Soonchul Kwon et al. "CO2 Sorption". In: *Coal Gasification and Its Applications* (Jan. 2011), pp. 293–339. DOI: 10.1016/B978-0-8155-2049-8.10010-5.

[83] Paul A Webb. "Introduction to Chemical Adsorption Analytical Techniques and their Applications to Catalysis". Norcross, Georgia, 2003.

[84] Martin Schmal. *Heterogeneous Catalysis and its Industrial Applications*. Vol. 1. Springer International Publishing, 2016, pp. 27–62. DOI: 10.1007/978-3-319-09250-8.

[85] Stefano Cimino and Luciana Lisi. "Catalyst Deactivation, Poisoning and Regeneration". In: *Catalysts* 9 (2019), p. 668. DOI: 10.3390/catal9080668. URL: www.mdpi.com/journal/catalysts.

[86] Grard Bergeret and Pierre Gallezot. *Handbook of Heterogeneous Catalysis*. Vol. 1. John Wiley & Sons, Ltd, Mar. 2008, pp. 738–765. DOI: 10.1002/9783527610044.HETCAT0038. URL: https://onlinelibrary.wiley.com/doi/full/10.1002/9783527610044.hetcat0038%20https://onlinelibrary.wiley.com/doi/abs/10.1002/9783527610044.hetcat0038%20https://onlinelibrary.wiley.com/doi/10.1002/9783527610044.hetcat0038.

[87] Peter R. Griffiths and James A. De Haseth. *Fourier Transform Infrared Spectrometry: Second Edition*. wiley, June 2006, pp. 1–529. ISBN: 9780470106310. DOI: 10.1002/047010631X. URL: https://onlinelibrary.wiley.com/doi/book/10.1002/047010631X.

[88] "Introduction to Gas Phase FTIR Spectroscopy Introduction to FTIR Spectroscopy". In: *Thermo Fischer Scientific* (2022).

[89] E G Eddings et al. "MINIMIZATION OF NO EMISSIONS FROM MULTI-BURNER COAL-FIRED BOILERS". In: (Apr. 2000). DOI: 10.2172/786523. URL: http://www.osti.gov/servlets/purl/786523/.

[90] *MultiGas™ 2030 FTIR Gas Analyzers*. 2023. URL: https://www.mks.com/f/multigas-2030g-ftir-gas-analyzer.

[91] By Stephen Brunauer et al. *On a Theory of the van der Waals Adsorption of Gases*. Tech. rep. 1. 1940. URL: https://pubs.acs.org/sharingguidelines.

[92] *Manganese | Uses, Facts, & Compounds | Britannica*. 2023. URL: https://www.britannica.com/science/manganese.

[93] Scott H. Fogler. *Elements of Chemical Reaction Engineering*. 5th ed. 2006.

[94] *Nitric Oxide Density*. URL: https://www.engineeringtoolbox.com/gas-density-d_158.html.

[95] Andrzej Borodzinski and Magdalena Bonarowska. "Relation between Crystallite Size and Dispersion on Supported Metal Catalysts". In: *Langmuir* 13 (1997), pp. 5613–5620. URL: https://pubs.acs.org/sharingguidelines.

[96] Yongfa Zhang et al. "Selective methanation of carbon monoxide over Ru-based catalysts in H 2-rich gases". In: (). DOI: 10.1016/j.jiec.2012.02.017.

[97] Elżbieta Truszkiewicz et al. "The Effect of the Ruthenium Crystallite Size on the Activity of Ru/Carbon Systems in CO Methanation". In: 60 (2017), pp. 1299–1305. DOI: 10.1007/s11244-017-0815-z.

[98] T Paryjczak, J Goralski, and K Jozwiak. "CHEMISORPTION OF H 2 , O 2 AND CO ON BIMETALLIC CATALYSTS Rh-Ag/A12 O3". In: *Kinet. Catal. Lett* 16.3 (1981), pp. 111–114.

[99] Ryuya Sakai et al. "Agglomeration Suppression of a Fe-Supported Catalyst and its Utilization for Low-Temperature Ammonia Synthesis in an Electric Field". In: *ACS Omega* 5.12 (Mar. 2020), pp. 6846–6851. ISSN: 24701343. DOI: 10.1021/acsomega.0c00170.

[100] C. C. Hsieh et al. "Structural investigation of catalyst deactivation of Pt/SDB for catalytic oxidation of VOC-containing wastewater". In: *Waste Management* 22.7 (Nov. 2002), pp. 739–745. ISSN: 0956-053X. DOI: 10.1016/S0956-053X(02)00048-X.

[101] P. B. Weisz and C. D. Prater. "Interpretation of Measurements in Experimental Catalysis". In: *Advances in Catalysis* 6.C (Jan. 1954), pp. 143–196. ISSN: 0360-0564. DOI: 10.1016/S0360-0564(08)60390-9.

[102] David E. Mears. "Diagnostic criteria for heat transport limitations in fixed bed reactors". In: *Journal of Catalysis* 20.2 (Feb. 1971), pp. 127–131. ISSN: 0021-9517. DOI: 10.1016/0021-9517(71)90073-X.

[103] Chaitanya K Narula et al. "Remarkable NO oxidation on single supported platinum atoms". In: (2014). DOI: 10.1038/srep07238. URL: www.nature.com/scientificreports.

[104] Sunniva Vold. *Zirconia-Supported Catalysts for Oxidation of NO to NO 2 in the Production of Nitric Acid*. 2021.

APPENDICES

A - CATALYST PREPARATION

A1 - Catalyst Preparation Calculations

The alumina used was 1/8" pellets of γ-Al_2O_3 purchased from Alfa Aesar. CAS number 1314234.

The ruthenium precursor used was $RuCl_3 \cdot xH_2O$, purchased from Sigma Aldrich. CAS number14898-67-0.

The iron precursor used was $Fe(NO_3)_3 \cdot 9\,H_2O$ ($>$ 98% purity), purchased from Sigma Aldrich. CAS number 7782-61-8.

The manganese precursor used was $Mn(NO_3)_2 \cdot 4\,H_2O$, provided by Merck. CAS number: 20694-39-7.

The molar weight of all precursors and the active metals are listed in Table A.1.

Table A.1: Molar mass of all precursor chemicals used for catalyst synthesis.

Chemical	**Molar Mass [g/mo]**
$RuCl_3 \cdot xH_2O$	207.43
Ru	101.07
$Fe(NO_3)_3 \cdot 9\,H_2O$	404.00
Fe	55.845
$Mn(NO_3)_2 \cdot 4\,H_2O$	251.01
Mn	54.93

Table A.2 shows the composition of each catalyst.

The catalysts were prepared by wet impregnation and catalysts with several metals were prepared by co-impregnation. Below is an example of the calculation of the required amounts of precursor and support for 8 g of 5Ru1Fe3Mn. Approximately 1 g H_2O/g catalyst was used to dissolve the precursor.

$$\gamma - Al_2O_3\ (g) = 0.91 * 8\ g = \mathbf{7.28}\ \ \mathbf{g} \tag{1}$$

Table A.2: List of names and compositions of the synthesized catalysts.

Catalyst Name	Composition
1Fe	1% Fe, 99% Al_2O_3
1Mn	1% Mn 99% Al_2O_3
5Ru1Fe	5% Ru, 1% Fe, 94% Al_2O_3
5Ru1Mn	5% Ru, 1% Mn, 94% Al_2O_3
5Ru1Fe1Mn	5% Ru, 1% Fe, 1% Mn, 93% Al_2O_3
5Ru3Fe1Mn	5% Ru, 3% Fe, 1% Mn, 91% Al_2O_3
5Ru1Fe3Mn	5% Ru, 1% Fe, 3% Mn, 91% Al_2O_3

$$Ru\ (g) = 8\ g * 0.05 = 0.4\ g \tag{2}$$

$$Ru\ (mol) = \frac{0.4\ g}{101.07\ g/mol} = 0.00396\ mol \tag{3}$$

$$\mathrm{RuCl_3 \cdot xH_2O}\ (g) = 0.00396\ mol * 207.43\ g/mol = \mathbf{0.8209}\ \ \mathbf{g} \tag{4}$$

$$Fe(g) = 8\ g * 0.01 = 0.08\ g \tag{5}$$

$$Fe\ (mol) = \frac{0.08\ g}{55.845\ g/mol} = 0.00143\ mol \tag{6}$$

$$\mathrm{Fe(NO_3)_3 \cdot 9\,H_2O}\ (g) = 0.00143\ mol * 404.00\ g/mol = \mathbf{0.5787}\ \ \mathbf{g} \tag{7}$$

$$Mn\ (g) = 8\ g * 0.03 = 0.24\ g \tag{8}$$

$$Mn\ (mol) = \frac{0.24\ g}{54.93\ g/mol} = 0.00437\ mol \tag{9}$$

$$\mathrm{Mn(NO_3)_2 \cdot 4\,H_2O}\ (g) = 0.00437\ mol * 251.01\ g/mol = \mathbf{1.097}\ \ \mathbf{g} \tag{10}$$

A2 - Catalyst Preparation Measurements

Table A.3: Measured amounts of support and metal precursor used in the preparation of each catalyst.

Catalyst	**$RuCl_3 \cdot xH_2O$ [g]**	**$Fe(NO_3)_3 \cdot 9\,H_2O$ [g]**	**$Mn(NO_3)_2 \cdot 4\,H_2O$ [g]**	**Al_2O_3 [g]**
1Fe	-	0.5757	-	7.9209
1Mn	-	-	0.3666	7.9222
5Ru1Fe	0.8216	0.5795	-	7.5209
5Ru1Mn	0.8229	-	0.3665	7.522
5Ru1Fe1Mn	0.8219	0.5785	0.3649	7.2815
5Ru3Fe1Mn	0.8205	1.736	0.3656	7.2817
5Ru1Fe3Mn	0.8211	0.5794	1.0974	7.2821

B - CHARACTERIZATION RESULTS

B1 - N_2 adsorption

Figure B.1 shows the isotherm linear plot for the alumina support. Figure B.2 shows the BET surface area plot for the alumina support. Figure B.3 shows the pore size distribution plot for the alumina support.

B2 - CO Chemisorption

Table B.1 shows the mass of catalyst and analysis procedure used for each chemisorption measurement.

Table B.1: Mass of catalyst and analysis procedure used for each chemisorption measurement.

Catalyst	Mass [g]	Analysis Procedure
5Ru1Fe	0.0967	Analysis Procedure 2
5Ru1Mn	0.1196	Analysis Procedure 1
5Ru1Fe1Mn	0.1247	Analysis Procedure 2
5Ru3Fe1Mn	0.139	Analysis Procedure 2
5Ru1Fe3Mn	0.096	Analysis Procedure 2
5Ru1Fe, SP NO	0.1165	Analysis Procedure 2
5Ru1Mn, SP NO	0.1131	Analysis Procedure 1
5Ru1Fe1Mn, SP NO	0.122	Analysis Procedure 2
5Ru3Fe1Mn, SP NO	0.1188	Analysis Procedure 2
5Ru1Fe3Mn, SP NO	0.1083	Analysis Procedure 2

Figure **??** shows the CO chemisorption isotherms recorded for spent 1Mn. It is attached as an example of unacceptable chemisorption isotherms, yielding invalid dispersion measurements.
Figure **??** shows the CO chemisorption isotherms recorded for spent 1Mn. It is attached as an example of acceptable chemisorption isotherms, yielding valid dispersion measurements.

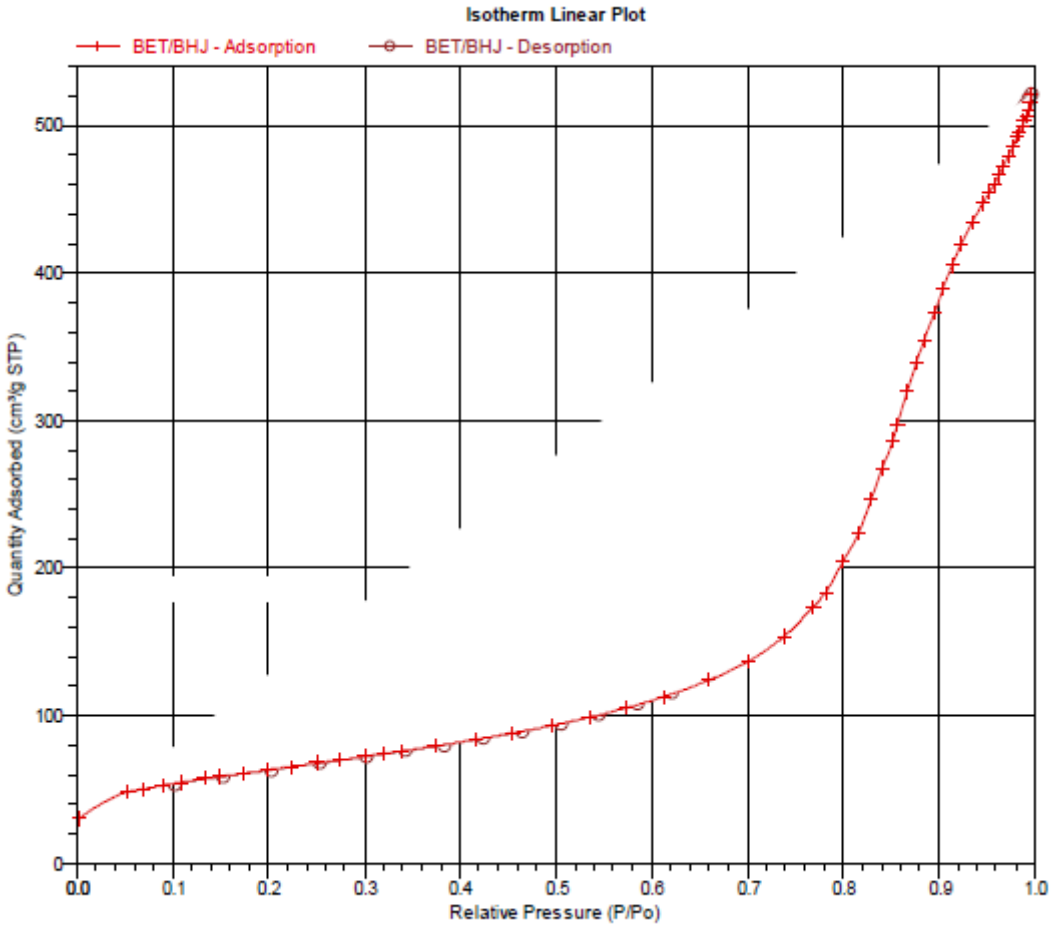

Figure B.1: The isotherm linear plot for Al_2O_3.

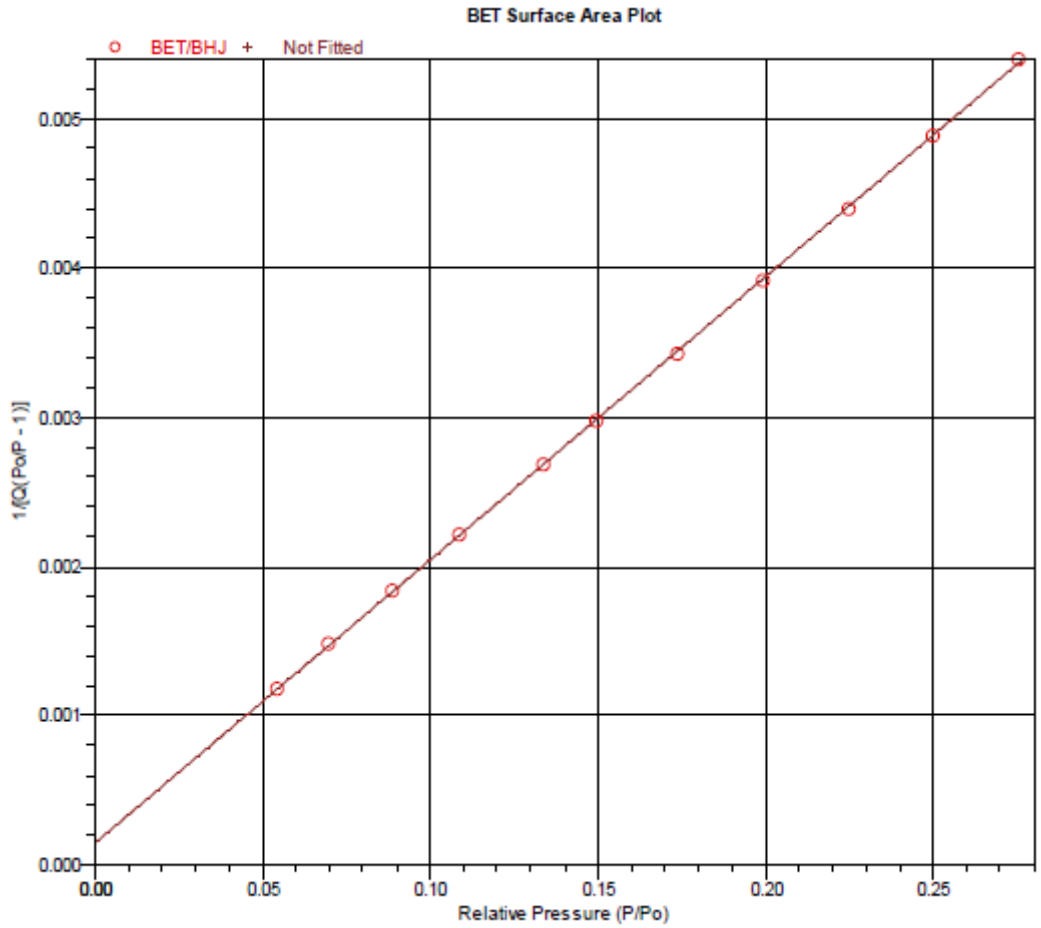

Figure B.2: The BET surface area plot for Al_2O_3.

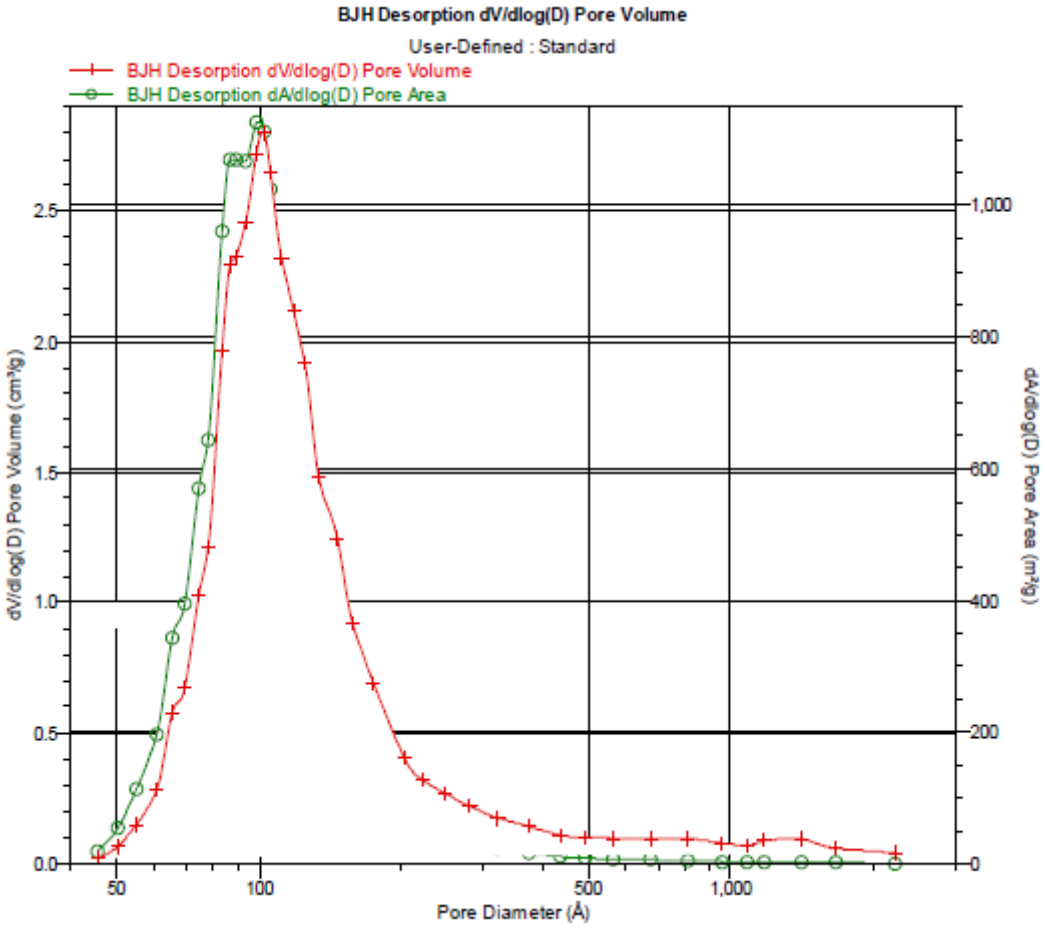

Figure B.3: The BJH desorption pore size distribution plot for Al_2O_3.

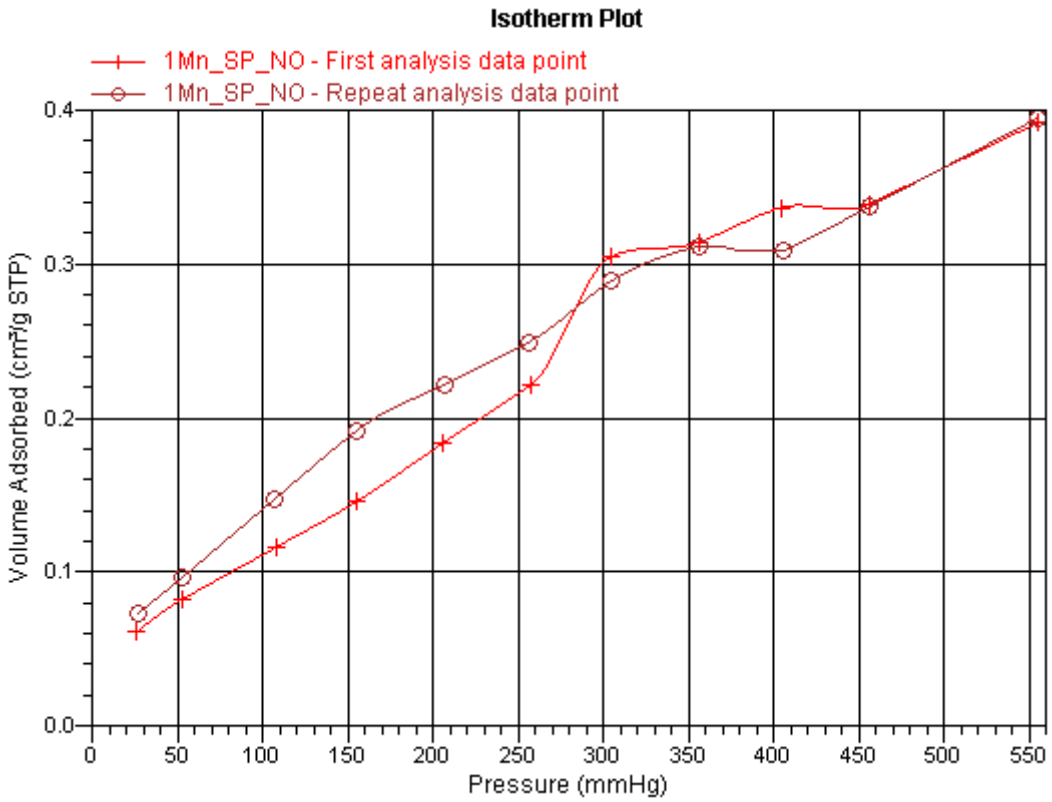

Figure B.4: CO chemisorption isotherms recorded for spent 1Mn at 35 ^{o}C, 25-550 mmHg.

B3 - Remaining X-rady Diffraction Patterns

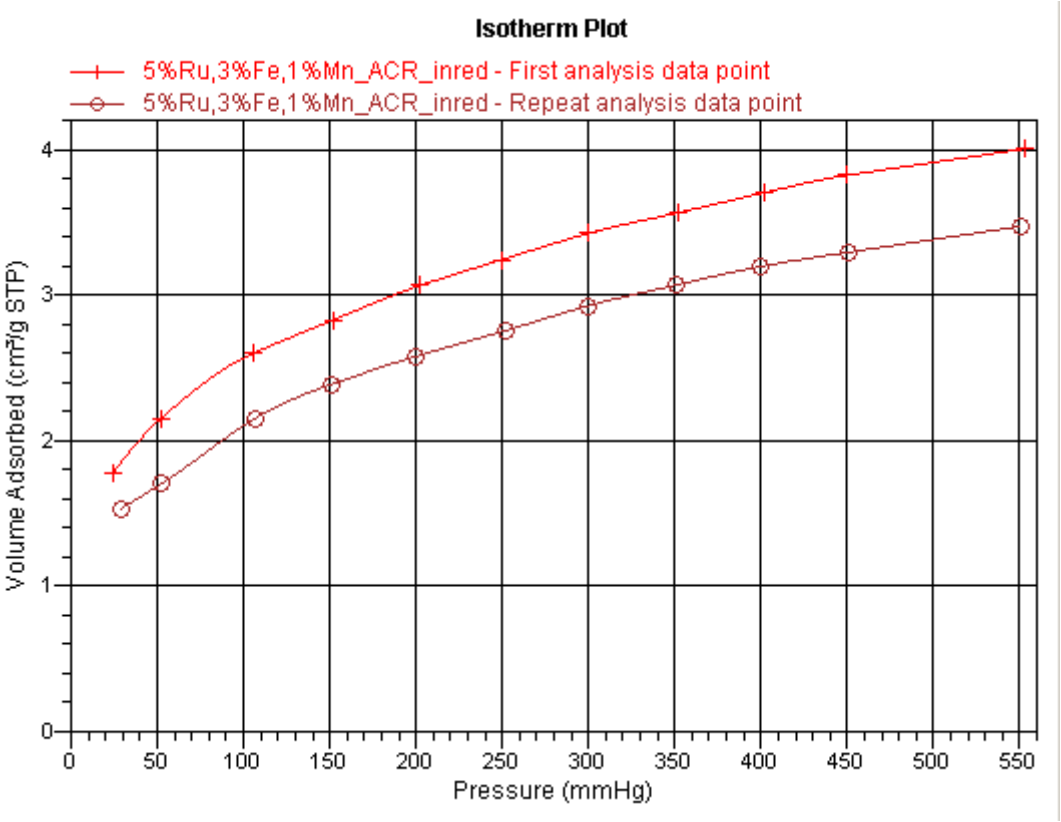

Figure B.5: CO chemisorption isotherms recorded for fresh 5Ru3Fe1Mn at 35 ^{o}C, 25-550 mmHg.

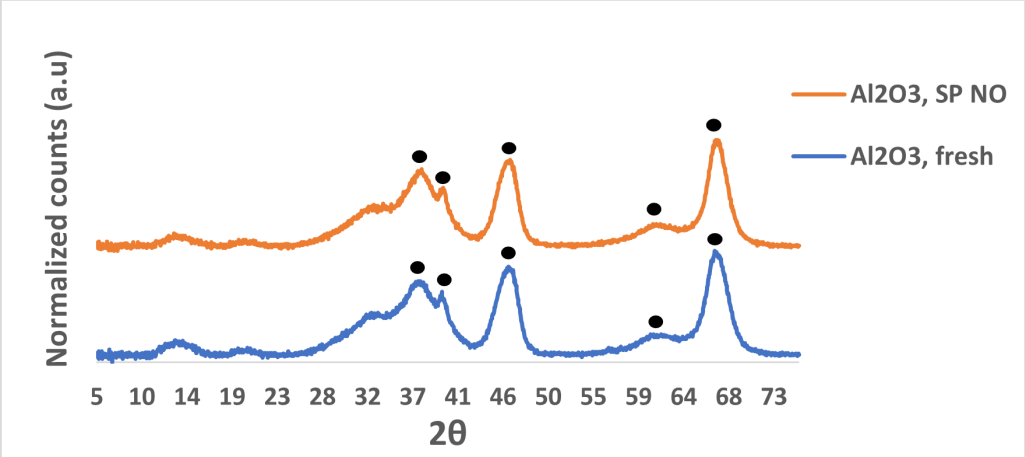

Figure B.6: XRD patterns of fresh and spent Al_2O_3.

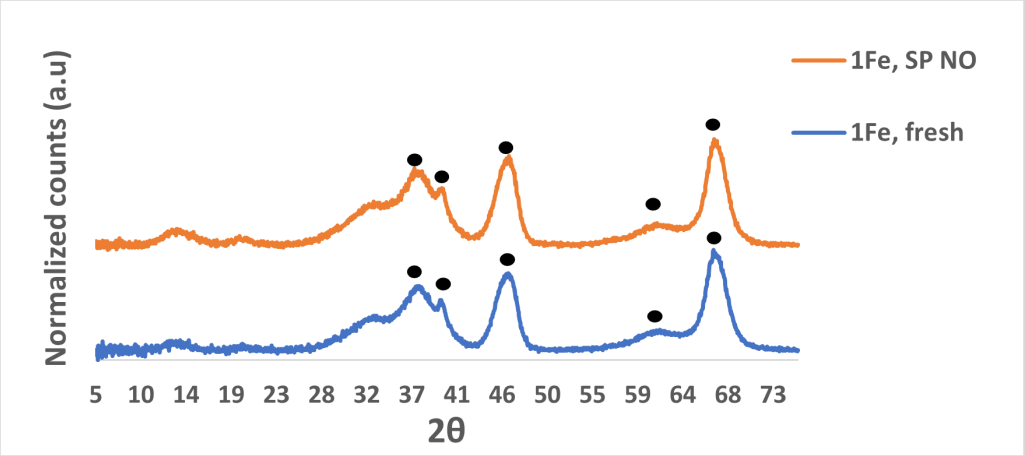

Figure B.7: XRD patterns of fresh and spent 1Fe.

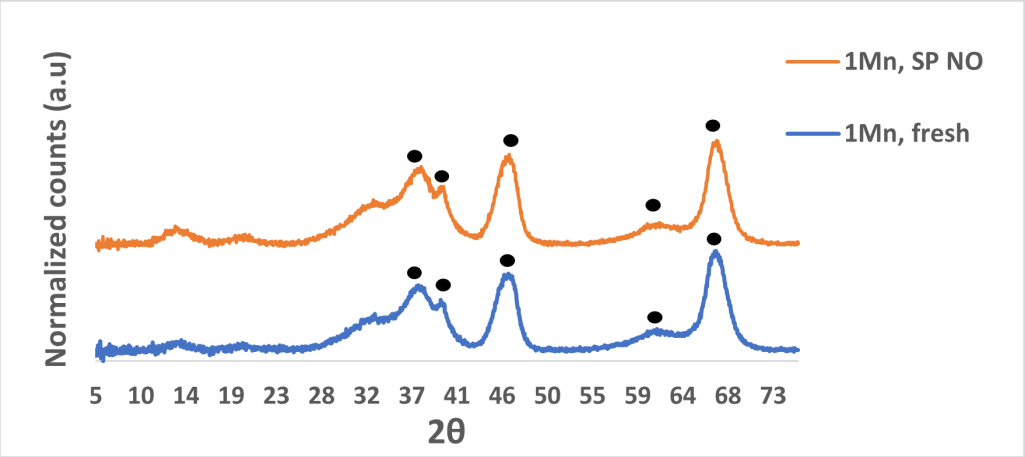

Figure B.8: XRD patterns of fresh and spent 1Mn.

C - CATALYTIC ACTIVITY TESTING

C1 - Experimental Data for Activity Tests

Table C.1 shows the bed height and mass of SiC and catalyst used for every activity test.

Table C.1: Bed height and mass of SiC and catalyst used for every activity test.

Catalyst	Test	SiC mass [g]	Catalyst mass [g]	Bed height [mm]
5Ru1Fe3Mn	450Ramp	2.7615	0.5042	30
5Ru3Fe1Mn	450Ramp	2.7647	0.5050	31
5Ru1Fe1Mn	450Ramp	2.762	0.5107	31
5Ru1Mn	450Ramp	2.755	0.5106	30
5Ru1Fe	450Ramp	2.7656	0.5089	30
1Mn	450Ramp	2.7527	0.5027	30
1Fe	450Ramp	2.7197	0.4936	30
5Ru1Fe3Mn	360SS	2.7624	0.5065	30
SiC + Al2O3	450Ramp	2.6449	0.4687	30
SiC	450Ramp	3.2499		26
ERE	450Ramp			

C2 - Total Conversion

Due to significant levels of noise in the concentration measurements made by the FTIR gas analyzer, all presented catalytic activity data was smoothened using the "Exponential Smoothening" tool in Microsoft Excel. Figures C.1 present the raw data for the activity test for SiC + Al_2O_3, while the smoothened data for the same test is presented in Figure C.2. Figure C.3 and C.4 present the total conversion of NO of SiC and an empty reactor (ERE).

Figure C.5 presents the total conversion of 1Fe and 1Mn. Figures C.6, C.7, C.9, and C.10 show the total conversion of NO for 5Ru3Fe1Mn, 5Ru1Fe3Mn,

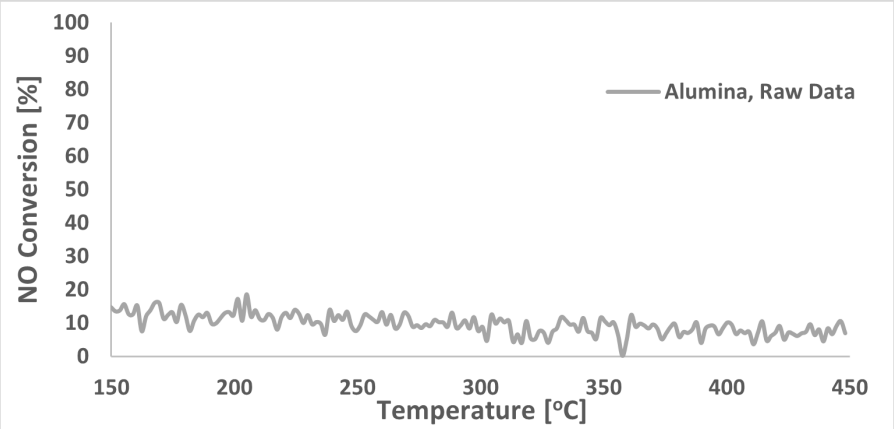

Figure C.1: Raw data of total NO conversion for SiC + Al_2O_3 in 10% NO, 6% O_2, 15% H_2O from 150-450 ^{o}C with a ramp rate of 5 ^{o}C/min, pressure of 1 bar, and WHSV = 24 000 NmL/h $\cdot$ g_{cat}

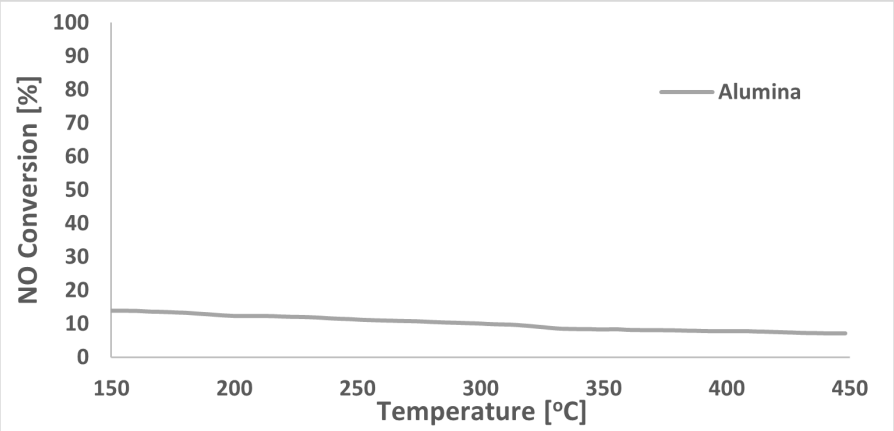

Figure C.2: Smoothened data of total NO conversion for SiC + Al_2O_3 in 10% NO, 6% O_2, 15% H_2O from 150-450 ^{o}C with a ramp rate of 5 ^{o}C/min, pressure of 1 bar, and WHSV = 24 000 NmL/h $\cdot$ g_{cat}

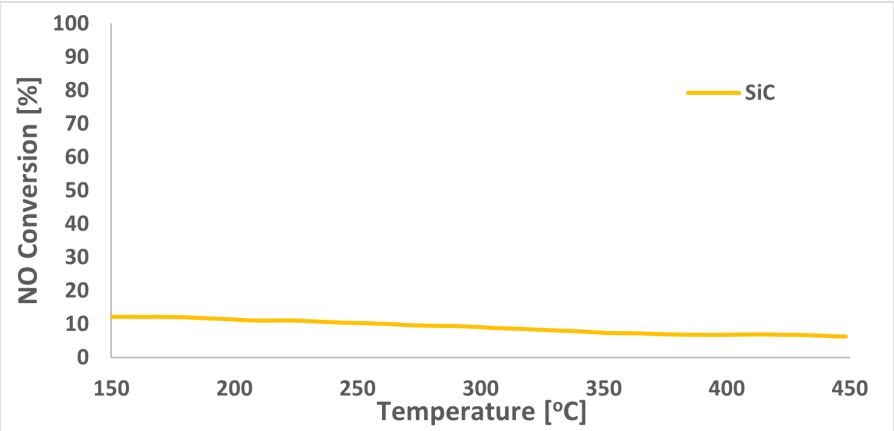

Figure C.3: Raw data of total NO conversion for SiC in 10% NO, 6% O_2, 15% H_2O from 150-450 ^{o}C with a ramp rate of 5 ^{o}C/min, pressure of 1 bar, and WHSV = 24 000 NmL/h $\cdot$ g_{cat}

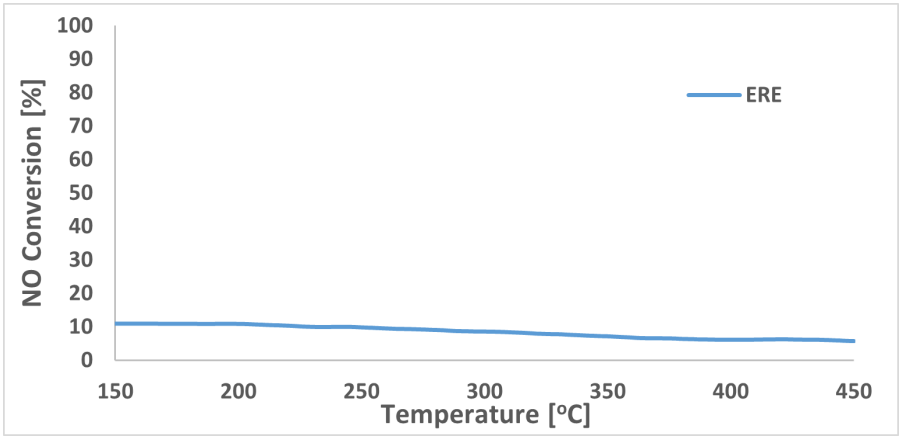

Figure C.4: Total NO conversion for an empty reactor in 10% NO, 6% O_2, 15% H_2O from 150-450 ^{o}C with a ramp rate of 5 ^{o}C/min, pressure of 1 bar, and WHSV = 24 000 NmL/h $\cdot$ g_{cat}

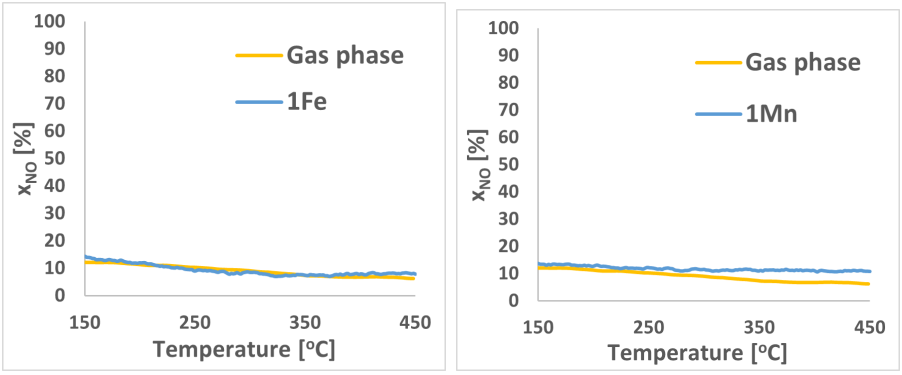

(a) Total conversion of 1Fe. **(b)** Total NO conversion of 1Mn.

Figure C.5: Total NO conversion, x_{NO} (%), of 1Fe and 1Mn in 10% NO, 6% O_2, 15% H_2O from 150-450 ^{o}C with a ramp rate of 5 ^{o}C/min, pressure of 1 bar, and WHSV = 24 000 NmL/h $\cdot$ g_{cat}. The blue line represents the equilibrium curve of NO and NO_2 at 1 bar pressure.

5Ru1Fe1Mn, 5Ru1Fe, and 5Ru1Mn, resepctively. The equilibrium curve of NO and NO_2 at 1 bar pressure is represented as a blue line.

C3 - Catalytic Activity Calculations

The catalytic conversion was calculated by subtracting the gas phase conversion from the total conversion, as shown in Equation 11. This was further used to calculate the catalytic reaction rate using Equation 12.

$$x_{NO,c} = x_{NO} - x_{NO,g} \tag{11}$$

$$r_{NO_2,c} = \frac{x_{NO,c} F_{NO,n}}{m_{cat}} \tag{12}$$

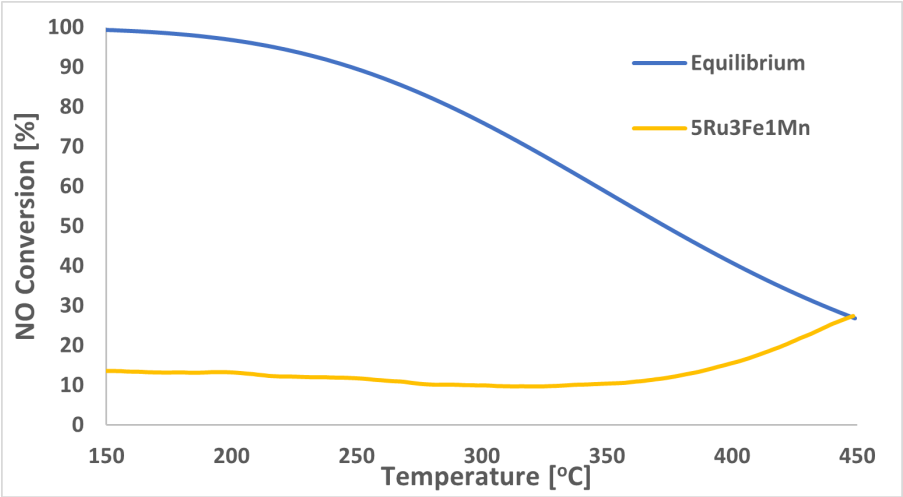

Figure C.6: Raw data of total NO conversion for 5Ru3Fe1Mn in 10% NO, 6% O_2, 15% H_2O from 150-450 °C with a ramp rate of 5 °C/min, pressure of 1 bar, and WHSV = 24 000 NmL/h $\cdot$ g_{cat}. The blue line represents the equilibrium curve of NO and NO_2 at 1 bar pressure.

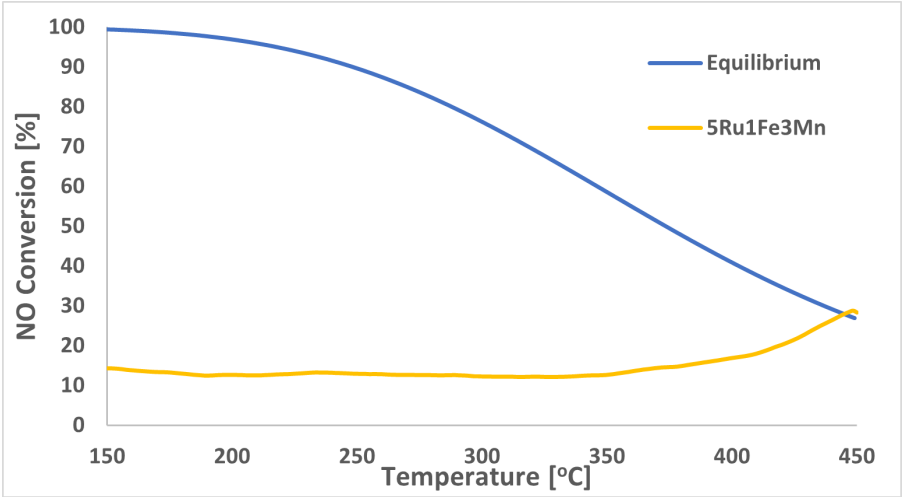

Figure C.7: Raw data of total NO conversion for 5Ru1Fe3Mn in 10% NO, 6% O_2, 15% H_2O from 150-450 °C with a ramp rate of 5 °C/min, pressure of 1 bar, and WHSV = 24 000 NmL/h $\cdot$ g_{cat}. The blue line represents the equilibrium curve of NO and NO_2 at 1 bar pressure.

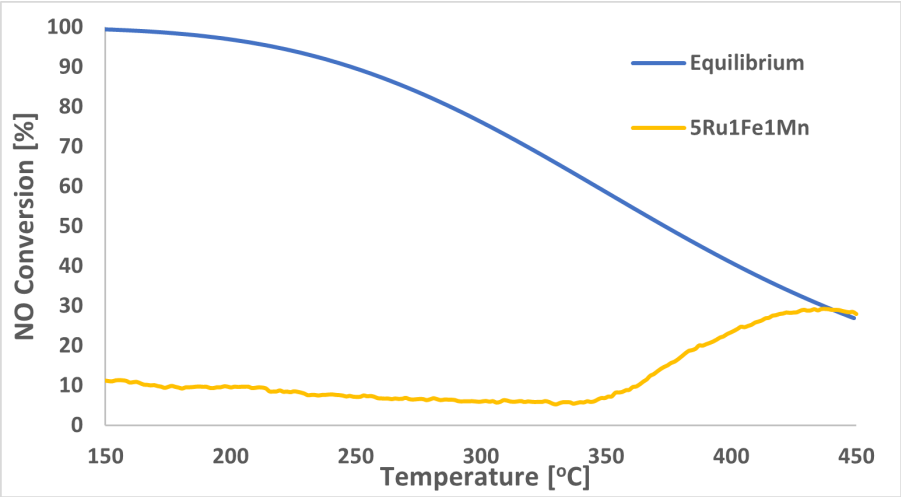

Figure C.8: Raw data of total NO conversion for 5Ru1Fe1Mn in 10% NO, 6% O_2, 15% H_2O from 150-450 °C with a ramp rate of 5 °C/min, pressure of 1 bar, and WHSV = 24 000 NmL/h $\cdot g_{cat}$. The blue line represents the equilibrium curve of NO and NO_2 at 1 bar pressure.

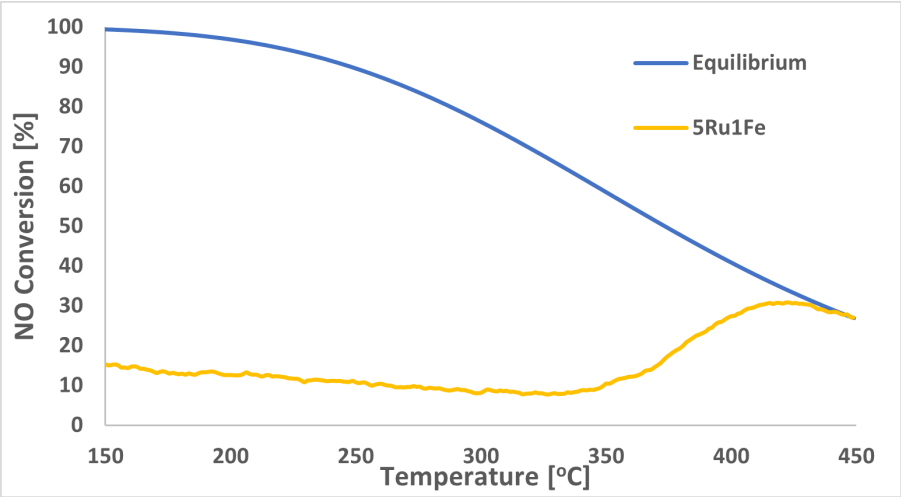

Figure C.9: Raw data of total NO conversion for 5Ru1Fe in 10% NO, 6% O_2, 15% H_2O from 150-450 °C with a ramp rate of 5 °C/min, pressure of 1 bar, and WHSV = 24 000 NmL/h $\cdot g_{cat}$. The blue line represents the equilibrium curve of NO and NO_2 at 1 bar pressure.

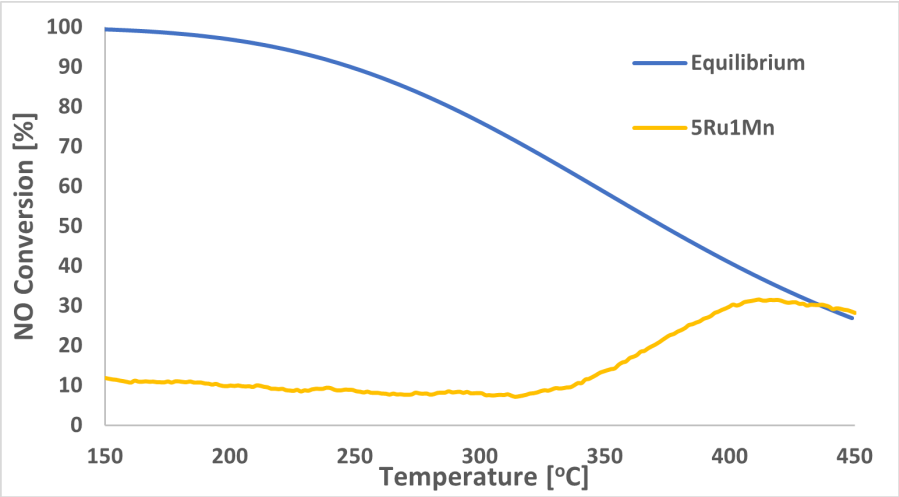

Figure C.10: Raw data of total NO conversion for 5Ru1Mn in 10% NO, 6% O_2, 15% H_2O from 150-450 ^{o}C with a ramp rate of 5 ^{o}C/min, pressure of 1 bar, and WHSV = 24 000 NmL/h$\cdot g_{cat}$. The blue line represents the equilibrium curve of NO and NO_2 at 1 bar pressure.

Where $x_{NO,c}$ is the catalytic conversion of NO to NO_2, $F_{NO,n}$ is the molar flow rate of NO at the inlet, and m_{cat} is the mass of the catalyst. To find the molar flow rate of NO, 1.249 g/L is used as the density of NO (20 ^{o}C, 1 bar) [94]. Below is an example of a calculation of the catalytic reaction rate for 5Ru1Mn at 425 ^{o}C.

$$x_{NO,c} = 30.822\% - 5.839\% = 24.983\% \tag{13}$$

$$r_{NO_2} = \frac{0.24983 * 0.2128\ mol/min}{60 * 0.5106\ g_{cat}} = 0.0001735\ mol/(s.g_{cat}) \tag{14}$$

C.3.1 - Dependence on Temperature

The temperature dependency of the catalytic conversion for each catalyst was evaluated as the slope of the catalytic conversion across two ranges of temperature, 350-400 ^{o}C and 375-425 ^{o}C. The slope was calculated by linear regression, described by Equation 15.

$$y = mx + b \tag{15}$$

Where m is the slope, presented in Table **??** together with the R^2 value for the regression fit.

Catalyst	**Temperature Range [^{o}C]**	**Slope**	R^2
5Ru1Fe	350-400	0.3891	0.9838
	375-425	0.32	0.9655
5Ru1Mn	350-400	0.3542	0.9982
	375-425	0.2472	0.9524
5Ru1Fe1Mn	350-400	0.36	0.9915
	375-425	0.29	0.9875
5Ru3Fe1Mn	350-400	0.12	0.9716
	375-425	0.20	0.989
5Ru1Fe3Mn	350-400	0.03	0.9544
	375-425	0.15	0.9684

D.1 - Flow Scheme of Rig 2.1

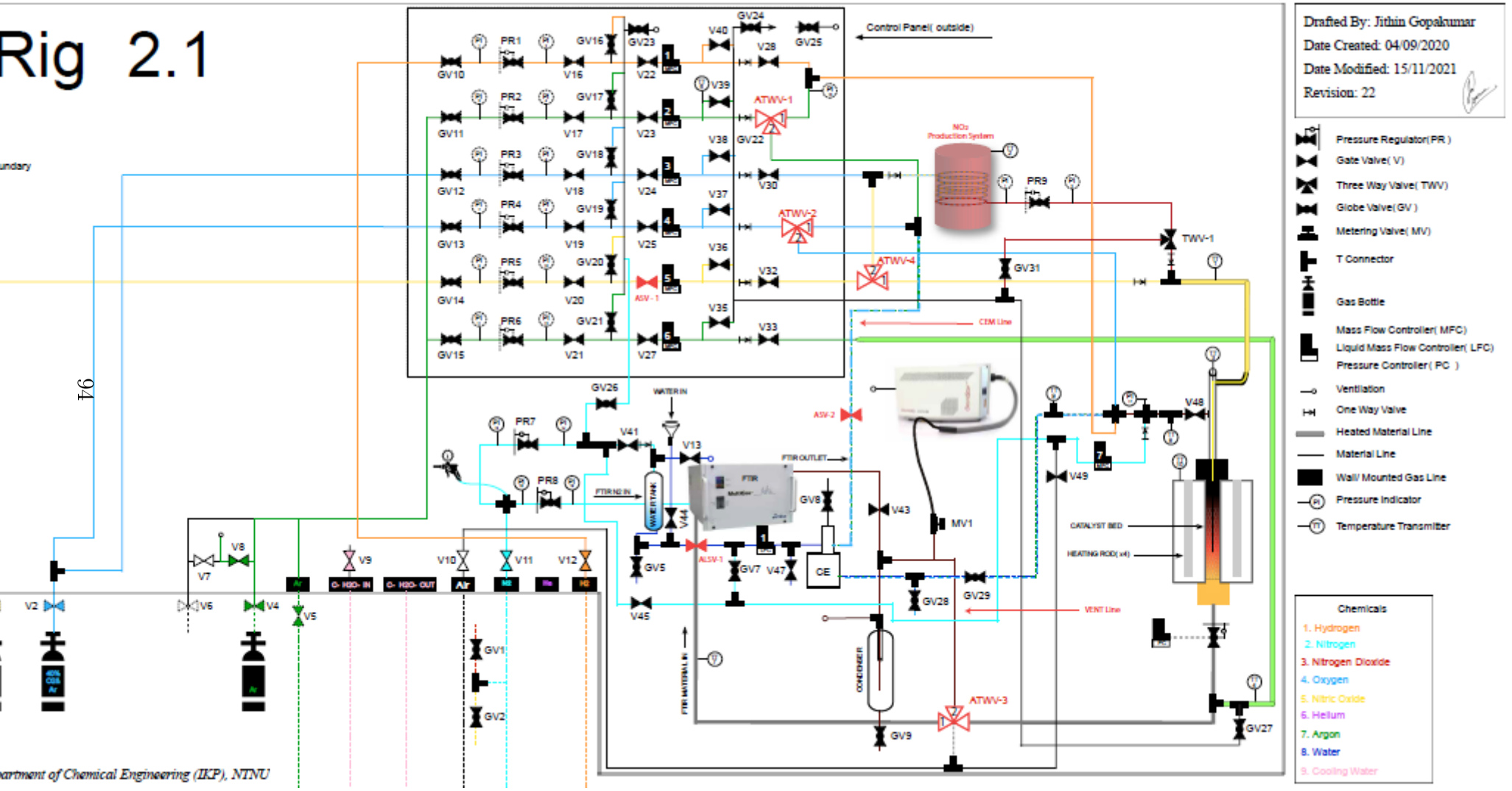
Rig 2.1
Drafted By: Jithin Gopakumar
Date Created: 04/09/2020
Date Modified: 15/11/2021
Revision: 22
Control Panel(outside)
Pressure Regulator(PR)
Gate Valve(V)
Three Way Valve(TWV)
Globe Valve(GV)
Metering Valve(MV)
T Connector
Gas Bottle
Mass Flow Controller(MFC)
Liquid Mass Flow Controller(LFC)
Pressure Controller(PC)
Ventilation
One Way Valve
Heated Material Line
Material Line
Wall/ Mounted Gas Line
Pressure Indicator
Temperature Transmitter
Chemicals
1. Hydrogen
2. Nitrogen
3. Nitrogen Dioxide
4. Oxygen
5. Nitric Oxide
6. Helium
7. Argon
8. Water
9. Cooling Water
ATWV-1
ATWV-2
ATWV-3
ATWV-4
TWV-1
MV1
ASV-1
ASV-2
ASV - 1
NO2 Production System
CEM Line
VENT Line
CATALYST BED
HEATING ROD(x4)
FTIR OUTLET
FTIR N2 IN
FTIR MATERIAL IN
WATER IN
WATER TANK
FTIR
CE
OZONIZER
PR1
PR2
PR3
PR4
PR5
PR6
PR7
PR8
PR9
GV1
GV2
GV5
GV7
GV8
GV9
GV10
GV11
GV12
GV13
GV14
GV15
GV16
GV17
GV18
GV19
GV20
GV21
GV22
GV23
GV24
GV25
GV26
GV27
GV28
GV29
GV31
V2
V4
V5
V6
V7
V8
V9
V10
V11
V12
V13
V21
V22
V23
V24
V25
V27
V28
V30
V32
V33
V35
V36
V37
V38
V39
V40
V41
V43
V44
V45
V47
V48
V49
C- H2O- IN
C- H2O- OUT
Air
94
Department of Chemical Engineering (IKP), NTNU

Figure D.2: Contaminated gold plated mirror in the FTIR gas analyzer.

D.2 - Contaminated Gold Plated Mirror in FTIR Gas Analyzer

Figure D.3: Contaminated gold plated mirror in the FTIR gas analyzer.

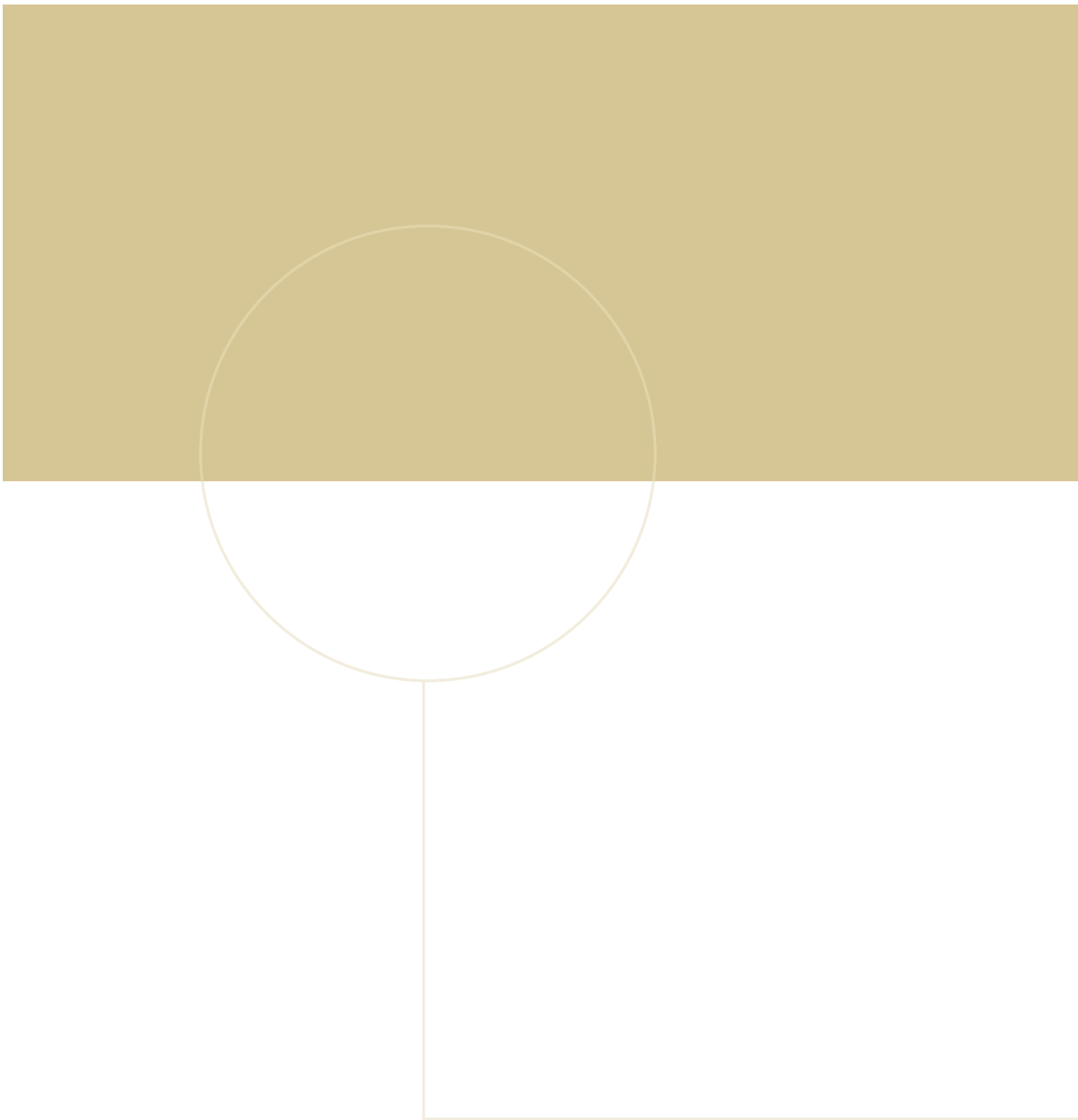

NTNU

Kunnskap for en bedre verden